Accepted Manuscript

An upwind cell centred Total Lagrangian finite volume algorithm for nearly incompressible explicit fast solid dynamic applications

Jibran Haider, Chun Hean Lee, Antonio J. Gil, Antonio Huerta, Javier Bonet

Please cite this article as: J. Haider, C.H. Lee, A.J. Gil, A. Huerta, J. Bonet, An upwind cell centred Total Lagrangian finite volume algorithm for nearly incompressible explicit fast solid dynamic applications, *Comput. Methods Appl. Mech. Engrg.* (2018), https://doi.org/10.1016/j.cma.2018.06.010

An upwind cell centred Total Lagrangian finite volume algorithm for nearly incompressible explicit fast solid dynamic applications

Jibran Haider [a], Chun Hean Lee [a,1], Antonio J. Gil [a,2], Antonio Huerta [b], Javier Bonet [c]

[a] *Zienkiewicz Centre for Computational Engineering, College of Engineering,
Swansea University, Bay Campus, SA1 8EN, United Kingdom*

[b] *Laboratori de Càlcul Numèric, Universitat Politècnica de Catalunya,
Campus Nord, Barcelona, 08034, Spain*

[c] *University of Greenwich, London, SE10 9LS, United Kingdom*

Abstract

The paper presents a new computational framework for the numerical simulation of fast large strain solid dynamics, with particular emphasis on the treatment of near incompressibility. A complete set of first order hyperbolic conservation equations expressed in terms of the linear momentum and the minors of the deformation (namely the deformation gradient, its co-factor and its Jacobian), in conjunction with a polyconvex nearly incompressible constitutive law, is presented. Taking advantage of this elegant formalism, alternative implementations in terms of entropy-conjugate variables are also possible, through suitable symmetrisation of the original system of conservation variables. From the spatial discretisation standpoint, modern Computational Fluid Dynamics code "OpenFOAM" [http://www.openfoam.com/] is here adapted to the field of solid mechanics, with the aim to bridge the gap between computational fluid and solid dynamics. A cell centred finite volume algorithm is employed and suitably adapted. Naturally, discontinuity of the conservation variables across control volume interfaces leads to a Riemann problem, whose resolution requires special attention when attempting to model materials with predominant nearly incompressible behaviour ($\kappa/\mu \geq 500$). For this reason, an acoustic Riemann solver combined with a preconditioning procedure is introduced. In addition, a global a posteriori angular momentum projection procedure proposed in [1] is also presented and adapted to a Total Lagrangian version of the nodal scheme of Kluth and Després [2] used in this paper for comparison purposes. Finally, a series of challenging numerical examples is examined in order to assess the robustness and applicability of the proposed methodology with an eye on large scale simulation in future works.

Keywords: First order conservation laws, Large strain solid dynamics, Finite Volume Method, Riemann solver, OpenFOAM

1. Introduction

Current commercial (displacement-based) Finite Element Method (FEM) codes are extensively used for the simulation of large strain fast solid dynamic problems in the aerospace, automotive, defence and manufacturing industries. However, these commercial codes present a number of shortcomings [3, 4], namely (1) reduced order of convergence for strains and stresses in comparison with that of displacements [5, 6], (2) high frequency noise in the vicinity of shocks [7–10], and (3) hour-glassing and pressure checkerboarding modes [11–17].

---

[1] Corresponding author: c.h.lee@swansea.ac.uk

[2] Corresponding author: a.j.gil@swansea.ac.uk

In order to overcome some of these drawbacks, a number of methodologies have been proposed over the years. One very popular option used in industry is to resort to a selective reduced integration procedure [3, 18–21] along with (tri-linear) hexahedral elements. In this case, a reduced number of Gauss integration points is utilised in order to under-integrate the volumetric component of the stress. However, as it is well known, the resulting formulation is still incapable of addressing the existence of shear locking in bending dominated scenarios [20, 21].

Alternatively, Bonet and Burton [22] introduced a FEM based nodally integrated procedure where the pressure field is under-integrated at nodes when employing the linear tetrahedral element (usually preferred in the case of complex geometries). Although this methodology was found to perform extremely well in nearly incompressible impact problems, it behaved poorly in bending dominated scenarios resulting in the appearance of hourglassing-like modes [23–25]. Several variants of the nodal pressure approach have since followed, including the averaged nodal deformation gradient [26], the F-bar method [27] and the Smoothed Finite Element Method [13]. However, all of these methods still suffer from spurious hydrostatic pressure fluctuations when attempting to model nearly incompressible materials [14].

On another front, several attempts have also been reported aiming to solve solid mechanics problems via the use of (displacement-based) finite volume based discretisations [28–33]. Some interesting work has also been recently explored using the open source platform "OpenFOAM", with special attention paid to the simulation of contact mechanics [34], orthotropic materials experiencing moderate strains [35] and metal forming applications [36].

The earliest attempt at employing a (mixed) hyperbolic system of first order conservation laws in solid dynamics originates from the work of Trangenstein and Colella [37, 38], where the conservation variables were the linear momentum p and the deformation gradient tensor F. A second order Godunov-type finite volume framework in conjunction with the use of a Riemann-based upwinding stabilisation was presented. However, the examples presented in the paper were restricted to the case of small strain linear elasticity in two dimensions [38]. With a similar philosophy, a node based Finite Volume Method (FVM), originally proposed by Mazeran and Després [39] in gas dynamics applications [40–44], was adapted to the context of hyperelastic solids in [2, 45]. Scovazzi and co-authors [46–49] also used a mixed based methodology for a linear tetrahedral element by utilising a Variational Multi-Scale method.

In recent years, some of the authors of this manuscript have pursued the same $\{p, F\}$ mixed-based approach whilst exploring a wide range of spatial discretisation techniques, including: upwind cell centred FVM [1, 50], Jameson–Schmidt–Turkel vertex centred FVM [51], upwind vertex centred FVM [52], two step Taylor–Galerkin FEM [53], stabilised Petrov–Galerkin FEM [54–57], Jameson–Schmidt–Turkel SPH [58] and Streamline Upwind Petrov–Galerkin SPH [59]. Very recently [1], a mixed-based $\{p, F\}$ cell centred finite volume algorithm, entitled TOUCH, was successfully developed for three dimensional applications, with a tailor-made implementation into the open source platform "OpenFOAM". Crucially, in order to fulfil the satisfaction of the inherent involutions within the system (also known as compatibility conditions [60, 61]), two variants of the TOUCH scheme were proposed, namely (a) Constrained-TOUCH (C-TOUCH) and (b) Penalised-TOUCH (P-TOUCH). In addition, an alternative Total Lagrangian version of the node based scheme presented in [2], namely X-GLACE, was also explored and implemented within the OpenFOAM environment. However, the methodologies introduced in [1] have been found to be inefficient when approaching the extreme limit of incompressibility ($\kappa/\mu \geq 500$).

With this in mind, the main aim of this paper is the improvement of the robustness and effectiveness of both TOUCH and X-GLACE schemes, extending their applicability to quasi incompressibility scenarios. To achieve this, we propose to incorporate two additional geometric conservation laws, one for the co-factor of the deformation (or area map) H and the other for the Jacobian of the deformation (or volume map) J. From a spatial discretisation point of view, a cell centred finite volume algorithm in conjunction with a monotonic slope reconstruction is employed. Discontinuity of the conservation variables across control volume interfaces leads to a Riemann problem [1, 50, 52, 62], whose resolution however requires special attention when attempting to model materials with nearly incompressible behaviour ($\kappa/\mu \geq 500$). In this paper, an acoustic Riemann solver combined with a preconditioning procedure is introduced, with the aim
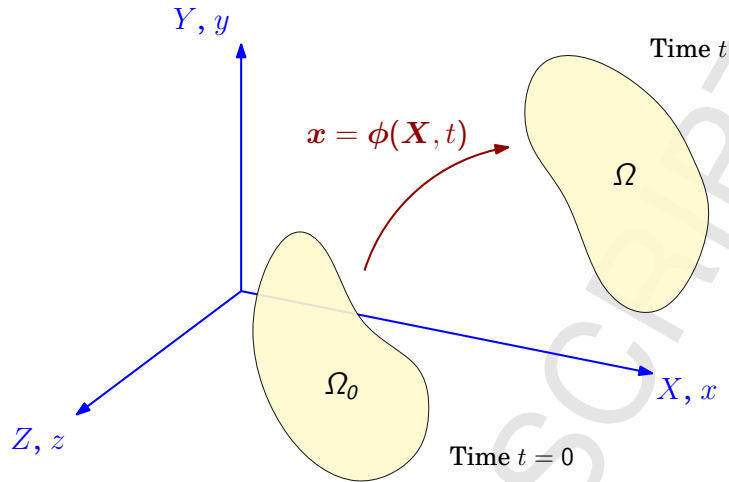
2

Figure 1: Motion of a continuum body

to recover a correct scaling of the numerical upwinding stabilisation. This preconditioning procedure has been previously used for the numerical simulation of the compressible Euler equations in the low Mach number limit [63–66]. For a fair comparison across the various schemes (TOUCH and X-GLACE), a global a posteriori angular momentum preserving procedure presented in Ref. [1] is now suitably adapted to the case of the node based X-GLACE scheme. An alternative approach was introduced by Després and Labourasse [67], which incorporates an angular momentum preserving reconstruction procedure within every cell via the use of a Lagrange multiplier.

The paper is organised as follows. Section 2 summarises the extended $\{\boldsymbol{p}, \boldsymbol{F}, \boldsymbol{H}, J\}$ system of first order hyperbolic conservation laws for solid dynamics. Section 3 details some fundamental aspects of the finite volume spatial discretisation procedure used in this work. An acoustic Riemann solver in conjunction with a preconditioning procedure is shown in Section 4. Section 5 describes the one-step two-stage TVD Runge–Kutta time integrator used for temporal discretisation. Section 7 presents the algorithmic description of the complete $\{\boldsymbol{p}, \boldsymbol{F}, \boldsymbol{H}, J\}$ TOUCH and $\{\boldsymbol{p}, \boldsymbol{F}, \boldsymbol{H}, J\}$ X-GLACE schemes. For benchmarking purposes, an extensive set of challenging numerical examples is examined in Section 8. Finally, Section 9 presents some concluding remarks and future directions of research.

2. Reversible elastodynamics

Consider the three dimensional deformation of an elastic body of material density ρ_0 moving from its initial undeformed configuration occupying a volume Ω_0, of boundary $\partial \Omega_0$, to a current deformed configuration at time t occupying a volume Ω, of boundary $\partial \Omega$ (see Fig. 1). The motion is defined through a deformation mapping $\boldsymbol{x} = \boldsymbol{\phi}(\boldsymbol{X}, t)$ which satisfies the following mixed based set of Total Lagrangian conservation laws [50–52, 54–59]

3

$$\frac{\partial \boldsymbol{p}}{\partial t} = \mathrm{DIV}\boldsymbol{P} + \rho_0\boldsymbol{b};\tag{1a}$$

$$\frac{\partial \boldsymbol{F}}{\partial t} = \mathrm{DIV}\left(\frac{\boldsymbol{p}}{\rho_0} \otimes \boldsymbol{I}\right);\tag{1b}$$

$$\frac{\partial \boldsymbol{H}}{\partial t} = \mathrm{CURL}\left(\frac{\boldsymbol{p}}{\rho_0} \times \boldsymbol{F}\right);\tag{1c}$$

$$\frac{\partial J}{\partial t} = \mathrm{DIV}\left(\boldsymbol{H}^T\frac{\boldsymbol{p}}{\rho_0}\right);\tag{1d}$$

$$\frac{\partial E}{\partial t} = \mathrm{DIV}\left(\boldsymbol{P}^T\frac{\boldsymbol{p}}{\rho_0}\right).\tag{1e}$$

Here, $\boldsymbol{p}$ is the linear momentum, $\boldsymbol{F}$ is the deformation gradient (or fibre map), $\boldsymbol{H}$ is the co-factor of the deformation (or area map), J is the Jacobian of the deformation (or volume map), E is the total energy, $\boldsymbol{P}$ is the first Piola-Kirchhoff stress tensor, $\boldsymbol{I}$ is the identity tensor and $\boldsymbol{b}$ is the material body force per unit of mass. The operators DIV and CURL denote the material divergence and material curl, respectively, and $\times$ denotes a tensor cross product between vectors and/or second order tensors as that presented in Ref. [68].

In this paper, we restrict ourselves only to the use of isothermal elasticity. Expression (1e) is thus redundant and is fully decoupled from the rest of the system equations (1a-1d). However, from a numerical viewpoint, the above energy equation (1e) is still extremely useful when monitoring the numerical dissipation (entropy) of the algorithm. Finally, the current geometry $\boldsymbol{x}$ can be obtained through time integration of the velocity field as

$$\frac{\partial \boldsymbol{x}}{\partial t} = \frac{\boldsymbol{p}}{\rho_0}.\tag{2}$$

It is now possible to combine all the balance equations described in (1a-1e) into a hyperbolic system of first order conservation laws written under a Total Lagrangian formalism

$$\frac{\partial \boldsymbol{\mathcal{U}}}{\partial t} + \frac{\partial \boldsymbol{\mathcal{F}}_I}{\partial X_I} = \boldsymbol{\mathcal{S}};\qquad \forall\, I = 1, 2, 3,\tag{3}$$

where the Einstein's summation convention is used such that the repeated indices I are to be summed from 1 to 3. Here, $\boldsymbol{\mathcal{U}}$ denotes the vector of conservation variables, $\boldsymbol{\mathcal{F}}_I$ is the flux vector in the I-th material direction and $\boldsymbol{\mathcal{S}}$ is a possible source term, described as follows

$$\boldsymbol{\mathcal{U}} = \begin{bmatrix} \boldsymbol{p} \\ \boldsymbol{F} \\ \boldsymbol{H} \\ J \\ E \end{bmatrix};\qquad \boldsymbol{\mathcal{F}}_I = -\begin{bmatrix} \boldsymbol{P}\boldsymbol{E}_I \\ \frac{1}{\rho_0}\boldsymbol{p} \otimes \boldsymbol{E}_I \\ \boldsymbol{F} \times \left(\frac{1}{\rho_0}\boldsymbol{p} \otimes \boldsymbol{E}_I\right) \\ \boldsymbol{H} : \left(\frac{1}{\rho_0}\boldsymbol{p} \otimes \boldsymbol{E}_I\right) \\ \boldsymbol{P} : \left(\frac{1}{\rho_0}\boldsymbol{p} \otimes \boldsymbol{E}_I\right) \end{bmatrix},\qquad \boldsymbol{\mathcal{S}} = \begin{bmatrix} \rho_0\boldsymbol{b} \\ \boldsymbol{0} \\ \boldsymbol{0} \\ 0 \\ 0 \end{bmatrix}.\tag{4}$$

The corresponding flux vector associated with the material unit outward normal $\boldsymbol{N}$ can now be expressed as

$$\boldsymbol{\mathcal{F}}_{\boldsymbol{N}} = \boldsymbol{\mathcal{F}}_I N_I = -\begin{bmatrix} \boldsymbol{P}\boldsymbol{N} \\ \frac{1}{\rho_0}\boldsymbol{p} \otimes \boldsymbol{N} \\ \boldsymbol{F} \times \left(\frac{1}{\rho_0}\boldsymbol{p} \otimes \boldsymbol{N}\right) \\ \boldsymbol{H} : \left(\frac{1}{\rho_0}\boldsymbol{p} \otimes \boldsymbol{N}\right) \\ \left(\frac{1}{\rho_0}\boldsymbol{P}^T\boldsymbol{p}\right) \cdot \boldsymbol{N} \end{bmatrix}.\tag{5}$$

4

Additionally, in the presence of non-smooth solutions, all of the above conservation laws described in (1a-1e) are accompanied by appropriate Rankine Hugoniot jump conditions across a discontinuous surface propagating with speed of c [1, 50–52, 57], defined as

$$c \, [\![\boldsymbol{p}]\!] = -[\![\boldsymbol{P}]\!] \boldsymbol{N}; \tag{6a}$$

$$c \, [\![\boldsymbol{F}]\!] = -\frac{1}{\rho_0} [\![\boldsymbol{p}]\!] \otimes \boldsymbol{N}; \tag{6b}$$

$$c \, [\![\boldsymbol{H}]\!] = -\boldsymbol{F}^{\mathrm{Ave}} \times \left(\frac{1}{\rho_0} [\![\boldsymbol{p}]\!] \otimes \boldsymbol{N} \right); \tag{6c}$$

$$c \, [\![J]\!] = -\boldsymbol{H}^{\mathrm{Ave}} : \left(\frac{1}{\rho_0} [\![\boldsymbol{p}]\!] \otimes \boldsymbol{N} \right); \tag{6d}$$

$$c \, [\![E]\!] = -\left(\frac{1}{\rho_0} [\![\boldsymbol{P}^T \boldsymbol{p}]\!] \right) \cdot \boldsymbol{N}. \tag{6e}$$

Here, $[\![\cdot]\!] := [\cdot]^+ - [\cdot]^-$ denotes the jump operator across a discontinuity surface with normal $\boldsymbol{N}$ moving with speed c in the reference space and $[\cdot]^{\mathrm{Ave}} := \frac{1}{2}\left([\cdot]^+ + [\cdot]^-\right)$ being defined as an average state between the left and right states of a discontinuity surface.

It is clear from equations (1b-1c) that two sets of involutions [60] must be satisfied by the geometric strain variables $\{\boldsymbol{F}, \boldsymbol{H}\}$ of the system as

$$\mathrm{CURL}\boldsymbol{F} = \boldsymbol{0}; \qquad \mathrm{DIV}\boldsymbol{H} = \boldsymbol{0}. \tag{7}$$

As a consequence, equations (1c) and (1d) can be further reduced to the non-conservative form of the differential equations presented as follows

$$\frac{\partial \boldsymbol{H}}{\partial t} = \boldsymbol{F} \times \mathrm{GRAD}\left(\frac{\boldsymbol{p}}{\rho_0}\right); \qquad \frac{\partial J}{\partial t} = \boldsymbol{H} : \mathrm{GRAD}\left(\frac{\boldsymbol{p}}{\rho_0}\right), \tag{8}$$

where GRAD is the material gradient operator defined as $\mathrm{GRAD} := \frac{\partial}{\partial \boldsymbol{X}}$ [19].

For the particular case of a reversible process, the closure of the system described in (1a-1e) requires the introduction of a suitable constitutive law relating the stress tensor $\boldsymbol{P}$ with the geometric strain measures $\{\boldsymbol{F}, \boldsymbol{H}, J\}$, obeying the principle of objectivity [19] and thermodynamic consistency (via the Colemann-Noll procedure) [69]. In this work, a polyconvex nearly incompressible constitutive model is employed and will be summarised in Section 2.1. It is interesting to remark how the complete set of first order conservation laws in (1a-1e) in conjunction with the polyconvex nature of the constitutive model (i.e. a guarantor of material stability [70]), can be used for the transformation of the system of conservation laws into a symmetric set of hyperbolic equations expressed in terms of the entropy conjugates of the conservation variables [56, 57]. Finally, for the complete definition of the initial boundary value problem, initial and boundary (essential and natural) conditions must also be specified as appropriate.

2.1. Constitutive model: Polyconvex elasticity

Polyconvexity [70] is a well accepted mathematical requirement that is satisfied by admissible multi-variable strain energy functions used to describe large strain deformation of elastic materials. For a polyconvex (nearly incompressible) Mooney-Rivlin material, the multi-variable strain energy W can be decomposed into the summation of deviatoric $\hat{W}(\boldsymbol{F}, \boldsymbol{H}, J)$ and volumetric $U(J)$ contributions [56, 57, 70]

$$W = \hat{W} + U, \tag{9}$$

with

$$\hat{W} = \zeta J^{-2/3} \left(\boldsymbol{F} : \boldsymbol{F}\right) + \xi J^{-2} \left(\boldsymbol{H} : \boldsymbol{H}\right)^{3/2} - 3\left(\zeta + \sqrt{3}\xi\right); \qquad U = \frac{\kappa}{2}(J-1)^2, \tag{10}$$
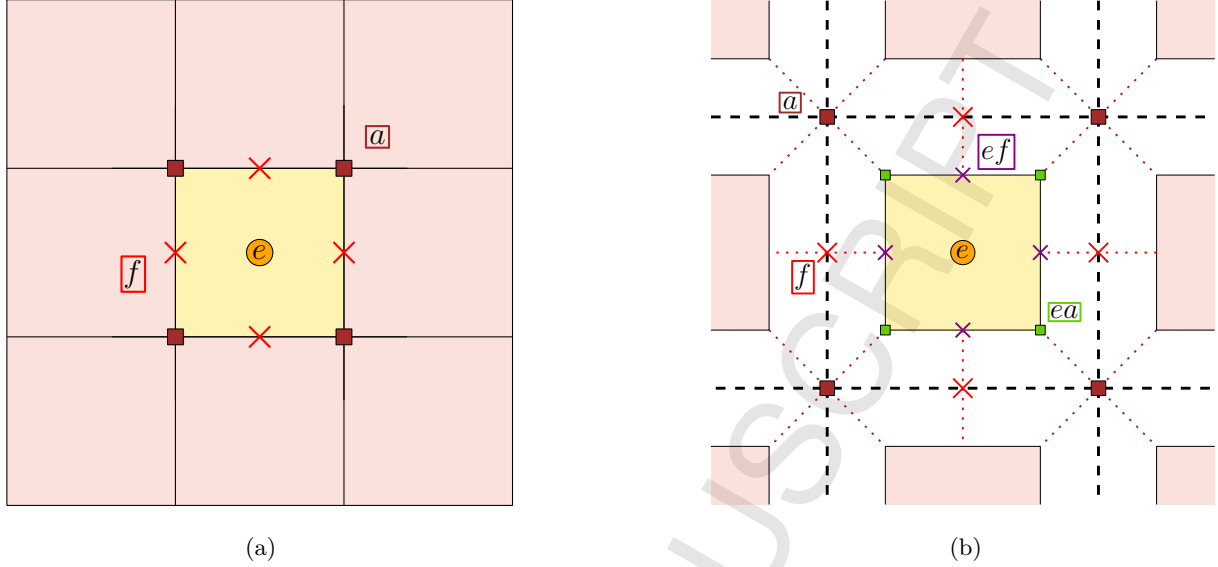
5

Figure 2: Nomenclature used for the finite volume spatial discretisation of (a) a quadrilateral mesh, and (b) an exploded view of (a).

where ζ, ξ and κ (bulk modulus) are positive material parameters. By comparison of the tangent elasticity operator at the initial undeformed configuration with that of classical linear elasticity [70], appropriate values for the material parameters ζ and ξ can be defined in terms of the shear modulus μ, that is, $2\zeta + 3\sqrt{3}\xi = \mu$ [56, 58, 59].

Following Reference [56, 68] (see Section 3 on pg. 149), the first Piola-Kirchhoff stress tensor $\boldsymbol{P}$ can be expressed as

$$\boldsymbol{P} = \boldsymbol{\Sigma_F} + \boldsymbol{\Sigma_H} \times \boldsymbol{F} + \Sigma_J \boldsymbol{H}, \tag{11}$$

where the conjugate stresses $\{\boldsymbol{\Sigma_F}, \boldsymbol{\Sigma_H}, \Sigma_J\}$ with respect to $\{\boldsymbol{F}, \boldsymbol{H}, J\}$ become

$$\boldsymbol{\Sigma_F} := \frac{\partial \hat{W}}{\partial \boldsymbol{F}} = 2\zeta J^{-2/3} \boldsymbol{F}; \qquad \boldsymbol{\Sigma_H} := \frac{\partial \hat{W}}{\partial \boldsymbol{H}} = 3\xi J^{-2} (\boldsymbol{H} : \boldsymbol{H})^{1/2} \boldsymbol{H}, \tag{12}$$

and $\Sigma_J := \hat{\Sigma}_J + p$ with

$$\hat{\Sigma}_J := \frac{\partial \hat{W}}{\partial J} = -\frac{2}{3}\zeta J^{-5/3}(\boldsymbol{F} : \boldsymbol{F}) - 2\xi J^{-3}(\boldsymbol{H} : \boldsymbol{H})^{3/2}; \qquad p := \frac{\partial U}{\partial J} = \kappa(J - 1). \tag{13}$$

It is worth noticing that the strain energy described in (9) degenerates to the case of a nearly incompressible neo-Hookean model by imposing the values of $\zeta = \frac{\mu}{2}$ and $\xi = 0$ [56].

3. Finite volume spatial discretisation

3.1. Preliminaries

In order to present the spatial discretisation procedure used in this work, some basic nomenclature will need to be introduced. For simplicity, let us consider a domain discretised with a quadrilateral mesh in two dimensions. In Fig. 2a, e represents the control volume of cell e, f represents the surface f connecting cell e and its neighbour, and a represents the node a of the underlying quadrilateral mesh. For further clarification, an exploded view of Fig. 2a is illustrated in Fig. 2b. In this figure, ef represents the elemental surface f associated with cell e and ea represents the elemental node a corresponding to any given cell e.

6

3.2. Finite volume method

Using a standard finite volume discretisation procedure [62, 71], the hyperbolic system described in (3) is spatially integrated within a given control volume (cell) e, to give

$$\frac{d\boldsymbol{\mathcal{U}}_e}{dt} = -\frac{1}{\Omega_0^e} \int_{\Omega_0^e} \frac{\partial \boldsymbol{\mathcal{F}}_I}{\partial X_I} \, d\Omega_0 + \boldsymbol{\mathcal{S}}_e. \tag{14}$$

Here, Ω_0^e denotes the material volume corresponding to cell e, $\boldsymbol{\mathcal{U}}_e$ and $\boldsymbol{\mathcal{S}}_e$ are, respectively, the average values of the conservation variables and the source term within the cell e.

Application of the classical Green-Gauss divergence theorem on the flux term of (14) results in

$$\frac{d\boldsymbol{\mathcal{U}}_e}{dt} = -\frac{1}{\Omega_0^e} \int_{\partial\Omega_0^e} \boldsymbol{\mathcal{F}}_{\boldsymbol{N}} \, dA + \boldsymbol{\mathcal{S}}_e, \tag{15}$$

with $\boldsymbol{\mathcal{F}}_{\boldsymbol{N}}$ as defined in (5). For evaluation of the surface flux integral in (15), we will restrict to integrands which require only one Gauss quadrature point (placed at the centroid of a surface) for exact integration, seeking computational efficiency of the overall scheme. With this in mind, above surface integral (15) can now be approximated by means of a Godunov-type spatial discretisation [50] as

$$\frac{d\boldsymbol{\mathcal{U}}_e}{dt} \approx -\frac{1}{\Omega_0^e} \sum_{f \in \Lambda_e^f} \boldsymbol{\mathcal{F}}_{\boldsymbol{N}_{ef}}^C(\boldsymbol{\mathcal{U}}_{ef}^-, \boldsymbol{\mathcal{U}}_{ef}^+) \, \|\boldsymbol{C}_{ef}\| + \boldsymbol{\mathcal{S}}_e, \tag{16}$$

where Λ_e^f represents the set of faces f associated with cell e, $\boldsymbol{N}_{ef} := \boldsymbol{C}_{ef}/\|\boldsymbol{C}_{ef}\|$ and $\|\boldsymbol{C}_{ef}\|$ represent the material outward unit normal vector and the surface area associated with face f of cell e, respectively, and $\boldsymbol{\mathcal{F}}_{\boldsymbol{N}_{ef}}^C$ represents the Godunov-type numerical flux evaluated at the centroid of the surface f belonging to cell e. Upper index C will be used in the remainder of this paper to emphasise the notion of interface or 'contact' flux. The accuracy of $\boldsymbol{\mathcal{F}}_{\boldsymbol{N}_{ef}}^C$ depends on the values of the left and right states of the variable $\boldsymbol{\mathcal{U}}$ at face f, namely $\boldsymbol{\mathcal{U}}_{ef}^-$ and $\boldsymbol{\mathcal{U}}_{ef}^+$.

For completeness, equation (16) can now be particularised for each individual component of $\boldsymbol{\mathcal{U}}$, yielding

$$\frac{d\boldsymbol{p}_e}{dt} = \frac{1}{\Omega_0^e} \sum_{f \in \Lambda_e^f} \boldsymbol{t}_f^C \|\boldsymbol{C}_{ef}\| + \rho_0 \boldsymbol{b}_e; \tag{17a}$$

$$\frac{d\boldsymbol{F}_e}{dt} = \frac{1}{\Omega_0^e} \sum_{f \in \Lambda_e^f} \frac{\boldsymbol{p}_f^C}{\rho_0} \otimes \boldsymbol{C}_{ef}; \tag{17b}$$

$$\frac{d\boldsymbol{H}_e}{dt} = \boldsymbol{F}_e \times \frac{1}{\Omega_0^e} \sum_{f \in \Lambda_e^f} \frac{\boldsymbol{p}_f^C}{\rho_0} \otimes \boldsymbol{C}_{ef}; \tag{17c}$$

$$\frac{dJ_e}{dt} = \boldsymbol{H}_e : \frac{1}{\Omega_0^e} \sum_{f \in \Lambda_e^f} \frac{\boldsymbol{p}_f^C}{\rho_0} \otimes \boldsymbol{C}_{ef}; \tag{17d}$$

$$\frac{dE_e}{dt} = \frac{1}{\Omega_0^e} \sum_{f \in \Lambda_e^f} \left(\frac{\boldsymbol{p}_f^C}{\rho_0} \cdot \boldsymbol{t}_f^C \right) \|\boldsymbol{C}_{ef}\|, \tag{17e}$$

where $\{\boldsymbol{t}_f^C, \boldsymbol{p}_f^C\}$ are the Godunov-type numerical approximation [1] for traction and linear momentum. The new supplemented geometric strain updates for $\boldsymbol{H}$ (17c) and J (17d) are obtained through the use of the non-conservative form of the differential equations presented in (8). As a result, the updates of (17c) and (17d) now exclusively depend on the evaluation of $\boldsymbol{p}_f^C$, exactly in the same way as those presented in (17b) for the fibre map evolution.

7

Finally, the current deformed geometry can be recovered by integrating in time the discrete (cell-based) velocity field

$$\frac{d\boldsymbol{x}_e}{dt} = \frac{\boldsymbol{p}_e}{\rho_0}. \tag{18}$$

In order to guarantee the existence of a single-valued deformation mapping $\boldsymbol{\phi}$, the time evolution of $\{\boldsymbol{F}_e, \boldsymbol{H}_e\}$ in (17b-17c) must ensure the discrete satisfaction of a set of compatibility conditions (also known as involutions [60, 72]) in time

$$\mathrm{CURL}\dot{\boldsymbol{F}}_e = \boldsymbol{0}; \qquad \mathrm{DIV}\dot{\boldsymbol{H}}_e = \boldsymbol{0}, \tag{19}$$

where overdot represents differentiation with respect to time. Above conditions need only be satisfied by the time evolution operator provided that they are met by the initial conditions [60]. This implies that expression (19), as opposed to a classical constraint, is not necessary to close the system of conservation laws, but must be an inherent property of the evolution operator. This will be presented in Section 6.

Remark 1: As presented in Ref. [1], the spatial discretisation of Eq. (16) can be alternatively expressed in terms of so-called nodal fluxes $\boldsymbol{\mathcal{F}}_{\boldsymbol{N}_{ea}}^C$ (see Fig. 3b) [2, 40, 44]

$$\frac{d\boldsymbol{\mathcal{U}}_e}{dt} = -\frac{1}{\Omega_0^e} \sum_{a \in \Lambda_e^a} \boldsymbol{\mathcal{F}}_{\boldsymbol{N}_{ea}}^C(\boldsymbol{\mathcal{U}}_{ea}^-, \boldsymbol{\mathcal{U}}_{ea}^+) \, \|\boldsymbol{C}_{ea}\| + \boldsymbol{\mathcal{S}}_e, \tag{20}$$

where the material nodal area normal vector $\boldsymbol{C}_{ea}$ is defined as $\boldsymbol{C}_{ea} := \sum_{f \in \Lambda_a^f} \left(\frac{1}{\Lambda_f^a} \boldsymbol{C}_{ef}\right)$ [2, 40–42, 44, 67]. Here, Λ_e^a and Λ_f^a represent the number of nodes a associated with cell e and face f, respectively, Λ_a^f represents the set of faces f corresponding to node a and $\boldsymbol{N}_{ea} := \boldsymbol{C}_{ea}/\|\boldsymbol{C}_{ea}\|$ represents the material outward nodal unit normal vector. For completeness, the system of semi-discrete nodal updates for the enhanced $\{\boldsymbol{p}, \boldsymbol{F}, \boldsymbol{H}, J\}$ formulation presented in this paper, named eXtended GLACE (X-GLACE), reads

$$\frac{d\boldsymbol{p}_e}{dt} = \frac{1}{\Omega_0^e} \sum_{a \in \Lambda_e^a} \boldsymbol{t}_{ea}^C \|\boldsymbol{C}_{ea}\| + \rho_0 \boldsymbol{b}_e; \tag{21a}$$

$$\frac{d\boldsymbol{F}_e}{dt} = \frac{1}{\Omega_0^e} \sum_{a \in \Lambda_e^a} \frac{\boldsymbol{p}_a^C}{\rho_0} \otimes \boldsymbol{C}_{ea}; \tag{21b}$$

$$\frac{d\boldsymbol{H}_e}{dt} = \boldsymbol{F}_e \times \frac{1}{\Omega_0^e} \sum_{a \in \Lambda_e^a} \frac{\boldsymbol{p}_a^C}{\rho_0} \otimes \boldsymbol{C}_{ea}; \tag{21c}$$

$$\frac{dJ_e}{dt} = \boldsymbol{H}_e : \frac{1}{\Omega_0^e} \sum_{a \in \Lambda_e^a} \frac{\boldsymbol{p}_a^C}{\rho_0} \otimes \boldsymbol{C}_{ea}; \tag{21d}$$

$$\frac{dE_e}{dt} = \frac{1}{\Omega_0^e} \sum_{a \in \Lambda_e^a} \left(\frac{\boldsymbol{p}_a^C}{\rho_0} \cdot \boldsymbol{t}_{ea}^C\right) \|\boldsymbol{C}_{ea}\|. \tag{21e}$$

Finally, the current deformed geometry $\boldsymbol{x}$ can be simply recovered through time integration of the discrete (node based) velocity as

$$\frac{d\boldsymbol{x}_a}{dt} = \frac{\boldsymbol{p}_a^C}{\rho_0}. \tag{22}$$

Given the fact that the discrete velocity field expressed in terms of its nodal values is continuous across the entire computational domain, the material curl of (21b) is thus naturally curl-free, and so is the material
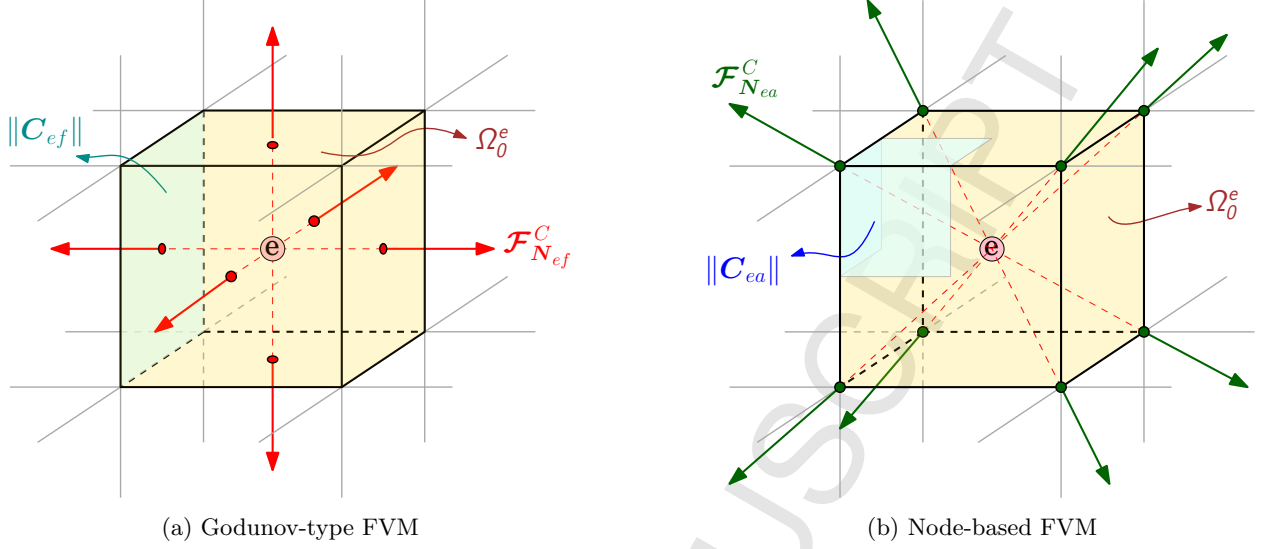
8

Figure 3: Two families of cell centred Finite Volume Methods: (a) Godunov-type FVM; and (b) node-based FVM.

divergence of (21c), as their updates are formulated in terms of a discrete gradient of a continuous field [72].

For evaluation of the interface values $\boldsymbol{\mathcal{U}}_{ef}^{+;-}$ described in (16) (or $\boldsymbol{\mathcal{U}}_{ea}^{+;-}$ in (20)), it is well known that a piecewise constant approximation of the Godunov-type scheme leads to excessive numerical dissipation [73, 74]. The physics of the problem can no longer be captured accurately unless excessively fine meshes are used, which is clearly undesirable. To overcome this drawback, and to guarantee second order accuracy in space, a linear reconstruction procedure in conjunction with an appropriate slope limiter is used. A detailed discussion of this monotone reconstruction procedure can be found in Ref. [1].

The remaining unknowns to be discussed in equations (17a-18) (or (21a-22)) are the Godunov-type numerical flux evaluation for $\{\boldsymbol{t}_f^C, \boldsymbol{p}_f^C\}$ (or node based numerical flux approximation for $\{\boldsymbol{t}_{ea}^C, \boldsymbol{p}_a^C\}$). This can be approximated via an acoustic Riemann solver and will be discussed in the following section.

4. Riemann solver

4.1. General remark

The finite volume spatial discretisation procedure presented in this paper requires an approximate Riemann solver [62] for the evaluation of $\{\boldsymbol{t}_f^C, \boldsymbol{p}_f^C\}$ in (17a-18) (or $\{\boldsymbol{t}_{ea}^C, \boldsymbol{p}_a^C\}$ in (21a-22)). To achieve this, recall first that the numerical interface (contact) flux across a discontinuous surface with normal $\boldsymbol{N}_{ef}$, namely $\boldsymbol{\mathcal{F}}_{\boldsymbol{N}_{ef}}^C$, is generally described as [71, 73]

$$\boldsymbol{\mathcal{F}}_{\boldsymbol{N}_{ef}}^C = \underbrace{\frac{1}{2}\left[\boldsymbol{\mathcal{F}}_{\boldsymbol{N}_{ef}}(\boldsymbol{\mathcal{U}}_f^-) + \boldsymbol{\mathcal{F}}_{\boldsymbol{N}_{ef}}(\boldsymbol{\mathcal{U}}_f^+)\right]}_{\text{Unstable flux}} \underbrace{-\frac{1}{2}\int_{\boldsymbol{\mathcal{U}}_f^-}^{\boldsymbol{\mathcal{U}}_f^+}|\boldsymbol{\mathcal{A}}_{\boldsymbol{N}_{ef}}|\,\mathrm{d}\boldsymbol{\mathcal{U}}}_{\text{Upwinding stabilisation}}, \tag{23}$$

where the absolute value component of the flux Jacobian matrix being defined as $|\boldsymbol{\mathcal{A}}_{\boldsymbol{N}_{ef}}| := \left|\frac{\partial \boldsymbol{\mathcal{F}}_{\boldsymbol{N}_{ef}}}{\partial \boldsymbol{\mathcal{U}}}\right| = \frac{1}{2}\sum_{\alpha=1}^{6}|c_\alpha|\boldsymbol{\mathcal{R}}_\alpha \boldsymbol{\mathcal{L}}_\alpha^T$ (refer to Appendix A).

In this work, evaluation of $|\boldsymbol{\mathcal{A}}_{\boldsymbol{N}_{ef}}|$ is carried out at the initial undeformed configuration (i.e. origin) by adopting $\boldsymbol{F} = \boldsymbol{H} = \boldsymbol{I}$ and $J = 1$. For this reason, the above numerical interface flux (23) can be

9

reduced to

$$\mathcal{F}^C_{\boldsymbol{N}_{ef}} = \underbrace{\frac{1}{2}\left[\boldsymbol{\mathcal{F}}_{\boldsymbol{N}_{ef}}(\boldsymbol{\mathcal{U}}^-_f) + \boldsymbol{\mathcal{F}}_{\boldsymbol{N}_{ef}}(\boldsymbol{\mathcal{U}}^+_f)\right]}_{\text{Unstable flux}} \underbrace{-\frac{1}{2}|\boldsymbol{\mathcal{A}}_{\boldsymbol{N}_{ef}}|\left(\boldsymbol{\mathcal{U}}^+_f - \boldsymbol{\mathcal{U}}^-_f\right)}_{\text{Upwinding stabilisation}}. \tag{24}$$

The first term on the right hand side of (24) denotes the unstable flux, whereas the second term (i.e. upwinding stabilisation) can be interpreted as a numerical stabilisation that counterbalances non-physical instabilities arising from the first term. A detailed derivation of the upwinding stabilisation term in (24) can be found in Reference [1] (see pg. 417 to pg. 420 in Section 4.3).

Following the exact same procedure presented in Reference [1], and after some algebraic manipulations, the Godunov-type numerical traction and linear momentum can be summarised here for completeness

$$\boldsymbol{t}^C_f = \boldsymbol{t}^{\text{Ave}}_f + \boldsymbol{t}^{\text{Stab}}_f; \qquad \boldsymbol{p}^C_f = \boldsymbol{p}^{\text{Ave}}_f + \boldsymbol{p}^{\text{Stab}}_f. \tag{25}$$

The average (unstable) states of both the traction and linear momentum are

$$\boldsymbol{t}^{\text{Ave}}_f := \frac{1}{2}(\boldsymbol{t}^-_f + \boldsymbol{t}^+_f); \qquad \boldsymbol{p}^{\text{Ave}}_f := \frac{1}{2}(\boldsymbol{p}^-_f + \boldsymbol{p}^+_f), \tag{26}$$

and the corresponding upwinding stabilisation terms are

$$\boldsymbol{t}^{\text{Stab}}_f := \frac{1}{2}\boldsymbol{S}^{\boldsymbol{p}}_{ef}(\boldsymbol{p}^+_f - \boldsymbol{p}^-_f); \qquad \boldsymbol{p}^{\text{Stab}}_f := \frac{1}{2}\boldsymbol{S}^{\boldsymbol{t}}_{ef}(\boldsymbol{t}^+_f - \boldsymbol{t}^-_f), \tag{27}$$

with the (acoustic) stabilisation matrices being defined as

$$\boldsymbol{S}^{\boldsymbol{t}}_{ef} := \left[\frac{1}{c_p}(\boldsymbol{n}_{ef} \otimes \boldsymbol{n}_{ef}) + \frac{1}{c_s}(\boldsymbol{I} - \boldsymbol{n}_{ef} \otimes \boldsymbol{n}_{ef})\right]; \qquad \boldsymbol{S}^{\boldsymbol{p}}_{ef} := \left[c_p(\boldsymbol{n}_{ef} \otimes \boldsymbol{n}_{ef}) + c_s(\boldsymbol{I} - \boldsymbol{n}_{ef} \otimes \boldsymbol{n}_{ef})\right]. \tag{28}$$

In this case, c_p and c_s represent the elastic pressure wave speed and the elastic shear wave speed

$$c_p := \sqrt{\frac{\lambda + 2\mu}{\rho_0}}; \qquad c_s := \sqrt{\frac{\mu}{\rho_0}}, \tag{29}$$

respectively.

Remark 2: In the case of the nodal scheme [39–42, 44, 67], the nodal linear momentum $\boldsymbol{p}_a$ can first be obtained by solving the following system of equations (see Section 6.2.2 on pg. 423-426 in Ref. [1])

$$\boldsymbol{A}_a \boldsymbol{p}^C_a = \boldsymbol{b}_a, \tag{30}$$

where

$$\boldsymbol{A}_a = \sum_{e \in \Lambda^e_a} \|\boldsymbol{C}_{ea}\| \boldsymbol{S}^{\boldsymbol{p}}_{ea}; \qquad \boldsymbol{b}_a = \sum_{e \in \Lambda^e_a} \|\boldsymbol{C}_{ea}\| \boldsymbol{S}^{\boldsymbol{p}}_{ea} \boldsymbol{p}_{ea} - \sum_{e \in \Lambda^e_a} \boldsymbol{P}_{ea} \boldsymbol{C}_{ea}. \tag{31}$$

The elemental nodal traction $\boldsymbol{t}^C_{ea}$ then follows as

$$\boldsymbol{t}^C_{ea} := \boldsymbol{P}^C_{ea} \boldsymbol{N}_{ea} = \boldsymbol{P}_{ea} \boldsymbol{N}_{ea} + \boldsymbol{S}^{\boldsymbol{p}}_{ea}\left(\boldsymbol{p}^C_a - \boldsymbol{p}_{ea}\right). \tag{32}$$

Notice that the above stabilisation matrix $\boldsymbol{S}^{\boldsymbol{p}}_{ea}$ is identical to $\boldsymbol{S}^{\boldsymbol{p}}_{ef}$ presented in (28), but replacing the subscript of ef with ea since $\boldsymbol{n}_{ef} \neq \boldsymbol{n}_{ea}$.

4.2. Preconditioned dissipation

As will be shown in the numerical examples of this paper, the acoustic Riemann solver previously presented is inefficient in the region of near incompressibility when the value of $\frac{\kappa}{\mu}$ tends to infinity. One possibility to rectify this numerical shortcoming is the introduction of a preconditioning for the numerical dissipation [63–65], which aims to recover a correct scaling for the stabilisation matrices $\{\boldsymbol{S}_{ef}^{\boldsymbol{t}}, \boldsymbol{S}_{ef}^{\boldsymbol{p}}\}$ in (28). To achieve this, the upwinding stabilisation term of the flux approximation $\boldsymbol{\mathcal{F}}_{\boldsymbol{N}_{ef}}^{C}$ described in (24) can be modified by preconditioning [63–65], resulting in

$$\boldsymbol{\mathcal{F}}_{\boldsymbol{N}_{ef}}^{C} = \frac{1}{2}\left[\boldsymbol{\mathcal{F}}_{\boldsymbol{N}_{ef}}(\boldsymbol{\mathcal{U}}_{f}^{-}) + \boldsymbol{\mathcal{F}}_{\boldsymbol{N}_{ef}}(\boldsymbol{\mathcal{U}}_{f}^{+})\right] - \frac{1}{2}\boldsymbol{\mathcal{P}}^{-1}|\boldsymbol{\mathcal{P}}\boldsymbol{\mathcal{A}}_{\boldsymbol{N}_{ef}}|\left(\boldsymbol{\mathcal{U}}_{f}^{+} - \boldsymbol{\mathcal{U}}_{f}^{-}\right), \tag{33}$$

where $\boldsymbol{\mathcal{P}}$ is a preconditioning matrix. With respect to the original flux computation (24), only the upwinding stabilisation terms (also known as high order corrections) are altered and thus, the finite volume spatial discretisation procedure presented in Section 3 still remains a consistent approximation for the enhanced $\{\boldsymbol{p}, \boldsymbol{F}, \boldsymbol{H}, J\}$ system.

In this paper, a very simple (diagonal) preconditioner is postulated

$$\boldsymbol{\mathcal{P}} = \begin{bmatrix} \boldsymbol{I} & \boldsymbol{0} & \boldsymbol{0} & \boldsymbol{0} \\ \boldsymbol{0} & \beta^2\boldsymbol{I} & \boldsymbol{0} & \boldsymbol{0} \\ \boldsymbol{0} & \boldsymbol{0} & \beta^2\boldsymbol{I} & \boldsymbol{0} \\ \boldsymbol{0} & \boldsymbol{0} & \boldsymbol{0} & \frac{1}{\beta^2} \end{bmatrix}, \tag{34}$$

where the dimensionless parameter β is defined as $\beta := \frac{\tilde{\kappa}}{\kappa}$ and $\tilde{\kappa}$ is a user-defined material constant, usually taken in the neighbourhood of the bulk modulus κ of the material. The aim of this diagonal preconditioner (34) is to re-scale the stabilisation coefficients of the system (i.e. c_p and c_s wave speeds) by means of the dimensionless ratio $\frac{\tilde{\kappa}}{\kappa}$, without altering the characteristic structure (i.e. streamline direction) of the upwinding method.

Remark 3: This simple preconditioner approach leads to a numerical scheme which can remind of the artificial compressibility (AC) method [75, 76]. However, it is important to realise that contrary to the AC method, the preconditioner only acts on the upwinding stabilisation flux and not on the averaging flux. Hence, the size of the time step will still be dictated by the real volumetric wave speed. In the AC approach, originally designed to deal with incompressible flows, the averaging flux is also modified as a new (artificial) nearly incompressible constitutive law is put forward.

Referring to Appendix A, three pairs of non-zero eigenvalues corresponding to the volumetric and shear waves are modified accordingly as

$$c_{1,2} = \pm\tilde{c}_p, \quad \tilde{c}_p = \frac{1}{\beta}\sqrt{\frac{\lambda + \mu(\beta^4 + 1)}{\rho_0}}; \qquad c_{3,4} = c_{5,6} = \pm\tilde{c}_s, \quad \tilde{c}_s = \beta\sqrt{\frac{\mu}{\rho_0}}. \tag{35}$$

In the case of near incompressibility, the stabilisation matrices (28) must be re-scaled by replacing $\{c_p, c_s\}$ with $\{\tilde{c}_p, \tilde{c}_s\}$ presented in (35). Notice that the original elastic pressure wave speed c_p (29a) and shear wave speed c_s (29b) can be simply recovered by equating the value of $\tilde{\kappa}$ with the bulk modulus κ of the material.

5. Time integration

In order to update in time the resulting set of semi-discrete equations described in (17a-18) (or (21a-22)), an explicit one-step two-stage Total Variation Diminishing Runge-Kutta (TVD-RK) time integrator

11

has been used [1, 50–52, 77]. This is described by the following time update equations from time step t^n to t^{n+1}

$$\boldsymbol{\mathcal{U}}_e^\star = \boldsymbol{\mathcal{U}}_e^n + \Delta t\, \dot{\boldsymbol{\mathcal{U}}}_e^n(\boldsymbol{\mathcal{U}}_e^n, t^n);$$ (36a)

$$\boldsymbol{\mathcal{U}}_e^{\star\star} = \boldsymbol{\mathcal{U}}_e^\star + \Delta t\, \dot{\boldsymbol{\mathcal{U}}}_e^\star(\boldsymbol{\mathcal{U}}_e^\star, t^{n+1});$$ (36b)

$$\boldsymbol{\mathcal{U}}_e^{n+1} = \frac{1}{2}(\boldsymbol{\mathcal{U}}_e^n + \boldsymbol{\mathcal{U}}_e^{\star\star}).$$ (36c)

The maximum time step $\Delta t := t^{n+1} - t^n$ is governed by a standard Courant-Friedrichs-Lewy (CFL) condition [78] to be computed as

$$\Delta t = \alpha_{\mathrm{CFL}}\, \frac{h_{\min}}{c_{p,\max}},$$ (37)

where $c_{p,\max}$ is the maximum p-wave speed, $h_{\min}$ is the minimum (or characteristic) length within the computational domain and α_{CFL} is the CFL stability number. For the numerical computations presented in this manuscript, a value of $\alpha_{\mathrm{CFL}} = 0.3$ has been chosen to ensure both accuracy and stability of the algorithm [50].

In this paper, the first Piola–Kirchhoff stress tensor is expressed as a function of a set of (weakly related) geometric strain measures, that is $\boldsymbol{P} = \boldsymbol{P}(\boldsymbol{F}, \boldsymbol{H}, J)$. Thus, the resulting system does not intrinsically fulfil conservation of angular momentum. In order to rectify this, a global a posteriori projection procedure as that presented in [1] (see Section 7 on pg. 429-432) is introduced and, moreover, has also been adapted to the node based Total Lagrangian X-GLACE scheme.

6. Involutions

One of the challenging issues in the process of the time-evolving expressions (17b-17c) is the ability to control the onset and propagation of spurious mechanisms over a long term response. Following recent work by the authors [1], two different strategies are used in this work where the geometric strain updates for $\{\boldsymbol{F}, \boldsymbol{H}\}$ described in (17b-17c) are solved subjected to the fulfilment of specific involutions (7) [1, 50, 61].

The first algorithm, named Constrained-TOUCH (C-TOUCH), is based on the use of a constrained transport algorithm [1], where the spatial discretisation is tailor-made to discretely satisfy the involutions by construction. In this approach, the evolution of $\boldsymbol{F}$ and $\boldsymbol{H}$ is re-formulated in terms of a material discrete gradient of a continuous velocity field. This can be achieved by replacing the Godunov-type numerical linear momentum $\boldsymbol{p}_f^C$ described in (17b-17d) with a projected linear momentum $\tilde{\boldsymbol{p}}_f^C$, ensuring that this specific update exactly coincides with the classical finite element discretisation when considering linear interpolation with only one Gauss quadrature point at the centroid of the element [1, 50]. The whole process for the computation of $\tilde{\boldsymbol{p}}_f^C$ is illustrated in Algorithm 2 of Reference [1] (see pg. 423 in Section 6.2.1).

The second algorithm, named Penalised-TOUCH (P-TOUCH), relies on the explicit addition of a residual based artificial dissipation to the evolution equations of $\{\boldsymbol{F}, \boldsymbol{H}\}$. The main aim of this approach is to control the accumulation of non-physical involution errors, whilst still preserving the standard finite volume update for the fibre map (17b) and area map (17c) equations, without the need to resort to projecting interface values of the linear momentum. In this case, a geometrical penalisation of the time-integrated fibre map equation is added to (17b), which gives

$$\boldsymbol{F}_e^{n+1} = \boldsymbol{F}_e^n + \frac{\Delta t}{\Omega_0^e} \sum_{f \in \Lambda_e^f} \left(\frac{\boldsymbol{p}_f^{C,n}}{\rho_0} \right) \otimes \boldsymbol{C}_{ef} + \xi_{\boldsymbol{F}} \underbrace{[\boldsymbol{\nabla}_0 \boldsymbol{x}_e^n - \boldsymbol{F}_e^n]}_{\text{Penalisation}}.$$ (38)

12

Similarly, another geometrical penalisation of the time-integrated area map equation can also be incorporated in (17c)

$$\boldsymbol{H}_e^{n+1} = \boldsymbol{H}_e^n + \frac{\Delta t}{\Omega_0^e} \left[\boldsymbol{F}_e^n \times \sum_{f \in \Lambda_e^f} \left(\frac{\boldsymbol{p}_f^{C,n}}{\rho_0} \right) \otimes \boldsymbol{C}_{ef} \right] + \xi_{\boldsymbol{H}} \underbrace{\left[\frac{1}{2} \left(\boldsymbol{\nabla}_0 \boldsymbol{x}_e^n \times \boldsymbol{\nabla}_0 \boldsymbol{x}_e^n \right) - \boldsymbol{H}_e^n \right]}_{\text{Penalisation}}, \qquad (39)$$

where $\boldsymbol{\nabla}_0 \boldsymbol{x}_e^n := \frac{1}{\Omega_0^e} \sum_{f \in \Lambda_e^f} \boldsymbol{x}_f^n \otimes \boldsymbol{C}_{ef}$ and the non-dimensional parameters $\{\xi_{\boldsymbol{F}}, \xi_{\boldsymbol{H}}\}$ are usually defined in the range of $[0, 0.5]$ [53–57, 59]. By setting the values of $\xi_{\boldsymbol{F}} = \xi_{\boldsymbol{H}} = 0$, the standard finite volume update presented in (17b) and (17c) can be recovered.

7. Algorithmic description

For ease of understanding, Algorithm 1 summarises the complete algorithmic description of the following three methodologies, namely: (a) $\{\boldsymbol{p}, \boldsymbol{F}, \boldsymbol{H}, J\}$ C-TOUCH, (b) $\{\boldsymbol{p}, \boldsymbol{F}, \boldsymbol{H}, J\}$ P-TOUCH and (c) $\{\boldsymbol{p}, \boldsymbol{F}, \boldsymbol{H}, J\}$ X-GLACE.

8. Numerical examples

In this section, a series of challenging numerical examples is presented in order to assess the accuracy, robustness and efficiency of the proposed $\{\boldsymbol{p}, \boldsymbol{F}, \boldsymbol{H}, J\}$ mixed-based methodologies, namely: (a) C-TOUCH, (b) P-TOUCH and (c) X-GLACE. In this paper, we exclusively focus on the simulation of isothermal processes that enable the total energy E of the system to be decoupled from the rest of the system equations. This energy balance principle (1e) however can still be employed to measure the numerical dissipation of the proposed methodologies.

In the following numerical computations, a piecewise linear reconstruction procedure (see Section 4.2.1 on. pg. 416-417 of [1]), Barth Jespersen slope limiter (see Section 4.2.2 on pg. 417 of [1]) and the global a posteriori angular momentum projection algorithm (see Section 7 on pg. 429-432 of [1]) are activated unless otherwise stated.

8.1. Convergence

The main objective of this example is to assess the convergence behaviour of the following three $\{\boldsymbol{p}, \boldsymbol{F}, \boldsymbol{H}, J\}$ methodologies, namely C-TOUCH, P-TOUCH and X-GLACE. A unit cube is considered (see Fig. 4a) with symmetric boundary conditions (restricted normal displacement) at faces $X = 0$, $Y = 0$ and $Z = 0$ and skew-symmetric boundary conditions (restricted tangential displacement) at faces $X = 1 \, \text{m}$, $Y = 1 \, \text{m}$ and $Z = 1 \, \text{m}$. For small deformations, the problem has a closed-form displacement field of the form [1, 47, 50–52, 54, 56–59, 79]

$$\boldsymbol{u}(\boldsymbol{X}, t) = U_0 \cos \left(\frac{\sqrt{3}}{2} c_d \pi t \right) \begin{bmatrix} A \sin \left(\frac{\pi X_1}{2} \right) \cos \left(\frac{\pi X_2}{2} \right) \cos \left(\frac{\pi X_3}{2} \right) \\ B \cos \left(\frac{\pi X_1}{2} \right) \sin \left(\frac{\pi X_2}{2} \right) \cos \left(\frac{\pi X_3}{2} \right) \\ C \cos \left(\frac{\pi X_1}{2} \right) \cos \left(\frac{\pi X_2}{2} \right) \sin \left(\frac{\pi X_3}{2} \right) \end{bmatrix} ; \quad c_d = \sqrt{\frac{\lambda + 2\mu}{\rho_0}}. \qquad (40)$$

Parameters $\{A, B, C\}$ are user-defined arbitrary constants, chosen such that $A=B=C$ which ensures the existence of a non-zero pressure field. For values of $U_0 < 0.001$ m, the solution can be considered to be linear and the closed-form expression (40) holds. The problem is initialised with the displacement field $\boldsymbol{u}^0 \equiv \boldsymbol{u}(\boldsymbol{X}, 0)$ according to Eq. (40) (see Fig. 4b) and subsequently, the initial deformation gradient, its co-factor and its Jacobian can be obtained as $\boldsymbol{F}^0 = \boldsymbol{I} + \boldsymbol{\nabla}_0 \boldsymbol{u}^0$, $\boldsymbol{H}^0 = \frac{1}{2} \boldsymbol{F}^0 \times \boldsymbol{F}^0$ and $J^0 = \frac{1}{6} (\boldsymbol{F}^0 \times \boldsymbol{F}^0) : \boldsymbol{F}^0$. A linear elastic material is chosen with a Poisson's ratio of $\nu = (1 - \mu/\kappa)/2 = 0.3$, Young's modulus $E = 17$ MPa and density $\rho_0 = 1100$ kg/m³. The solution parameters are set as $A=B=C=1$ and $U_0 = 5 \times 10^{-4}$ m.

13

Algorithm 1: Time update of conservation variables

Input : $\boldsymbol{\mathcal{U}}_e^n$ where $\boldsymbol{\mathcal{U}} = [\boldsymbol{p}\ \boldsymbol{F}\ \boldsymbol{H}\ J\ E]^T$

Output: $\boldsymbol{\mathcal{U}}_e^{n+1}$, $\boldsymbol{P}_e^{n+1}$

(1) Calculate time increment: $\Delta t^n \leftarrow$ Eq. (37)

(2) Store conservation variables: $\boldsymbol{\mathcal{U}}_e^{\mathrm{old}} = \boldsymbol{\mathcal{U}}_e^n$

for Runge Kutta stage $= 1$ **to** 2 **do**

     (3) Evaluate wave speeds: $\tilde{c}_p,\ \tilde{c}_s \leftarrow$ Eq. (35)

     (4) Apply linear reconstruction procedure: Sections 4.2.1 & 4.2.2 in Ref. [1]

     (5) Apply acoustic Riemann solver:

         if (algorithm = TOUCH) **then**

                 • Calculate face fluxes: $\boldsymbol{p}_f^C,\ \boldsymbol{t}_f^C \leftarrow$ Eq. (25)

                 • Compute projected contact linear momentum: $\tilde{\boldsymbol{p}}_f^C \leftarrow$ Section 6.2.1 in Ref. [1]

                 • Compute nodal linear momentum: $\boldsymbol{p}_a \leftarrow$ Section 6.2.1 in Ref. [1]

         else if (algorithm = X$-$GLACE) **then**

                 • Calculate nodal fluxes: $\boldsymbol{p}_a^C,\ \boldsymbol{t}_{ea}^C \leftarrow$ Eqs. (30) and (32)

         end

     (6) Enforce strong boundary conditions on nodal linear momentum $\boldsymbol{p}_a$ or $\boldsymbol{p}_a^C$

     (7) Apply angular momentum projection algorithm: Section 7 on pg. 429 in Ref. [1]

     (8) Solve governing equations:

         if (algorithm = C$-$TOUCH) **then**

                 • $\boldsymbol{\mathcal{U}}_e = \boldsymbol{\mathcal{U}}_e + \Delta t^n \dot{\boldsymbol{\mathcal{U}}}_e \left(\tilde{\boldsymbol{p}}_f^C, \boldsymbol{t}_f^C \right)$

         else if (algorithm = P$-$TOUCH) **then**

                 • $\boldsymbol{\mathcal{U}}_e = \boldsymbol{\mathcal{U}}_e + \Delta t^n \dot{\boldsymbol{\mathcal{U}}}_e \left(\boldsymbol{p}_f^C, \boldsymbol{t}_f^C \right)\ \leftarrow$ Eqs. (17a)$-$(17e) and (18)

                 • $\boldsymbol{F}_e = \boldsymbol{F}_e \left(1 - \xi_{\boldsymbol{F}} \right) + \xi_{\boldsymbol{F}} \left(\boldsymbol{\nabla}_0 \boldsymbol{x} \right)_e$

                 • $\boldsymbol{H}_e = \boldsymbol{H}_e \left(1 - \xi_{\boldsymbol{H}} \right) + \frac{1}{2} \xi_{\boldsymbol{H}} \left(\boldsymbol{\nabla}_0 \boldsymbol{x} \times \boldsymbol{\nabla}_0 \boldsymbol{x} \right)_e$

         else if (algorithm = X$-$GLACE) **then**

                 • $\boldsymbol{\mathcal{U}}_e = \boldsymbol{\mathcal{U}}_e + \Delta t^n \dot{\boldsymbol{\mathcal{U}}}_e \left(\boldsymbol{p}_a^C, \boldsymbol{t}_{ea}^C \right)\ \leftarrow$ Eqs. (30)$-$(32)

         end

end

(9) Update conservation variables: $\boldsymbol{\mathcal{U}}_e^{n+1} = \frac{1}{2}(\boldsymbol{\mathcal{U}}_e + \boldsymbol{\mathcal{U}}_e^{\mathrm{old}})$

(10) Compute PK1 stresses: $\boldsymbol{P}_e^{n+1} \leftarrow$ Eq. (11)

14

Fig. 5 shows the expected second order convergence pattern (e.g. L^1 and L^2 norm errors) of the velocity $\boldsymbol{v}$ and the first Piola-Kirchhoff stress tensor $\boldsymbol{P}$, as compared to the closed-form solution described in Eq. (40) [3]. It can be clearly seen that the C-TOUCH and P-TOUCH schemes produce practically identical convergence patterns for both velocities and stresses. Their solutions are slightly more accurate than the results obtained from the X-GLACE scheme, as can be observed by noticing the higher translation error in the convergence patterns.

8.2. Momentum conservation

Following Reference [80], the motion of a satellite-like structure is studied in order to demonstrate the momentum conservation characteristics of the proposed algorithm. The structure consists of a central cylindrical section of diameter $D = 1.5$ m and height $H = 3$ m, along with four attached arms of cross-section 1×1 m^2 that extend 6.5 m from the center of the structure (see Fig. 6a). The problem is simulated with an initial angular velocity field $\boldsymbol{\omega}_0 = [0, 0, 1]^T$ rad/s resulting in an initial velocity distribution shown in Fig. 6b. A neo-Hookean constitutive model is chosen to model the structure with material parameters defined by density $\rho_0 = 1000$ kg/m^3, Young's modulus $E = 50.05$ kPa and Poisson's ratio $\nu = 0.3$.

The time evolution of the deformation along with the expected smooth pressure representation is shown in Fig. 7. It can be observed that the arms of the structure undergo large deformation without experiencing spurious hourglassing-like modes. The cylindrical part of the structure is however dominated by a rotational motion. Additionally, a mesh refinement study with respect to both the deformation pattern and pressure resolution is presented in Fig. 8. Sequentially refined meshes of 4032, 16960 and 51336 hexahedral elements are used with the purpose to compare resolution of the deformed structure at time $t = 5.5$ s. The use of finest mesh produces a very similar deformation pattern to that of the coarsest mesh, but with a noticeably better pressure representation at the bending region of the four arms. Figs. 9 and 10 show the time history of the components of the global linear and angular momenta of the system, simulated using both C-TOUCH and X-GLACE schemes. As expected, the global linear momentum fluctuates around zero machine accuracy, whereas the angular momentum is perfectly conserved with the use of angular momentum projection algorithm. Otherwise, significant reduction in angular momentum

(a) Configuration

(b) Initial deformed state and mesh
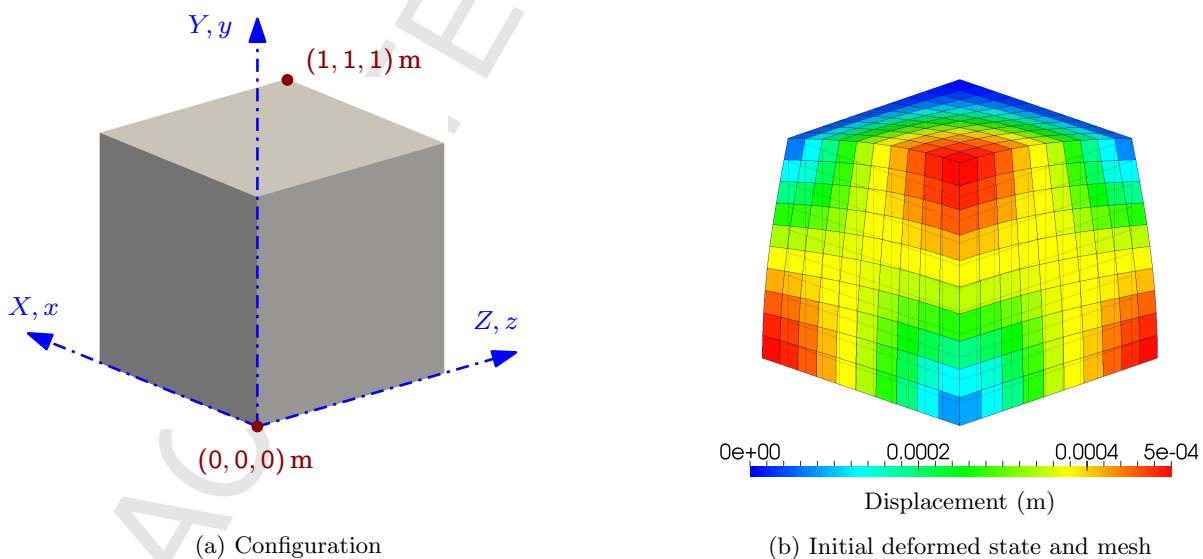
Figure 4: Low dispersion cube: Problem setup.

---

[3] Given the fact that $A=B=C$, all the three components of velocities and stresses are of the same magnitude (i.e. $v_x=v_y=v_z$ and $P_{xx}=P_{yy}=P_{zz}$).
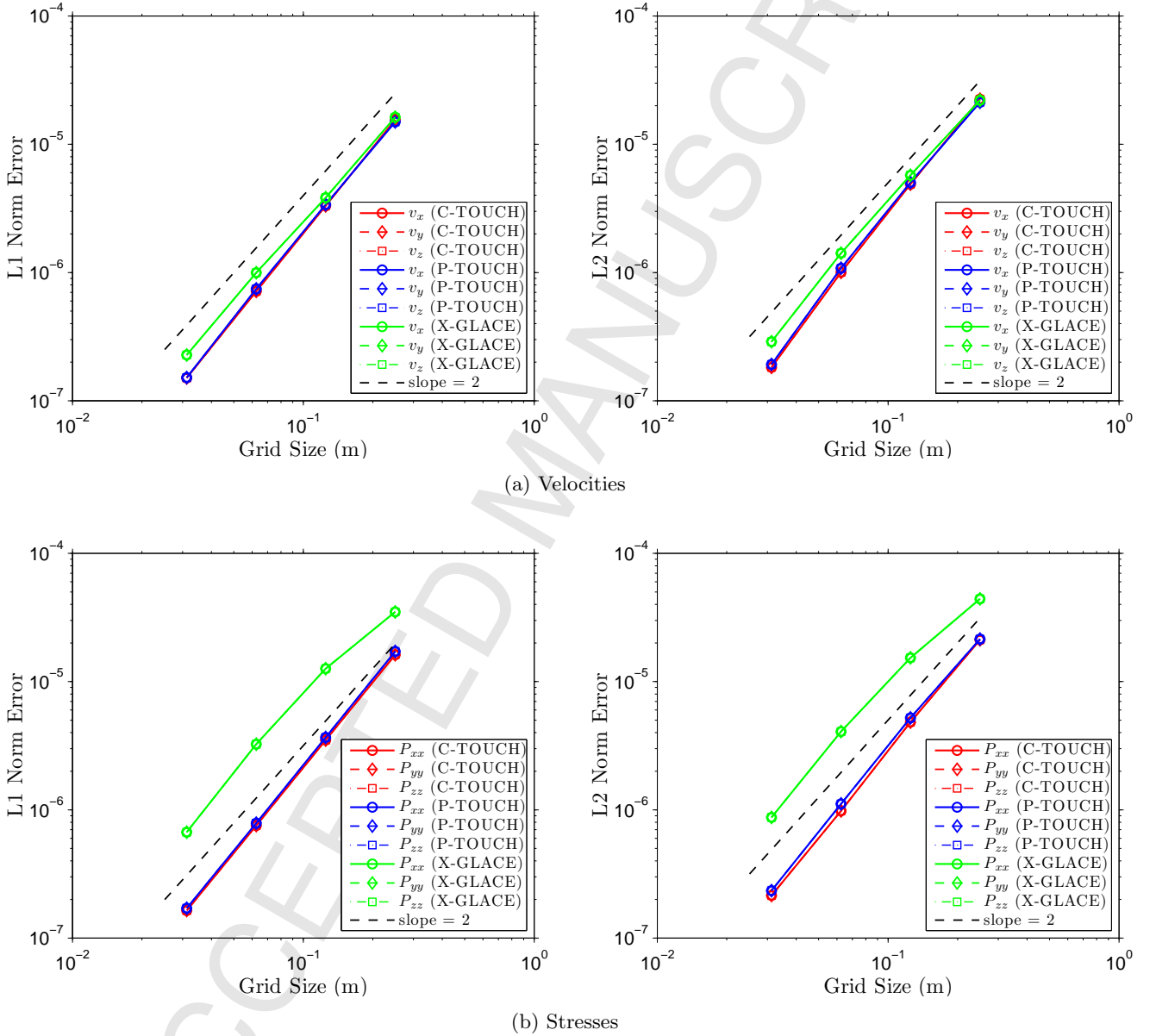
(a) Velocities

(b) Stresses

Figure 5: Low dispersion cube: L_1 and L_2 norm convergence of components of (a) velocities; and (b) stresses using the $\{\boldsymbol{p}, \boldsymbol{F}, \boldsymbol{H}, J\}$ C-TOUCH, P-TOUCH ($\xi_{\{\boldsymbol{F}, \boldsymbol{H}, J\}} = 0$) and X-GLACE schemes. Results obtained with $A = B = C = 1$ and $U_0 = 5 \times 10^{-4}$ m at time $t = 4$ ms. A linear elastic material is used with $\rho_0 = 1100$ kg/m^3, $E = 17$ MPa, $\nu = 0.3$ and $\alpha_{\text{CFL}} = 0.3$.

16

(a) Initial configuration

(b) Initial velocity (m/s) and mesh
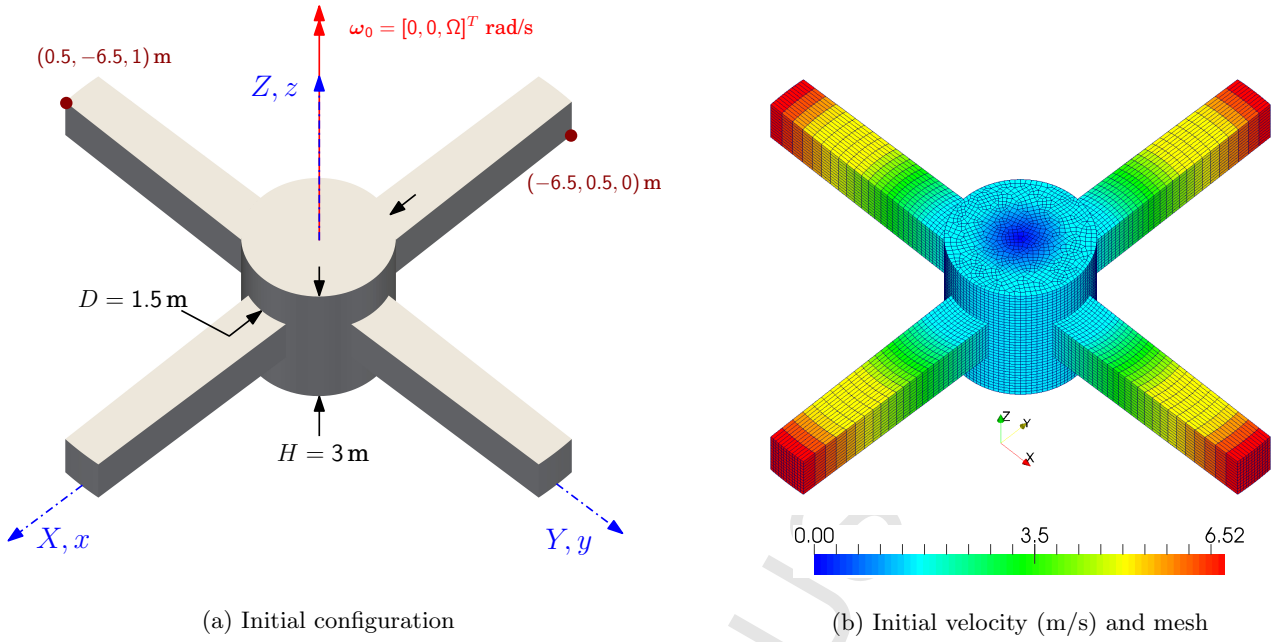
Figure 6: Satellite-like structure: Problem setup.

can be noticed (denoted as dashed lines in Figs. 9a and 10a), specially in the case of X-GLACE scheme.

8.3. Bending dominated scenario

In this example, performance of the proposed scheme is assessed in nearly incompressible bending dominated scenarios. Following [1, 52, 54, 55, 57], a 1 m squared cross section column clamped at the bottom and free on all other sides is presented (see Fig. 11a). The column is subjected to bending by the application of an initial linearly varying velocity profile given by $\boldsymbol{v}_0 = V[(Y/H), 0, 0]^T$ m/s, where V m/s is the maximum velocity applied and H m is the height of column (see Fig. 11b). A nearly incompressible neo-Hookean constitutive law is used where the material parameters are density $\rho = 1100$ kg/m^3, Young's modulus $E = 17$ MPa and Poisson's ratio $\nu = 0.45$.

In the first part of this example a thick column of height $H = 6$ m is considered. The time evolution of deformation along with pressure distribution is shown in Fig. 12. It is remarkable to observe the locking-free deformation behaviour obtained by employing only 2 elements across the thickness of the column. A mesh refinement is also carried out in Fig. 13 to show the deformation along with normal (see Fig. 13a) and shear (see 13b) components of stresses. Both cases show that better stress resolution is obtained as the mesh is refined without the appearance of any oscillations. Moreover, evolution of horizontal displacement u_x and horizontal velocity v_x at the tip of the column $\boldsymbol{X} = [0.5, 6, 0.5]^T$ m is shown in Fig. 14a. As the mesh is refined convergence can be clearly observed. Furthermore, bending of a thin column of height $H = 30$ m is also investigated. The mesh refinement of deformation of the column along with normal and shear stresses are plotted in Figs. 15 and 16, respectively. Again, the horizontal displacement u_x and horizontal velocity v_x of the tip of the column $\boldsymbol{X} = [0.5, 30, 0.5]^T$ m is monitored in Fig. 14b. As the mesh is refined, practically identical solutions are obtained showing mesh convergence.

8.4. Highly non-linear scenario

A well documented twisting column example has been explored in References [1, 47, 48, 51, 52, 55–59], which aims to examine the effectiveness of the proposed methodologies in highly nonlinear scenarios. A unit squared cross section column of height $H = 6$ m is considered (see Fig. 17a). The problem is simulated with an initial sinusoidal angular velocity field relative to the origin given by $\boldsymbol{\omega}_0 = \Omega[0, \sin(\pi Y/2H), 0]^T$ rad/s, where $\Omega = 105$ rad/s represents the magnitude of initial angular velocity (see Fig. 17b). The main objective of this problem is to assess the capability of the proposed methodologies when approaching the limit of incompressibility ($\kappa/\mu \geq 500$). To effectively handle this scenario, a preconditioned Riemann
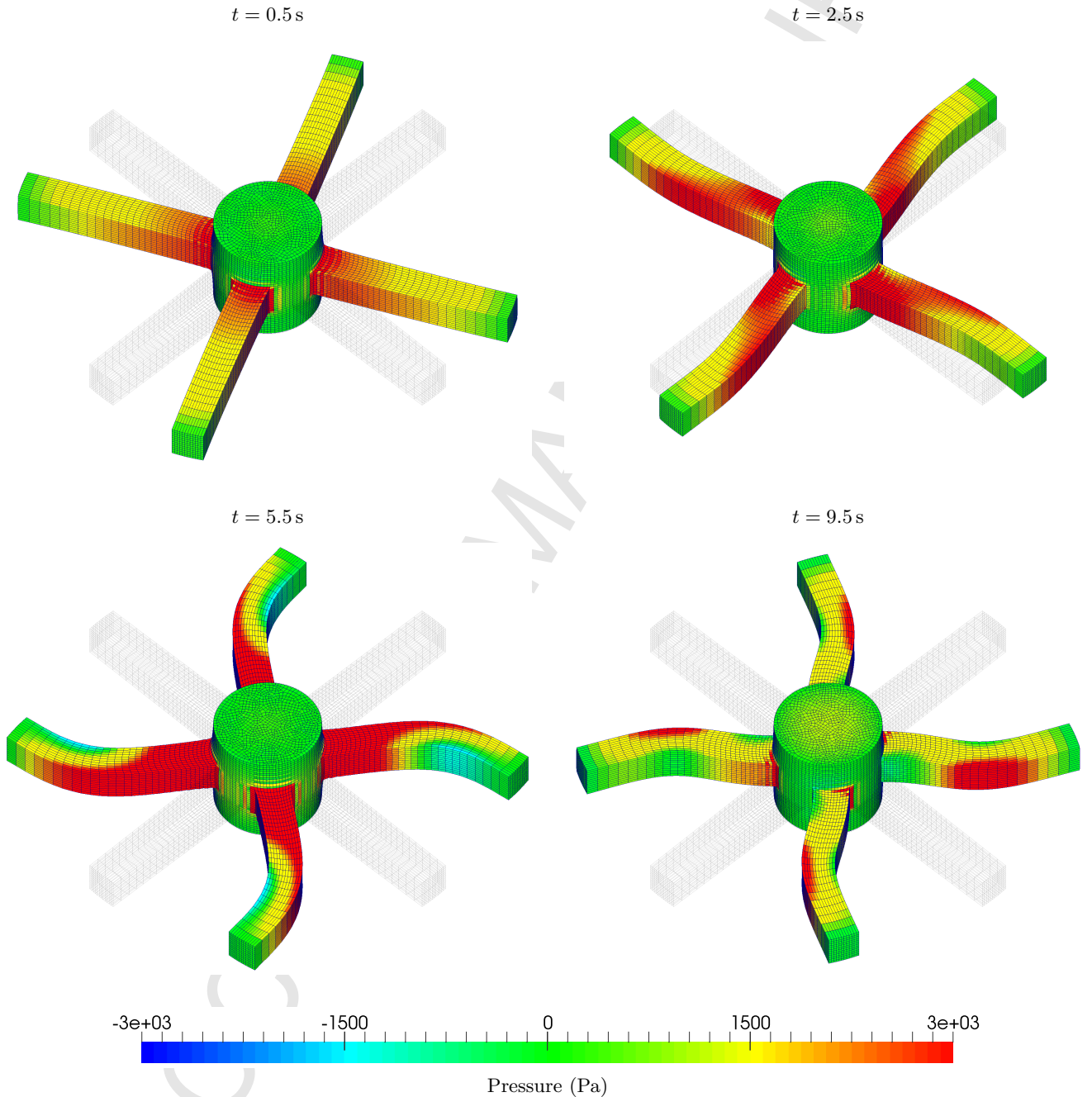
17

1
2
3
4
5
6
7
8
9
10
11
12
13
14
15
16
17
18
19
20
21
22
23
24
25
26
27
28
29
30
31
32
33
34
35
36
37
38
39
40
41
42
43
44
45
46
47
48
49
50
51
52
53
54
55
56
57
58
59
60
61
62
63
64
65

$t = 0.5\,\mathrm{s}$

$t = 2.5\,\mathrm{s}$

$t = 5.5\,\mathrm{s}$

$t = 9.5\,\mathrm{s}$

-3e+03   -1500   0   1500   3e+03

Pressure (Pa)

Figure 7: Satellite-like structure: Time evolution of the deformation along with the pressure distribution using the $\{p, F, H, J\}$ C-TOUCH scheme. Results obtained using a discretisation of 51336 hexahedral elements with an angular velocity $\omega_0 = [0, 0, 1]^T$ rad/s. A neo-Hookean material is used with $\rho_0 = 1000$ kg/m^3, $E = 50.05$ kPa, $\nu = 0.3$, $\alpha_{\mathrm{CFL}} = 0.3$ and $\Delta t \approx 1.3 \times 10^{-3}$ s.

18
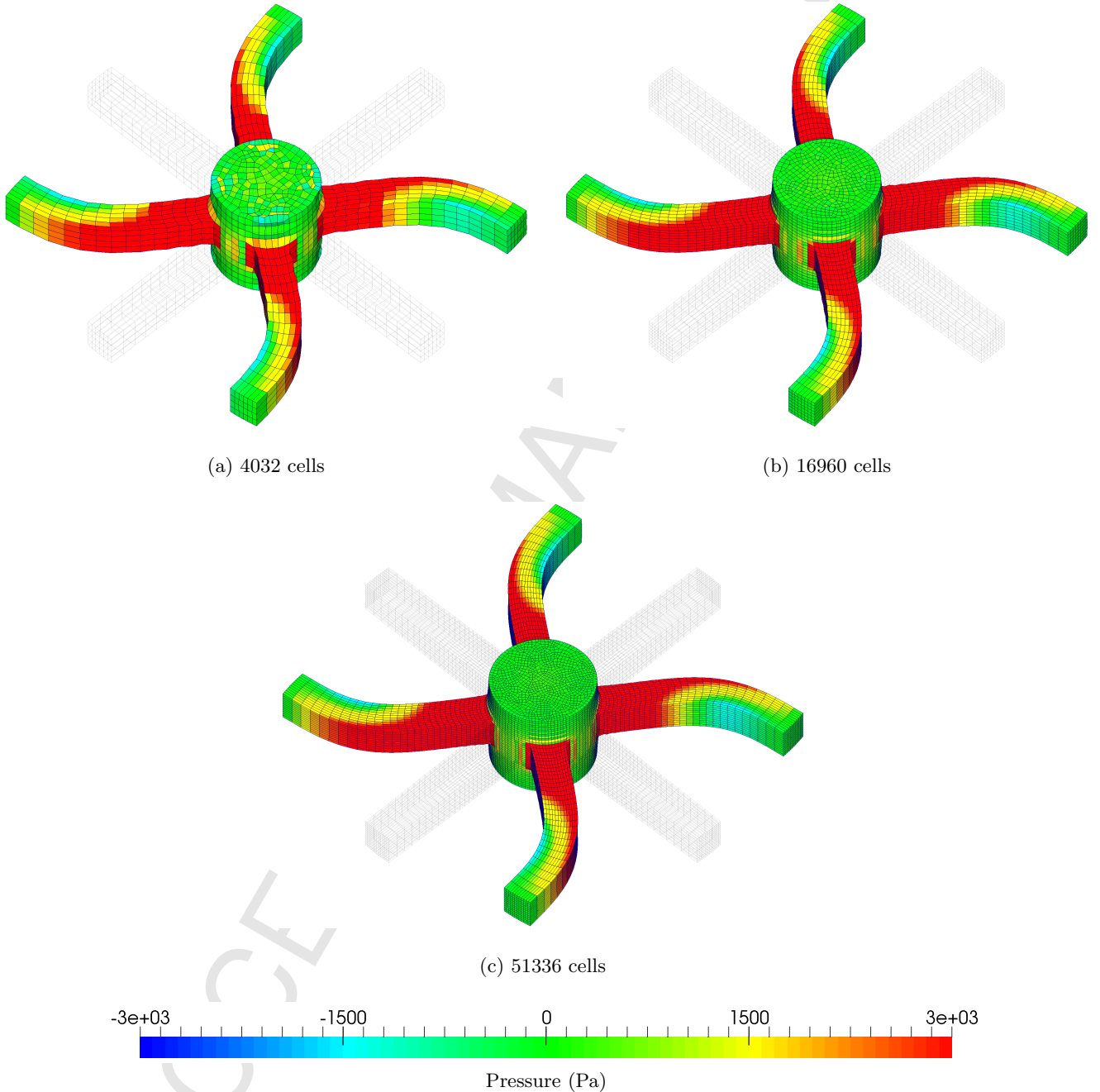
Figure 8: Satellite structure: Mesh refinement of deformed shapes along with pressure distribution at time $t = 5.5\,$s using various mesh sizes: (a) 4032; (b) 16960; and (c) 51336 hexahedral elements. Results obtained using the $\{\boldsymbol{p}, \boldsymbol{F}, \boldsymbol{H}, J\}$ C-TOUCH scheme with an angular velocity $\boldsymbol{\omega}_0 = [0, 0, 1]^T$ rad/s. A neo-Hookean material is used with $\rho_0 = 1000$ kg/m^3, $E = 50.05$ kPa, $\nu = 0.3$ and $\alpha_{\mathrm{CFL}} = 0.3$.

19

(a) Global angular momentum

(b) Global linear momentum
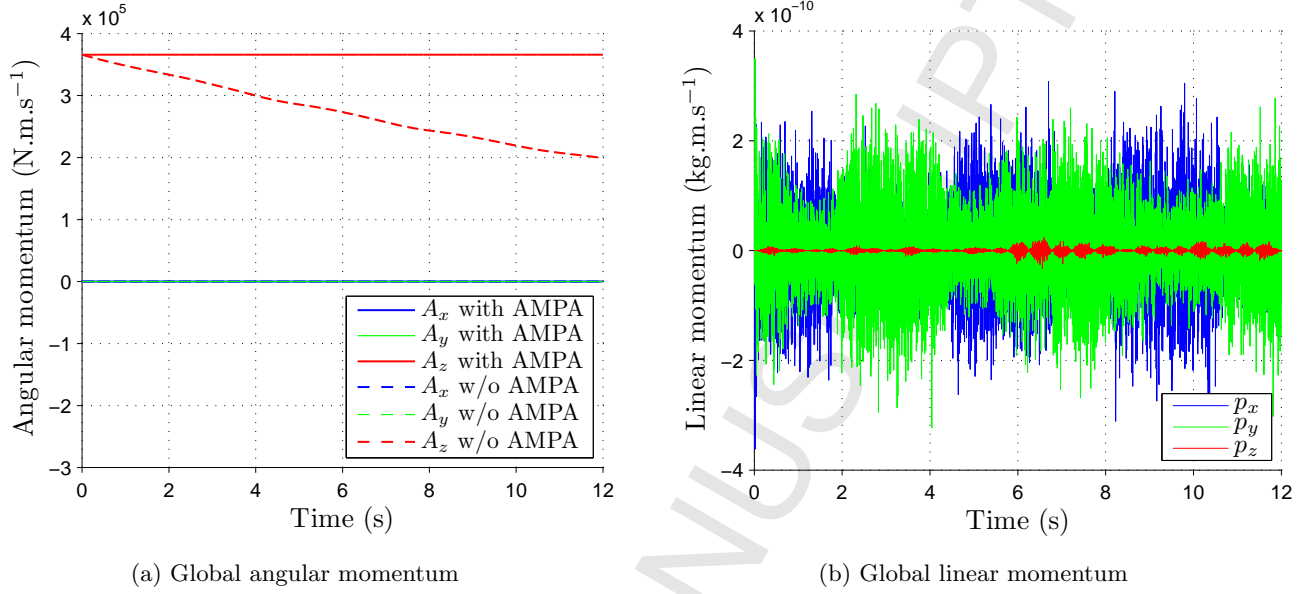
Figure 9: Satellite-like structure: Time evolution of the components of (a) global angular momentum with and without the consideration of discrete angular momentum projection algorithm (AMPA); and (b) global linear momentum using the $\{\boldsymbol{p}, \boldsymbol{F}, \boldsymbol{H}, J\}$ C-TOUCH scheme. Results obtained with an angular velocity $\boldsymbol{\omega}_0 = [0, 0, 1]^T$ rad/s with a discretisation of 51336 hexahedral elements. A neo-Hookean constitutive model is utilised with $\rho_0 = 1000$ kg/m^3, $E = 50.05$ kPa, $\nu = 0.3$ and $\alpha_{\mathrm{CFL}} = 0.3$.

(a) Global angular momentum

(b) Global linear momentum
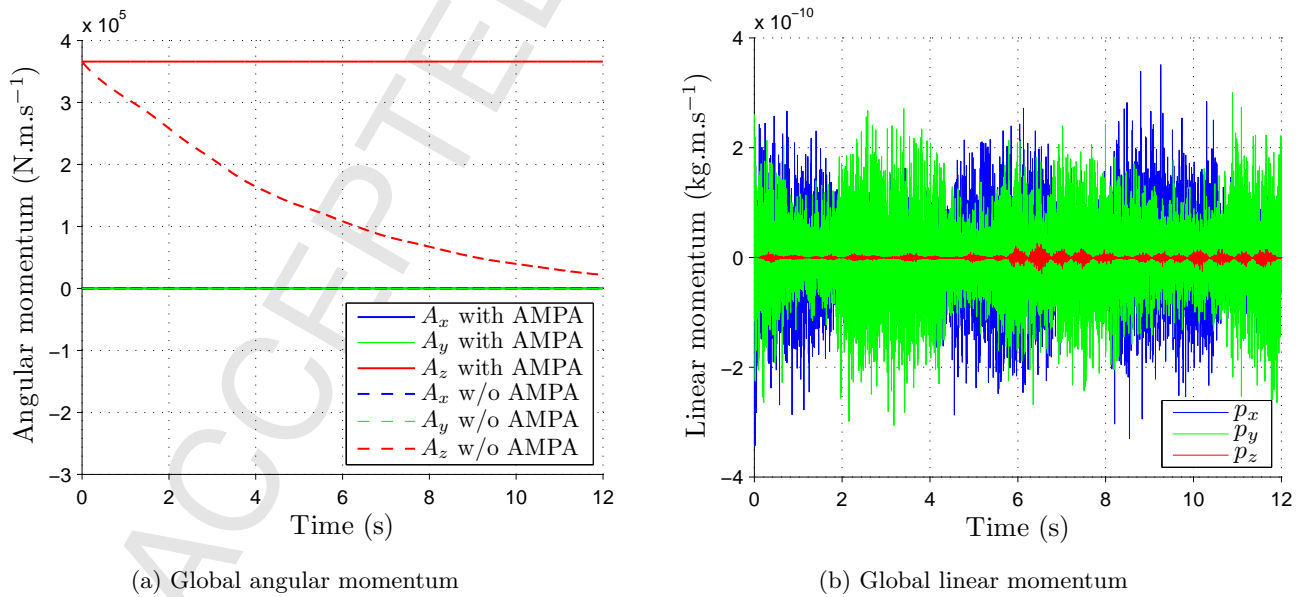
Figure 10: Satellite-like structure: Time evolution of the components of (a) global angular momentum with and without the consideration of discrete angular momentum projection algorithm (AMPA); and (b) global linear momentum using the $\{\boldsymbol{p}, \boldsymbol{F}, \boldsymbol{H}, J\}$ X-GLACE scheme. Results obtained with an angular velocity $\boldsymbol{\omega}_0 = [0, 0, 1]^T$ rad/s with a discretisation of 51336 hexahedral elements. A neo-Hookean constitutive model is utilised with $\rho_0 = 1000$ kg/m^3, $E = 50.05$ kPa, $\nu = 0.3$ and $\alpha_{\mathrm{CFL}} = 0.3$.

20

(a) Initial configuration

(b) Initial velocity for V=10 m/s and mesh
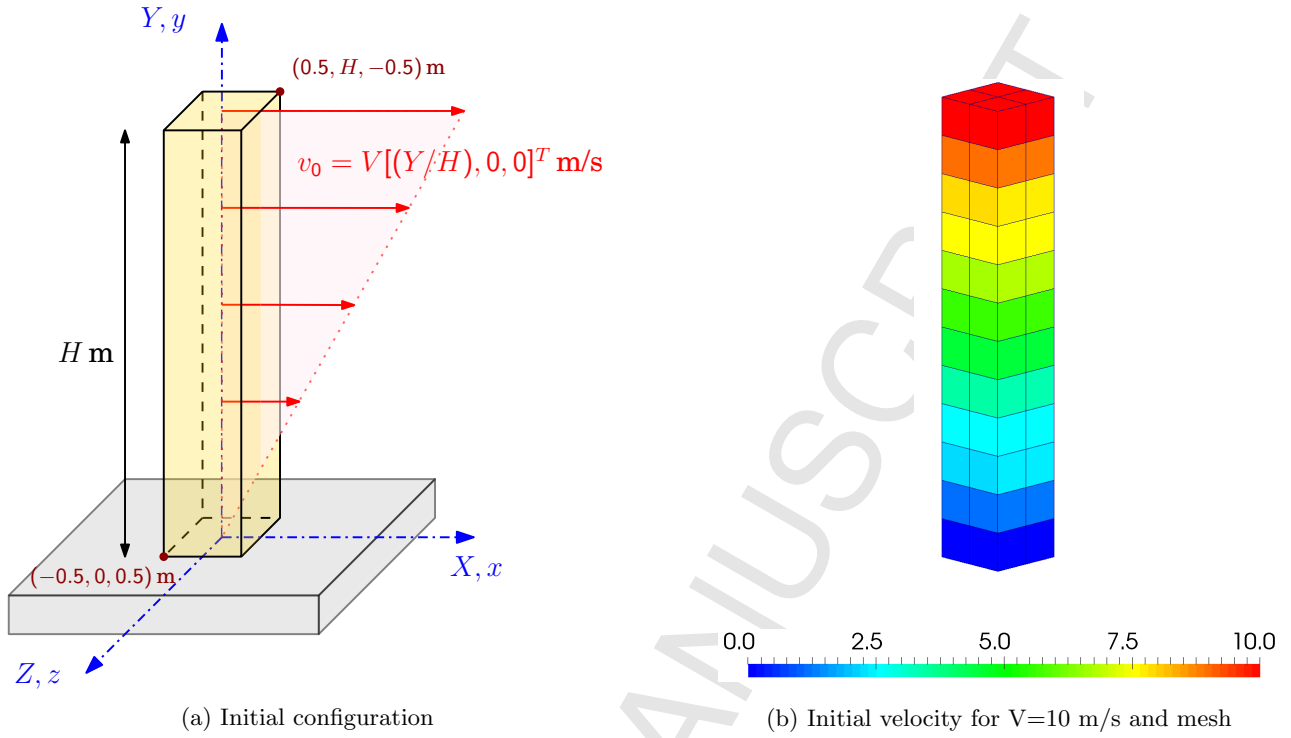
Figure 11: Thick column: Problem setup.

solver (see Section 4.2) is thus required. A neo-Hookean material is used with material density $\rho_0 = 1100$ kg/m^3, Young's modulus $E = 17$ MPa and Poisson's ratio $\nu = 0.4999$, unless otherwise stated.

In Fig. 18a,b, two different formulations, namely $\{\boldsymbol{p}, \boldsymbol{F}\}$ and $\{\boldsymbol{p}, \boldsymbol{F}, \boldsymbol{H}, J\}$, are presented. Both the deformation and pressure field obtained are practically identical. Notice that the slightly discontinuous cell pressure distribution along the longitudinal direction of the column does not correspond to any spurious pressure instability, as it gets eliminated after mesh refinement (see Fig. 18c). Alternatively, a nodal averaging (smoothing) process could have been used to display the results (refer to Fig. 18d). However, it is known that this can lead to the removal of possible pressure fluctuations. It is for this reason why we have explicitly decided not to do so in this paper, and we always depict cell values contour plots (see 18a,b)

For benchmarking purposes, Fig. 19 depicts a comparison of the proposed C-TOUCH, P-TOUCH and X-GLACE methodologies against the recently proposed JST-SPH [58] and SUPG-SPH [59] mesh-free methods. For completeness, the column is also simulated using the non-LBB compliant B-bar hexahedral method (see Fig. 19d) and the LBB compliant Q2-Q1 hexahedral FEM (see Fig. 19e). Remarkably, all the schemes described above produce very similar results both in terms of deformed shape and pressure field. Insofar as an axisymmetric hexahedral mesh is employed, the column is expected to prevent out-of-plane deformation. This can be easily shown by monitoring the displacement of a point located at the top surface of the column along the central axis. Fig. 22 shows that the evolution of planar displacement components (e.g. u_x and u_z) at point $\boldsymbol{X} = [0, 6, 0]^T$ m is within zero machine accuracy.

The problem becomes significantly more challenging by increasing the initial angular velocity to a value of $\Omega = 200$ rad/s, thus leading to a pronounced twisting behaviour. A mesh refinement study is shown in Fig. 20 at time $t = 90$ ms. In particular, the number of twists shown in the column is captured extremely well even with the use of a coarse mesh. Aiming to prove mesh convergence, Fig. 21a illustrates the time evolution of the ratio of current and initial heights of the column by using successive meshes of $4 \times 24 \times 4$, $8 \times 48 \times 8$ and $16 \times 96 \times 16$ hexahedral elements. Moreverover, the global numerical dissipation introduced in the algorithm can be assessed by taking the difference between total conserved energy and

21

t = 0.25 s

t = 0.5 s

t = 0.75 s

t = 1.0 s

t = 1.25 s

t = 1.5 s

-1e+06   -7e+5   -3.5e+5   0   3.5e+5   7e+5   1e+06
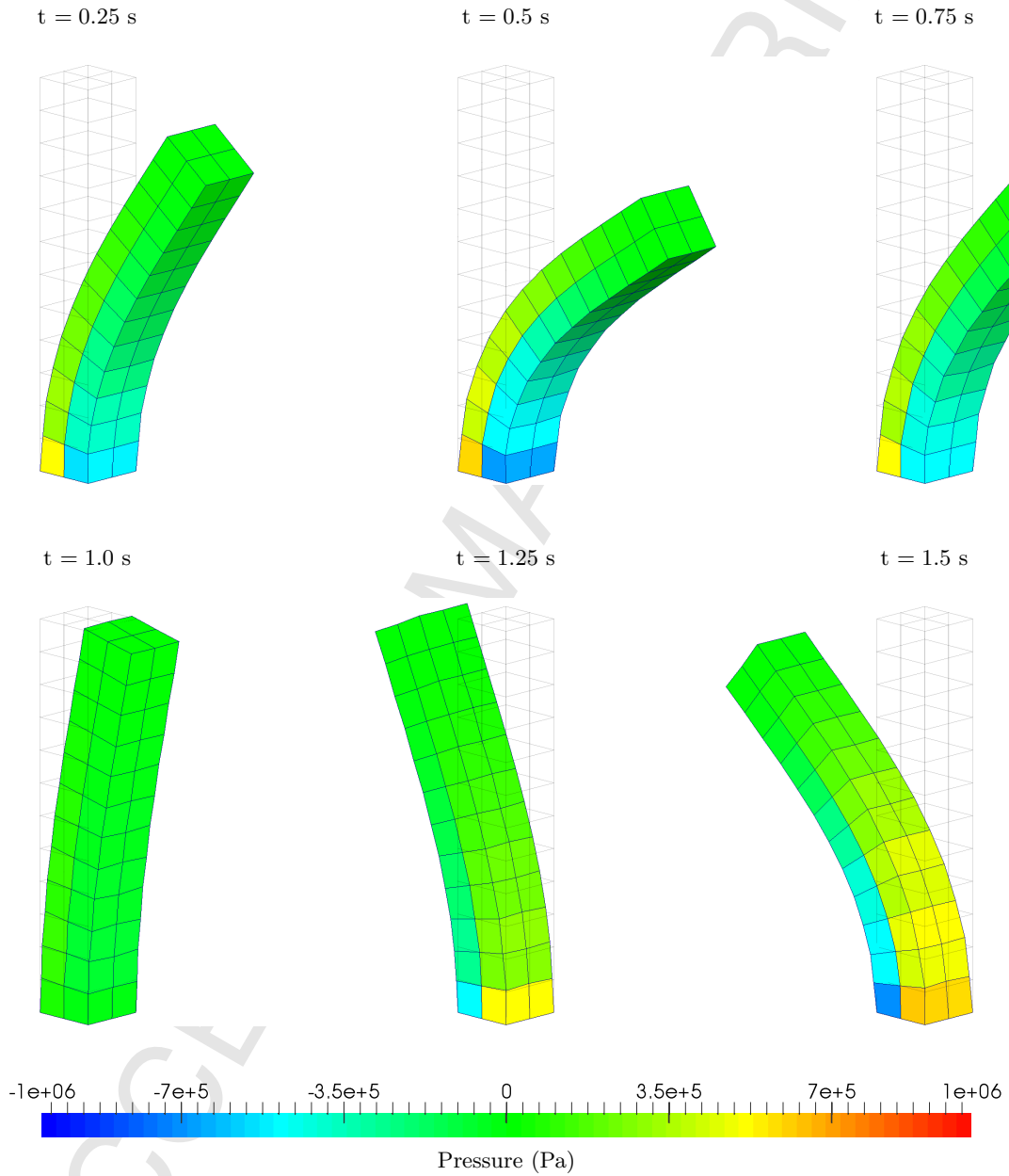
Pressure (Pa)

Figure 12: Thick column: Time evolution of deformation along with pressure distribution using $\{p, F, H, J\}$ C-TOUCH scheme. Results obtained with velocity $\boldsymbol{v}_0 = V[(Y/H), 0, 0]^T$ m/s where $V = 10$ m/s and $H = 6$ m using a discretisation of $2 \times 12 \times 2$ hexahedral elements. A neo-Hookean material is used with $\rho = 1100$ kg/m^3, $E = 17$ MPa, $\nu = 0.45$ and $\alpha_{\mathrm{CFL}} = 0.3$.

22

2×12×2 cells   4×24×4 cells   8×48×8 cells   16×96×16 cells

-2e+06   -1.4e+6   -7e+5   0   7e+5   1.4e+6   2e+06

(a) Normal stress P_{yY} (Pa)

-1e+06   -7e+5   -3.5e+5   0   3.5e+5   7e+5   1e+06

(b) Shear stress P_{xY} (Pa)
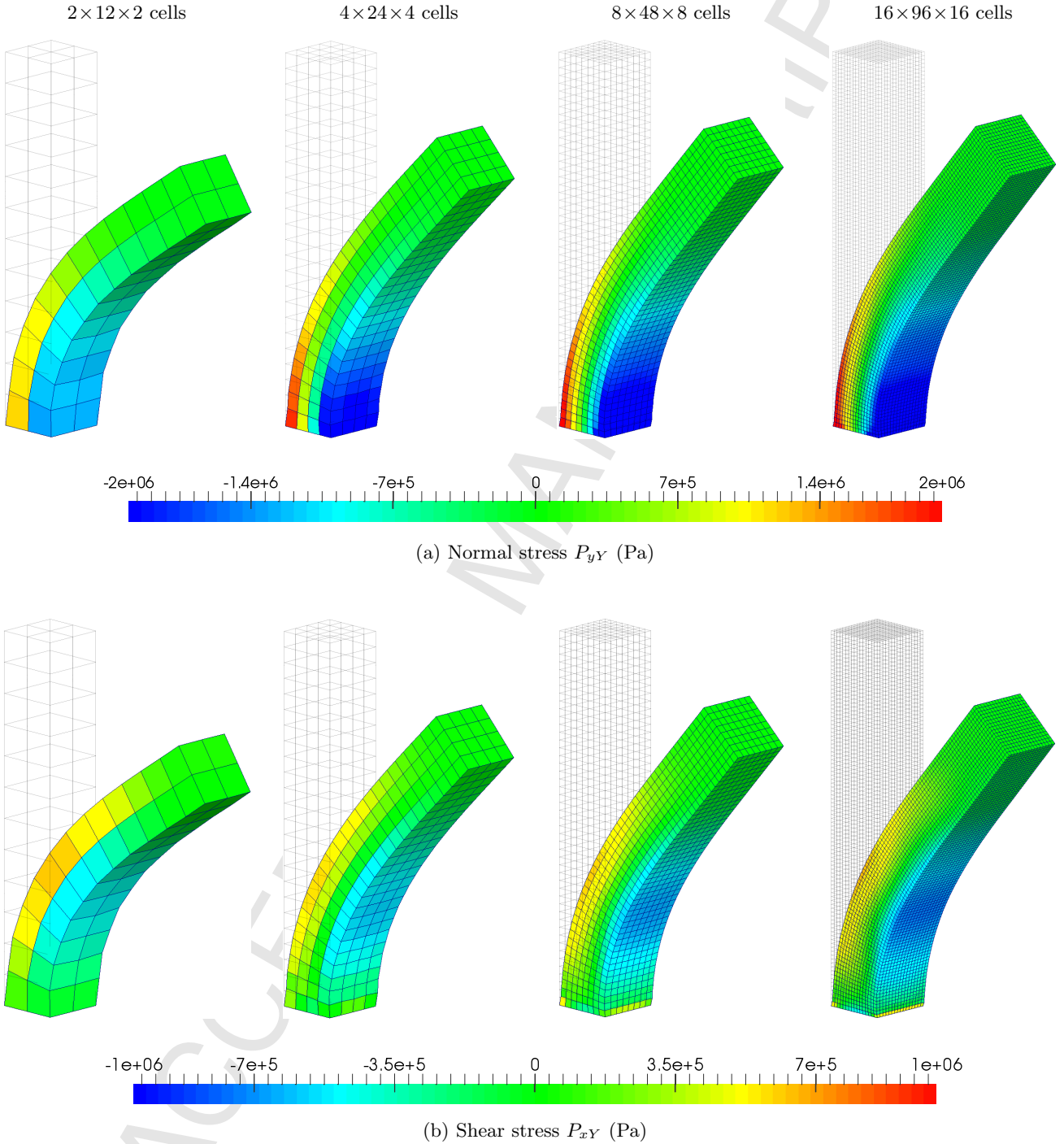
Figure 13: Thick column: Mesh refinement of deformation plotted with (a) normal stress P_{yY}; and (b) shear stress P_{xY} using $\{p, F, H, J\}$ C-TOUCH scheme at time $t = 0.5$ s. Results obtained with velocity $\boldsymbol{v}_0 = V[(Y/H), 0, 0]^T$ m/s where $V = 10$ m/s and $H = 6$ m using a discretisation of $2 \times 12 \times 2$, $4 \times 24 \times 4$, $8 \times 48 \times 8$ and $16 \times 96 \times 16$ hexahedral elements. A neo-Hookean material is used with $\rho = 1100$ kg/m³, $E = 17$ MPa, $\nu = 0.45$ and $\alpha_{\mathrm{CFL}} = 0.3$.

23
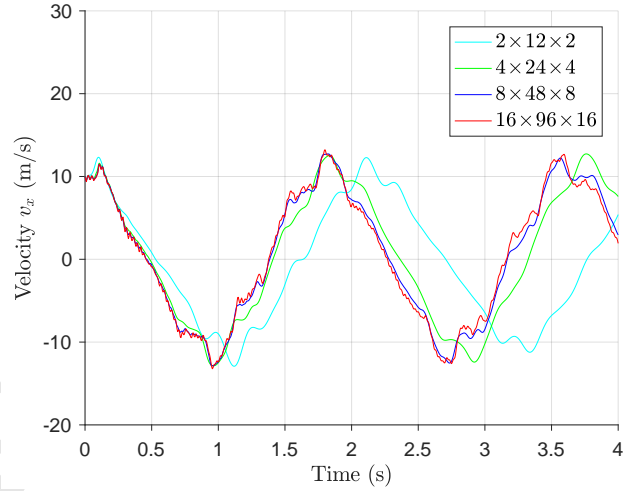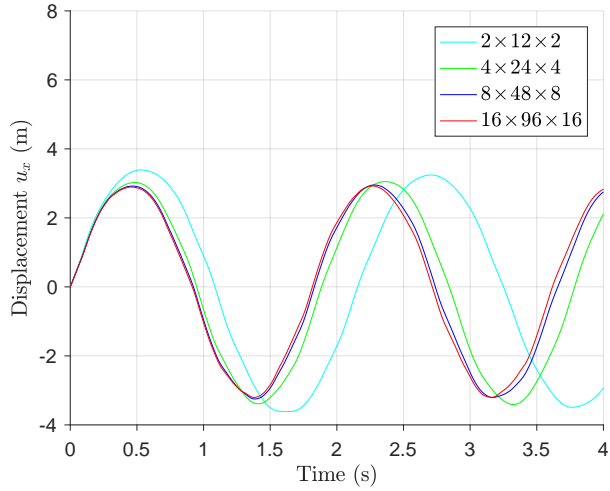
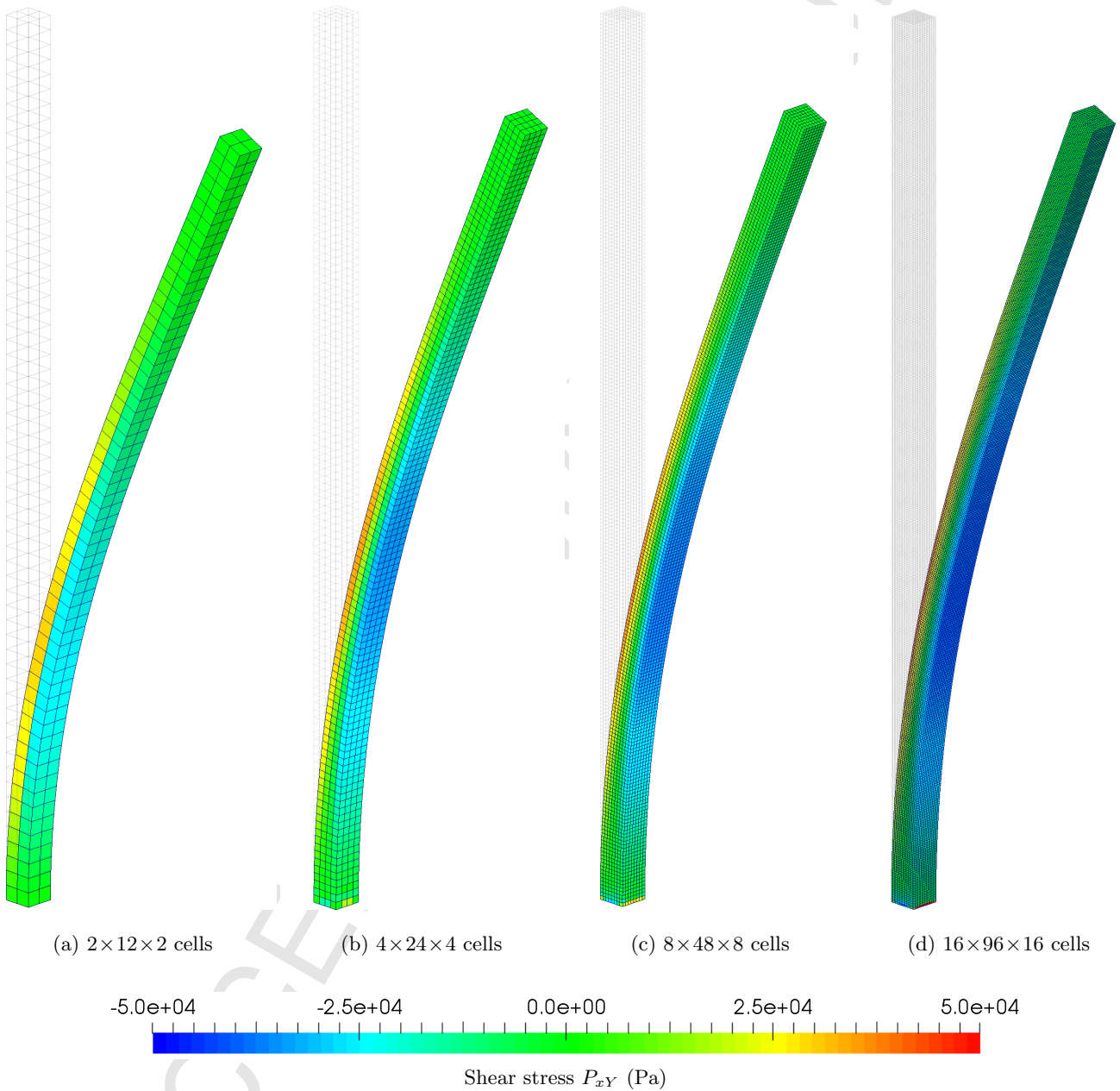(a) Thick column: Horizontal displacement and velocity
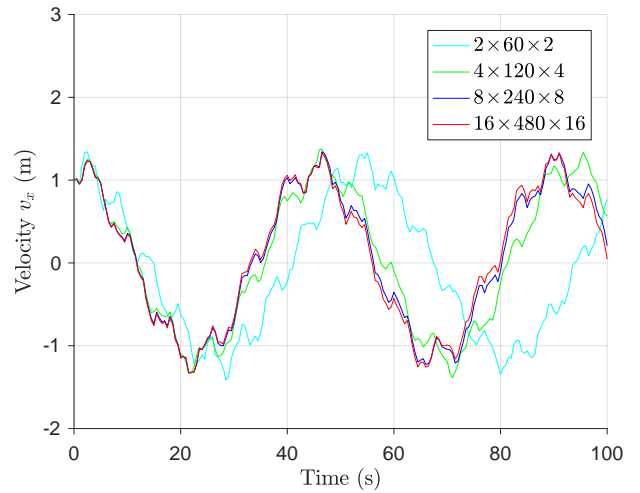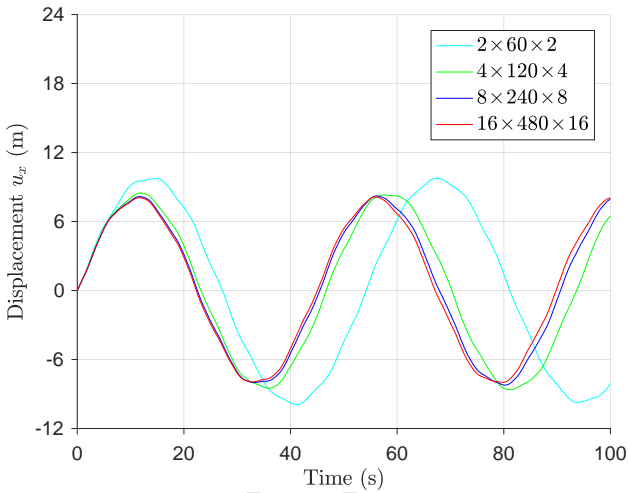
(b) Thin column: Horizontal displacement and velocity

Figure 14: Thick and thin columns: Time evolution of (a) horizontal displacement u_x (thick column); (b) horizontal velocity v_x (thick column); (c) horizontal velocity u_x (thin column); and (d) horizontal velocity v_x (thin column) at material point $\boldsymbol{X} = [0.5, H, 0.5]^T$ m where $H = 6$ m and $H = 30$ m for thick and thin columns respectively. Results obtained using $\{\boldsymbol{p}, \boldsymbol{F}, \boldsymbol{H}, J\}$ C-TOUCH scheme with velocity $\boldsymbol{v}_0 = V[(Y/H), 0, 0]^T$ m/s where $V = 10$ m/s for thick column and $V = 1$ m/s for thin column. A neo-Hookean constitutive model is utilised with $\rho_0 = 1100$ kg/m^3, $E = 17$ MPa, $\nu = 0.45$ and $\alpha_{\mathrm{CFL}} = 0.3$.

24

1
2
3
4
5
6
7
8
9
10
11
12
13
14
15
16
17
18
19
20
21
22
23
24
25
26
27
28
29
30
31
32
33
34
35
36
37
38
39
40
41
42
43
44
45
46
47
48
49
50
51
52
53
54
55
56
57
58
59
60
61
62
63
64
65

(a) $2{\times}12{\times}2$ cells   (b) $4{\times}24{\times}4$ cells   (c) $8{\times}48{\times}8$ cells   (d) $16{\times}96{\times}16$ cells

-2.0e+05   -1.0e+05   0.0e+00   1.0e+05   2.0e+05

Normal stress P_{yY} (Pa)
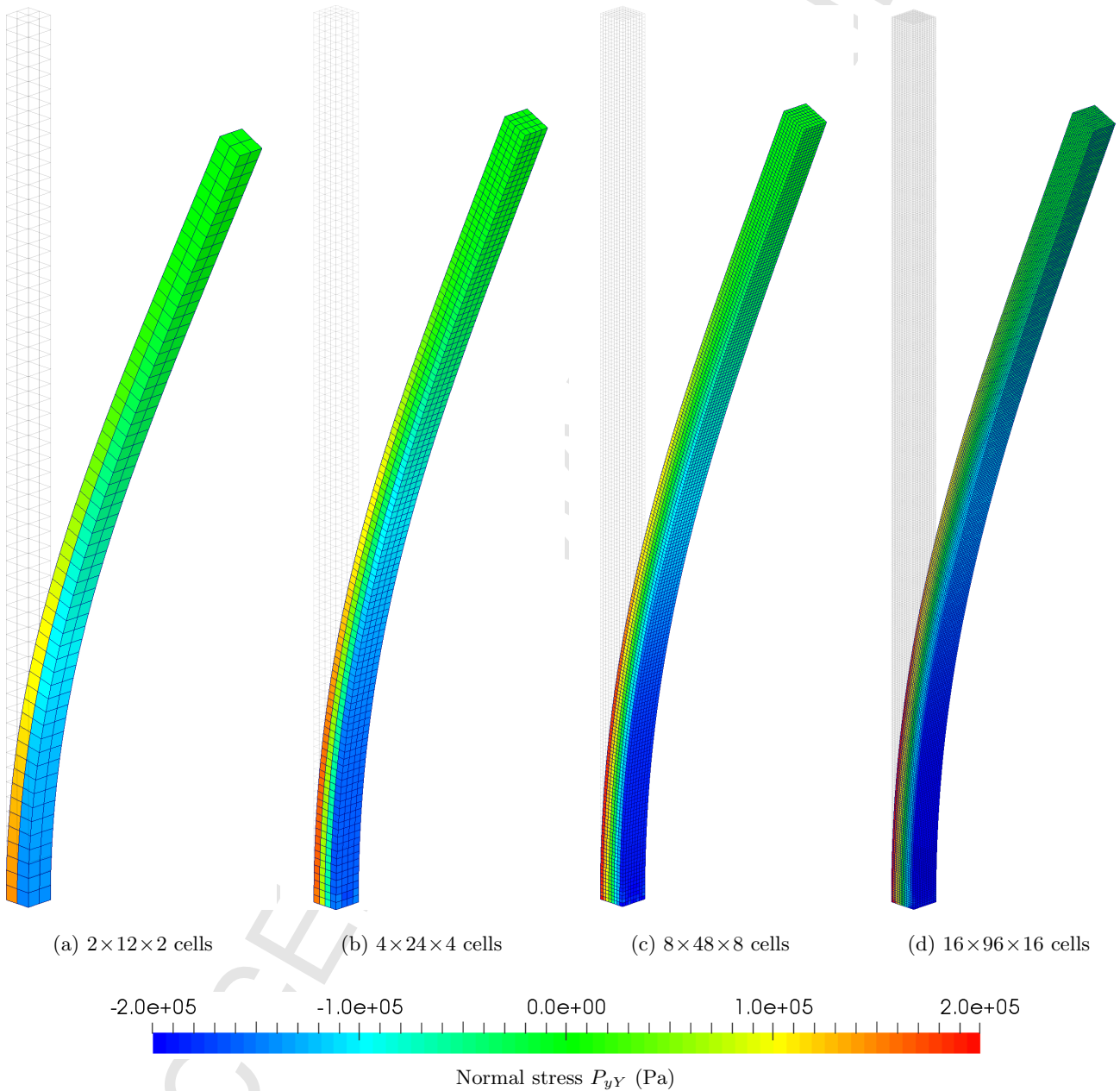
Figure 15: Thin column: Mesh refinement of deformation plotted with normal stress P_{yY} using (a) $2{\times}12{\times}2$; (b) $4{\times}24{\times}4$; (c) $8{\times}48{\times}8$; and (d) $16{\times}96{\times}16$ hexahedral elements. Results obtained at time $t = 12\,\mathrm{s}$ using $\{\boldsymbol{p}, \boldsymbol{F}, \boldsymbol{H}, J\}$ C-TOUCH scheme with velocity $\boldsymbol{v}_0 = V[(Y/H), 0, 0]^T$ m/s where $V = 1\,\mathrm{m/s}$ and $H = 30\,\mathrm{m}$. A neo-Hookean material is used with $\rho = 1100$ kg/m^3, $E = 17$ MPa, $\nu = 0.45$ and $\alpha_{\mathrm{CFL}} = 0.3$.

25

(a) $2 \times 12 \times 2$ cells   (b) $4 \times 24 \times 4$ cells   (c) $8 \times 48 \times 8$ cells   (d) $16 \times 96 \times 16$ cells

Shear stress P_{xY} (Pa)

Figure 16: Thin column: Mesh refinement of deformation plotted with shear stress P_{xY} distribution using (a) $2 \times 12 \times 2$; (b) $4 \times 24 \times 4$; (c) $8 \times 48 \times 8$; and (d) $16 \times 96 \times 16$ hexahedral elements. Results obtained at time $t = 12\,\mathrm{s}$ using $\{\boldsymbol{p}, \boldsymbol{F}, \boldsymbol{H}, J\}$ C-TOUCH scheme with velocity $\boldsymbol{v}_0 = V\,[(Y/H), 0, 0]^T$ m/s where $V = 1\,\mathrm{m/s}$ and $H = 30\,\mathrm{m}$. A neo-Hookean material is used with $\rho = 1100\ \mathrm{kg/m^3}$, $E = 17$ MPa, $\nu = 0.45$ and $\alpha_{\mathrm{CFL}} = 0.3$.

26

the summation of internal and kinetic energies. This is shown in Fig. 21b where the numerical dissipation of the algorithm is reduced when increasing the mesh density.

8.5. Contact capability

Previously explored in [82] in two dimensions, an extension of this contact example to three dimensions is carried out by considering the rebound of a hollow circular bar of outer diameter $D_0 = 6.4$ mm, inner diameter $D_i = 2$ mm and height $H = 32.4$ mm (see Fig. 23). The bar impacts against a rigid frictionless wall with an initial velocity of $\boldsymbol{v}_0 = [0, -100, 0]^T$ m/s where the separation distance between the bar and wall is 4 mm. Upon impact, the bar undergoes large compressive deformation until $t = 150$ μs when all the kinetic energy of the bar is converted to internal strain energy. Soon afterwards, tensile forces start developing and a bounce-off motion begins. At approximately $t = 250$ μs the bar completely detaches from the wall and continues to deform. A neo-Hookean constitutive model is chosen with density $\rho_0 = 8930$ kg/m^3, Young's modulus $E = 585$ MPa and Poisson's ratio $\nu = 0.45$. Due to the existence of two symmetry planes, only a quarter of the domain is modelled with appropriate symmetric roller support and free boundary conditions.

A sequence of snapshots displaying the deformation of the hollow bar along with its pressure distribution is shown in Fig. 24. No spurious pressure instabilities can be observed. In Fig. 25, a mesh convergence study is carried out with a progressive level of refinement. It is remarkable that the deformation obtained with the coarse mesh agrees extremely well with the fine mesh, although the pressure contour is clearly enhanced as we increase the mesh density. In Fig. 26 and Fig. 27, two sequentially refined hexahedral meshes of 512 and 13824 are used. Fig. 26 shows the time evolution of the global linear and angular momenta, whereas Fig. 27 shows the time history of vertical displacement u_y at the bottom plane $\boldsymbol{X}_B = \left[1/\sqrt{2}, 0, 1/\sqrt{2}\right]^T$ mm (shown as red lines) and at the top plane $\boldsymbol{X}_T = \left[1/\sqrt{2}, 32.4, 1/\sqrt{2}\right]^T$ mm

(a) Initial configuration

(b) Initial velocity (m/s) for $\Omega = 105$ rad/s and mesh
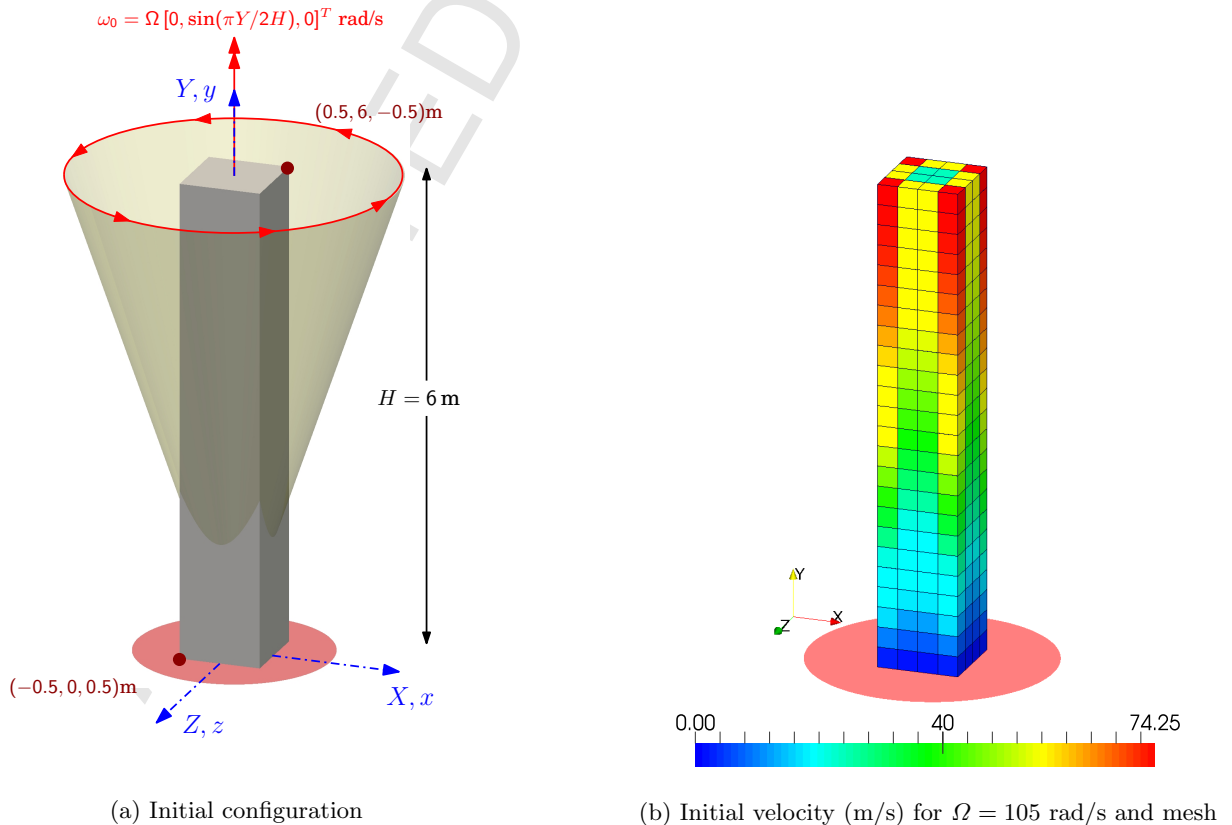
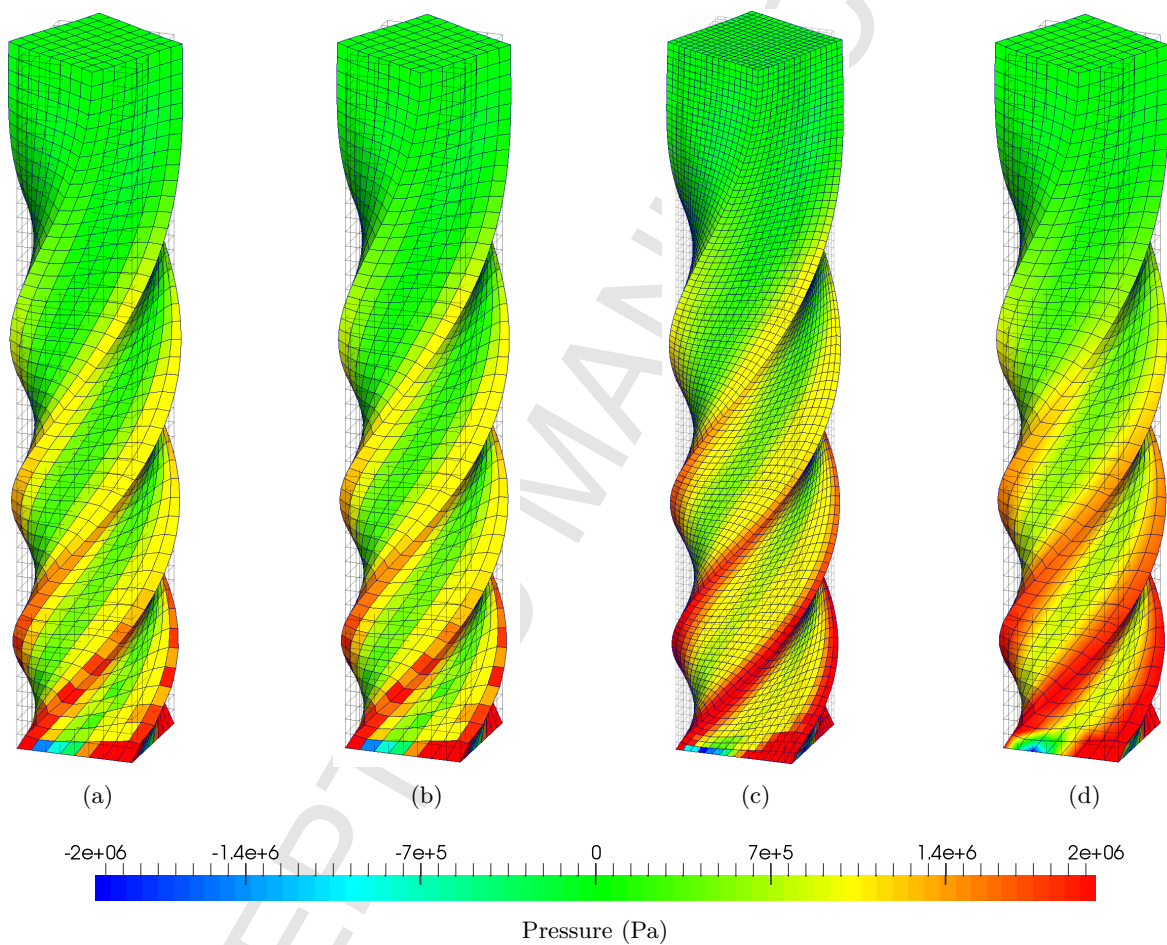Figure 17: Twisting column: Problem setup.

Figure 18: Twisting column: Comparison of deformed shapes along with the pressure distribution using (a) $\{\boldsymbol{p}, \boldsymbol{F}\}$ ($8 \times 48 \times 8$, cell based pressure); (b) $\{\boldsymbol{p}, \boldsymbol{F}, \boldsymbol{H}, J\}$ ($8 \times 48 \times 8$, cell based pressure); (c) $\{\boldsymbol{p}, \boldsymbol{F}, \boldsymbol{H}, J\}$ ($16 \times 96 \times 16$, cell based pressure) with fine mesh; and (d) $\{\boldsymbol{p}, \boldsymbol{F}, \boldsymbol{H}, J\}$ ($8 \times 48 \times 8$, node based pressure) using C-TOUCH scheme. Results obtained at time $t = 0.1$ s with an angular velocity $\boldsymbol{\omega}_0 = \Omega \left[0, \sin(\pi Y/2H), 0\right]^T$ where $\Omega = 105$ rad/s and $H = 6$ m. A neo-Hookean constitutive model is used with density $\rho_0 = 1100$ kg/m^3, $E = 17$ MPa, $\nu = 0.4999$, $\alpha_{\mathrm{CFL}} = 0.3$ and $\Delta t \approx 1.3 \times 10^{-5}$ s.
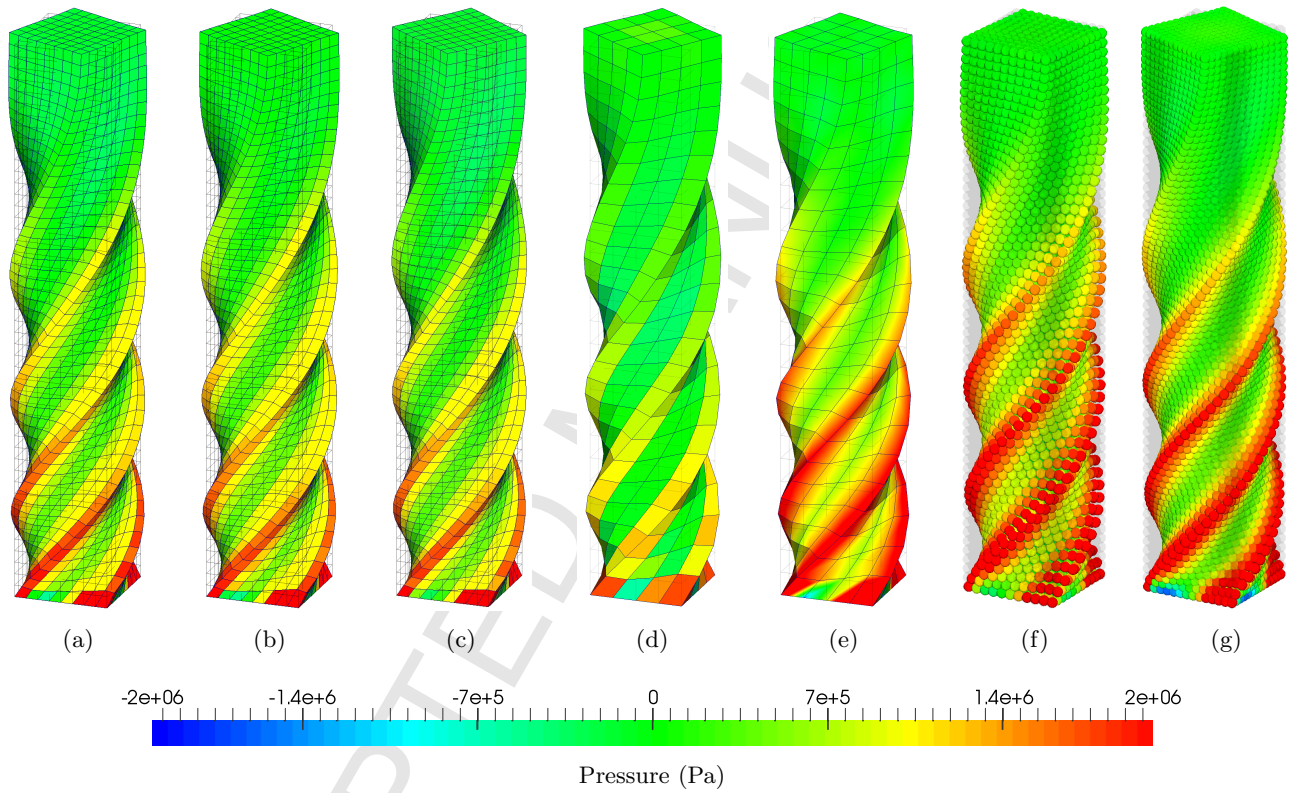
Figure 19: Twisting column: Comparison of deformed shapes along with the pressure distribution using various numerical schemes namely; (a) $\{p, F, H, J\}$ C-TOUCH ($\tilde{\kappa} = 3\kappa$); (b) $\{p, F, H, J\}$ P-TOUCH ($\xi_F = \xi_H$=0.1); (c) $\{p, F, H, J\}$ X-GLACE ($\tilde{\kappa} = 3\kappa$); (d) B-bar hexahedral method; (e) Q2-Q1 hexahedral FEM [81]; (f) JST-SPH [58]; and (g) SUPG-SPH [59] numerical schemes. Results obtained at time $t = 0.1$ s with an angular velocity $\boldsymbol{\omega}_0 = \Omega\left[0, \sin(\pi Y/2H), 0\right]^T$ where $\Omega = 105$ rad/s and $H = 6$ m. A neo-Hookean constitutive model is used with density $\rho_0 = 1100$ kg/m^3, $E = 17$ MPa, $\nu = 0.495$ and $\alpha_{\mathrm{CFL}} = 0.3$.

29

Isometric view

Top view

(a) $h = 1/4$ m   (b) $h = 1/8$ m   (c) $h = 1/16$ m   (d) $h = 1/32$ m
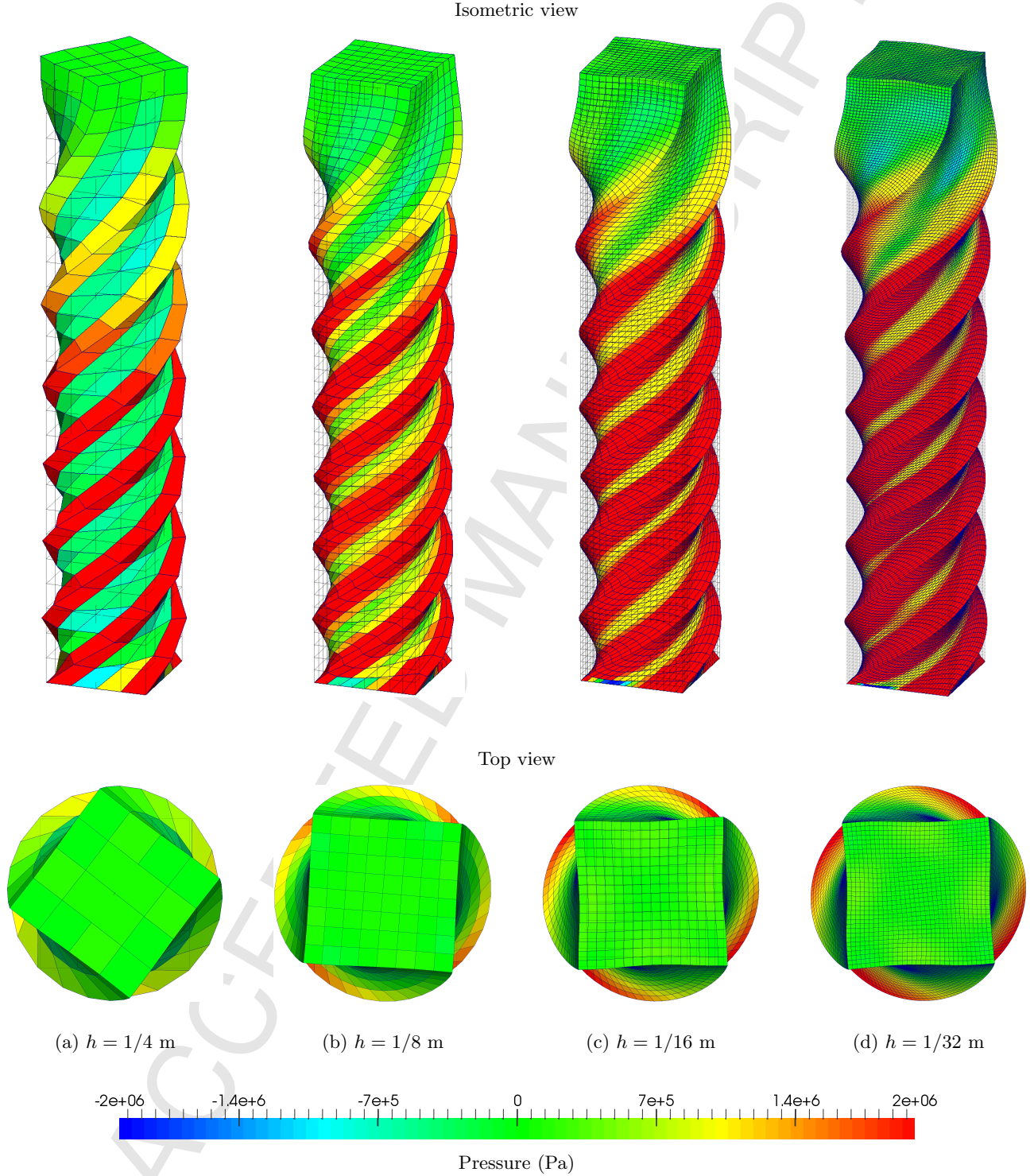
Pressure (Pa)

Figure 20: Twisting column: Mesh refinement of deformed shapes with pressure distribution obtained using an increased angular velocity $\boldsymbol{\omega}_0 = \Omega\,[0, \sin(\pi Y/2H), 0]^T$, where $\Omega = 200$ rad/s and $H = 6$ m. Results obtained at $t = 90$ ms using the $\{\boldsymbol{p}, \boldsymbol{F}\}$ C-TOUCH scheme with $\tilde{\kappa} = 3\kappa$ using meshes with (a) $4 \times 24 \times 4$; (b) $8 \times 48 \times 8$; (c) $16 \times 96 \times 16$; and (d) $32 \times 192 \times 32$ hexahedral elements. A neo-Hookean material is used with $\rho_0 = 1100$ kg/m^3, $E = 17$ MPa, $\nu = 0.499$ and $\alpha_{\mathrm{CFL}} = 0.3$.

30

(a) Column height

(b) Numerical dissipation
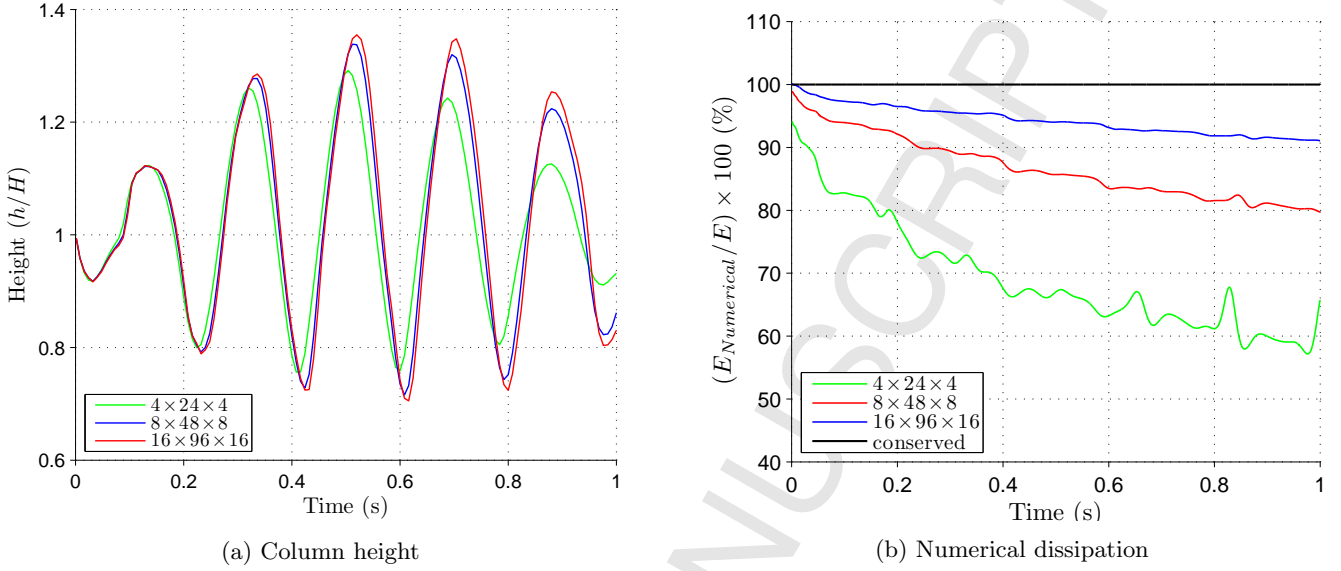
Figure 21: Twisting column: Time evolution of (a) non-dimensionalised height of the column measured at the material point $\boldsymbol{X} = [0, 6, 0]^T$ m; and (b) numerical dissipation using the $\{\boldsymbol{p}, \boldsymbol{F}\}$ C-TOUCH scheme with $\tilde{\kappa} = 3\kappa$. Results obtained using a discretisation of $4 \times 24 \times 4$, $8 \times 48 \times 8$ and $16 \times 96 \times 16$ hexahedral elements with an increased angular velocity $\boldsymbol{\omega}_0 = \Omega\,[0, \sin(\pi Y/2H), 0]^T$, where $\Omega = 200$ rad/s and $H = 6$ m. A neo-Hookean material is used with $\rho_0 = 1100$ kg/m^3, $E = 17$ MPa, $\nu = 0.499$ and $\alpha_{\mathrm{CFL}} = 0.3$.
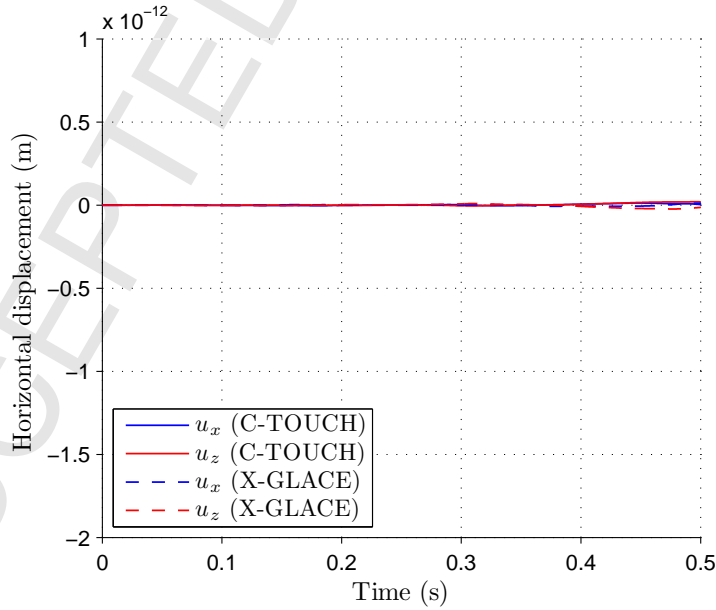
Figure 22: Twisting column: Comparison of time evolution of horizontal displacements $\boldsymbol{u}_x$ and $\boldsymbol{u}_z$ of the point at top of column along the central Y axis $\boldsymbol{X} = [0, 6, 0]^T$ m using the $\{\boldsymbol{p}, \boldsymbol{F}, \boldsymbol{H}, J\}$ C-TOUCH and X-GLACE schemes with $\tilde{\kappa} = 3\kappa$. Results obtained using a discretisation of $8 \times 48 \times 8$ hexahedral elements with an angular velocity $\boldsymbol{\omega}_0 = \Omega\,[0, \sin(\pi Y/2H), 0]^T$, where $\Omega = 105$ rad/s and $H = 6$ m. A neo-Hookean material is used with $\rho_0 = 1100$ kg/m^3, $E = 17$ MPa, $\nu = 0.495$ and $\alpha_{\mathrm{CFL}} = 0.3$.

31

1
2
3
4
5
6
7
8
9
10
11
12
13
14
15
16
17
18
19
20
21
22
23
24
25
26
27
28
29
30
31
32
33
34
35
36
37
38
39
40
41
42
43
44
45
46
47
48
49
50
51
52
53
54
55
56
57
58
59
60
61
62
63
64
65

(a) Initial configuration

(b) Initial velocity (m/s) and mesh
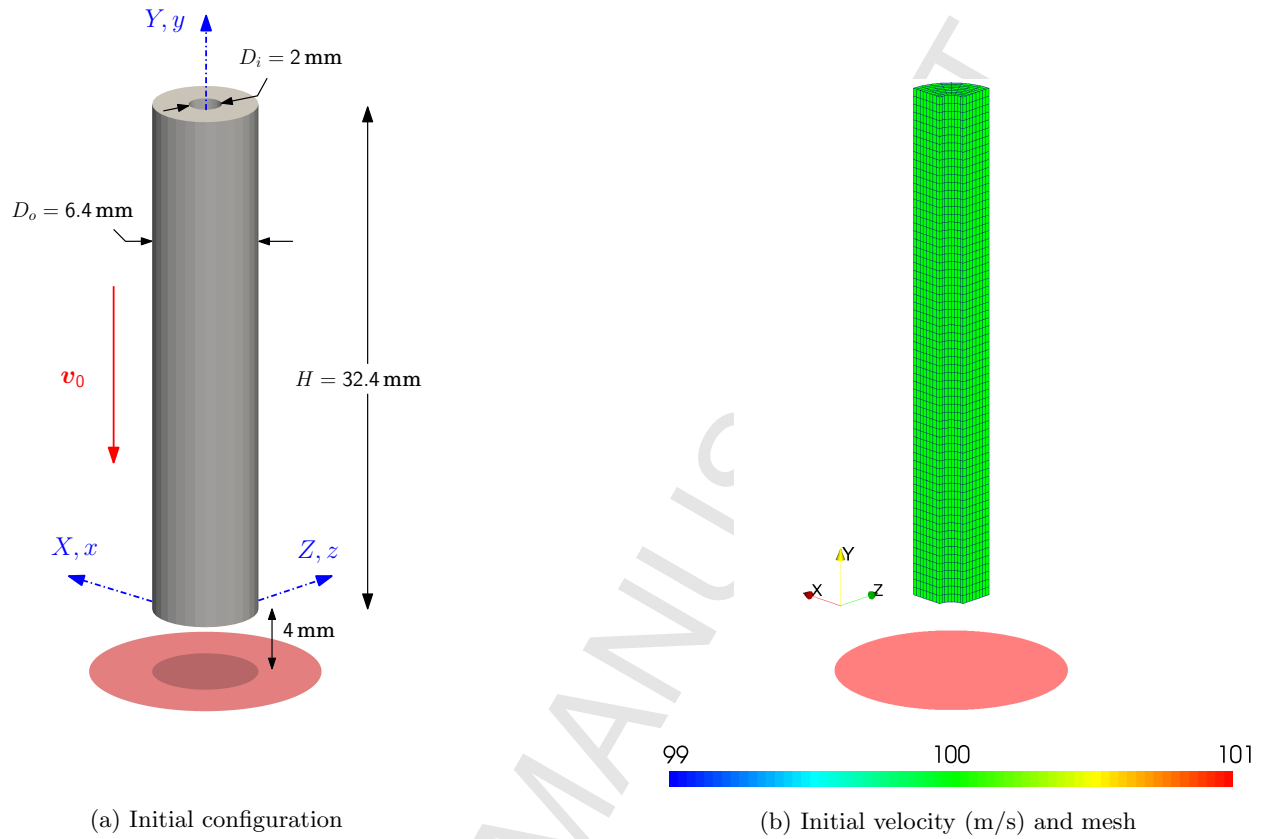
Figure 23: Bar rebound: Problem setup.

(shown as blue lines). The difference between the red and blue lines indicates the amount of elongation/reduction in bar length. Reasonably accurate deformation is obtained using a coarse mesh, showing optimal convergence for the proposed method. Finally, we further examine this problem using a large value of the Poisson's ratio $\nu = 0.499$. Fig. 28 shows a series of deformed states without experiencing any locking difficulties.
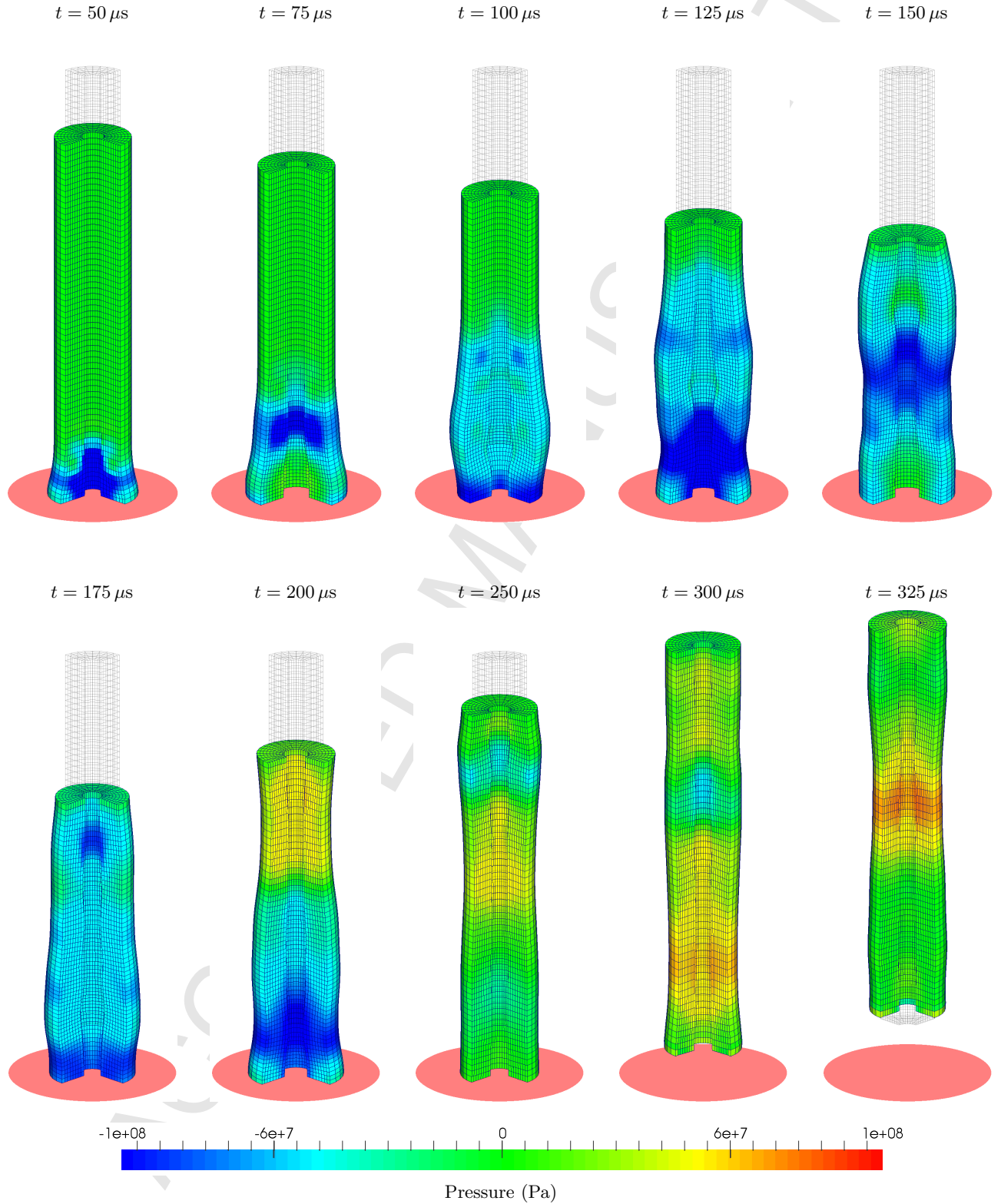
Figure 24: Bar rebound: Time evolution of the deformation along with the pressure distribution using the $\{\boldsymbol{p}, \boldsymbol{F}, \boldsymbol{H}, J\}$ C-TOUCH scheme. Results obtained with velocity $\boldsymbol{v}_0 = [0, -100, 0]^T$ m/s using 4096 hexahedral elements in quarter domain. A neo-Hookean constitutive model is used with $\rho_0 = 8930$ kg/m^3, $E = 585$ MPa, $\nu = 0.45$, $\alpha_{\mathrm{CFL}} = 0.3$ and $\Delta t \approx 7 \times 10^{-8}$ s.

512 cells   4096 cells   13824 cells

(a) $t = 150\,\mu\text{s}$

512 cells   4096 cells   13824 cells

(b) $t = 195\,\mu\text{s}$

-1e+08   -6e+7   0   6e+7   1e+08
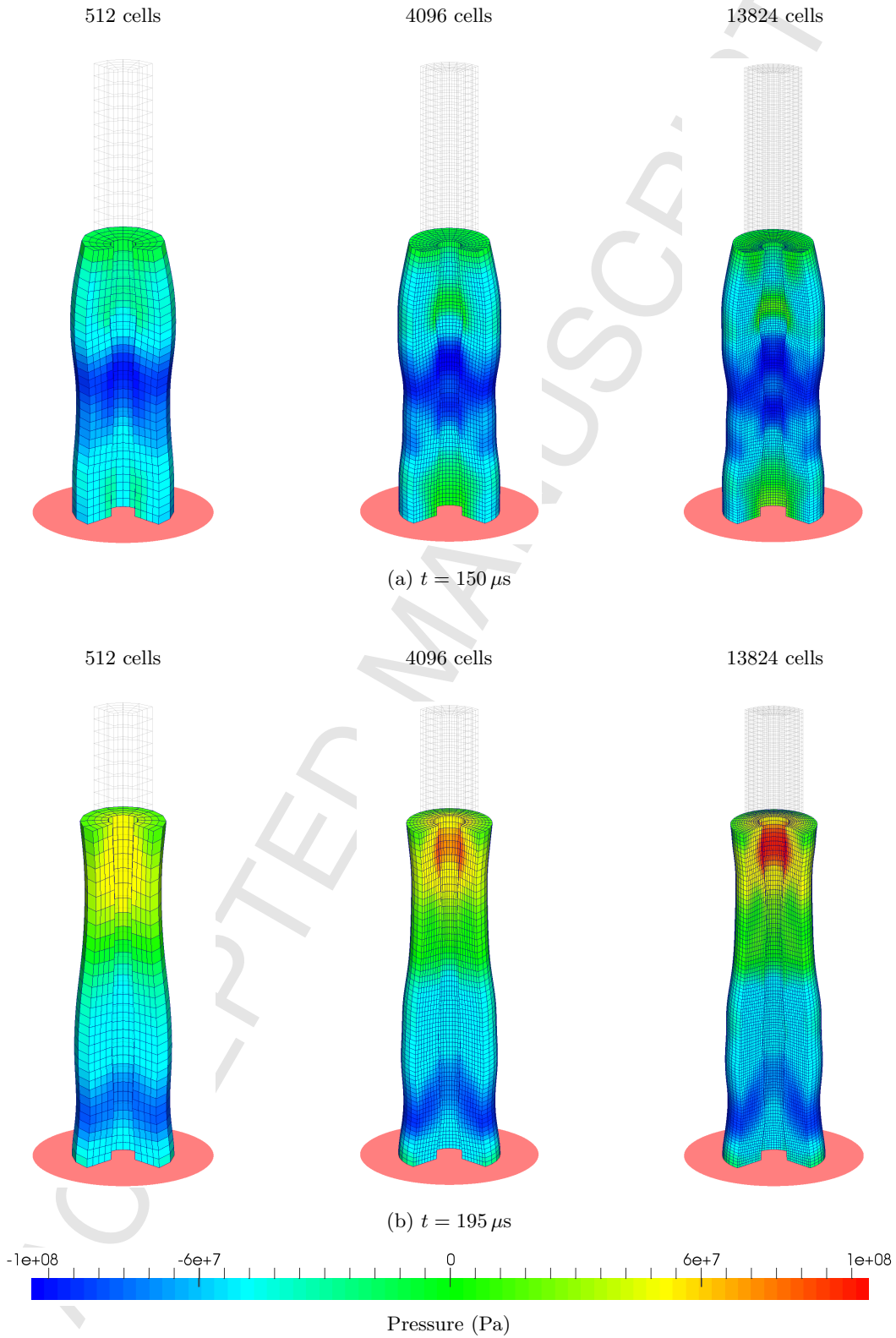
Pressure (Pa)

Figure 25: Bar rebound: Mesh refinement of deformed shapes along with pressure distribution at times: (a) $t = 150\,\mu\text{s}$; and (b) $t = 195\,\mu\text{s}$ using meshes of 512, 4096 and 13824 hexahedral elements in quarter domain. Results obtained using the $\{\boldsymbol{p}, \boldsymbol{F}, \boldsymbol{H}, J\}$ C-TOUCH scheme with velocity $\boldsymbol{v}_0 = [0, -100, 0]^T$ m/s. A neo-Hookean material is used with $\rho_0 = 8930$ kg/m^3, $E = 585$ MPa, $\nu = 0.45$ and $\alpha_{\text{CFL}} = 0.3$.

34

(a) Angular momentum
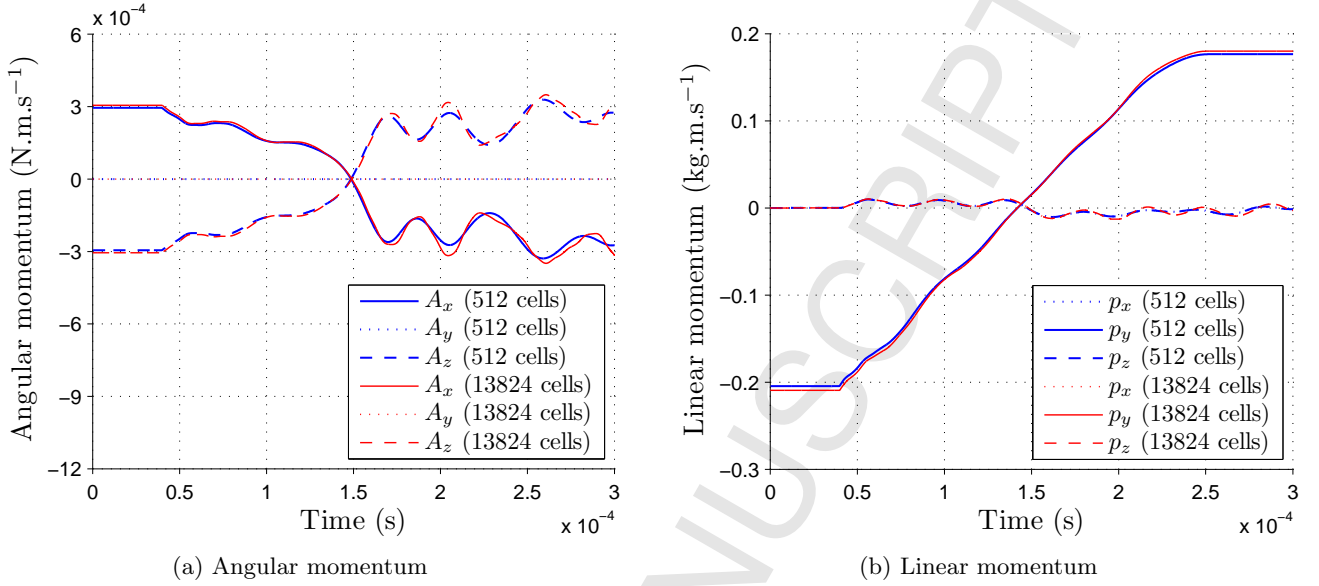
(b) Linear momentum

Figure 26: Bar rebound: Time evolution of components of (a) global angular momentum; and (b) global linear momentum using meshes of 512 and 13824 hexahedral elements in quarter domain. Results obtained using the $\{\boldsymbol{p}, \boldsymbol{F}, \boldsymbol{H}, J\}$ C-TOUCH scheme with velocity $\boldsymbol{v}_0 = [0, -100, 0]^T$ m/s. A neo-Hookean constitutive model is used with $\rho_0 = 8930$ kg/m^3, $E = 585$ MPa, $\nu = 0.45$ and $\alpha_{\mathrm{CFL}} = 0.3$.
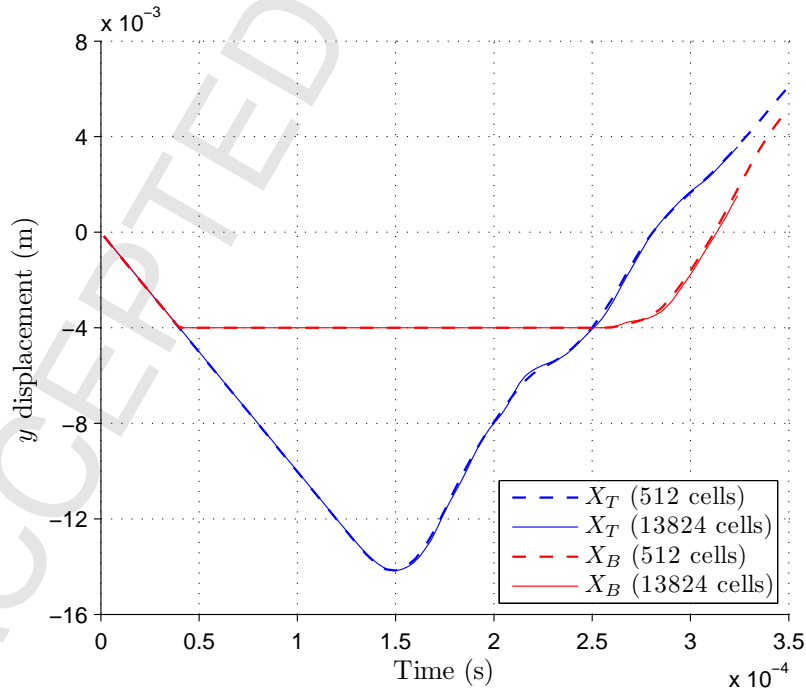
Figure 27: Bar rebound: Time evolution of vertical displacements u_y of the points on the top plane $\boldsymbol{X}_T = \left[1/\sqrt{2}, 32.4, 1/\sqrt{2}\right]^T$ mm and the bottom plane $\boldsymbol{X}_B = \left[1/\sqrt{2}, 0, 1/\sqrt{2}\right]^T$ mm. Results obtained with velocity $\boldsymbol{v}_0 = [0, -100, 0]^T$ m/s using the $\{\boldsymbol{p}, \boldsymbol{F}, \boldsymbol{H}, J\}$ C-TOUCH scheme. A neo-Hookean constitutive model is used with $\rho_0 = 8930$ kg/m^3, $E = 585$ MPa, $\nu = 0.45$ and $\alpha_{\mathrm{CFL}} = 0.3$.

35
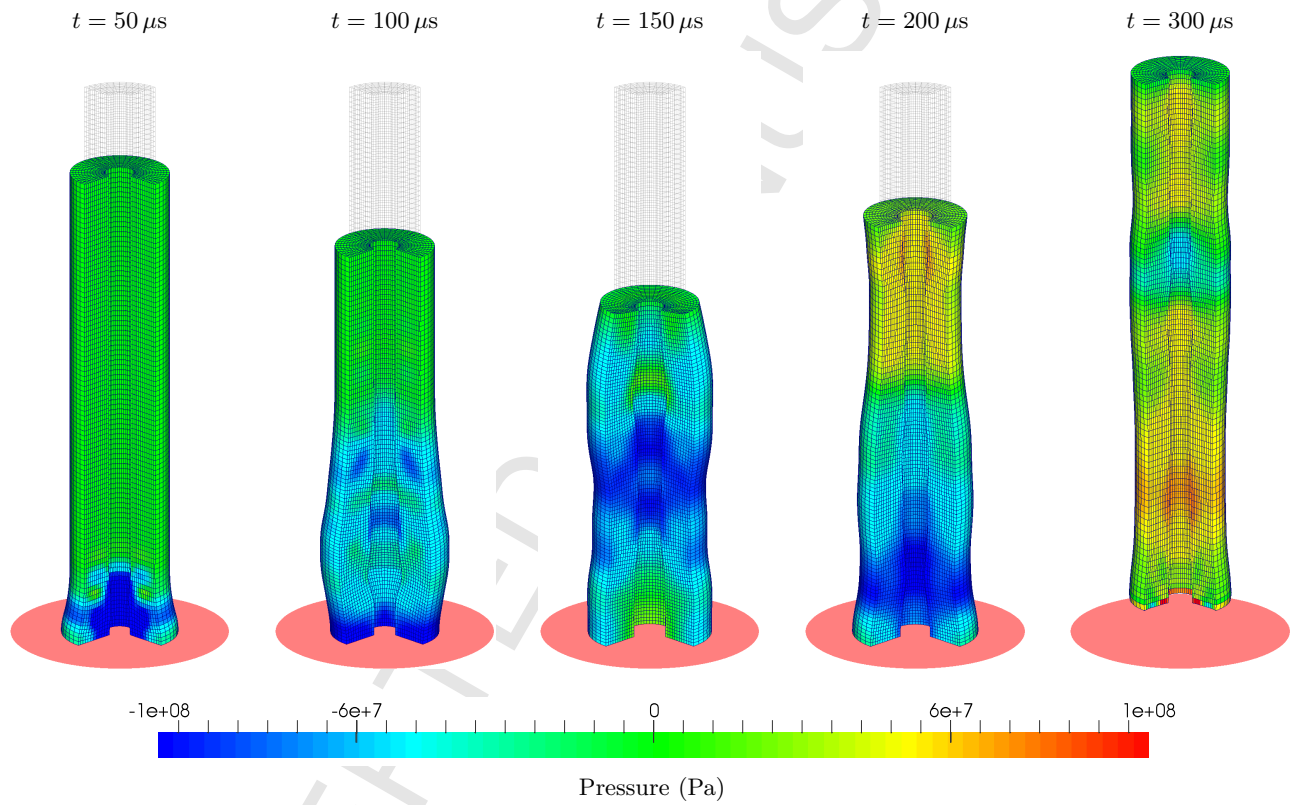
Figure 28: Bar rebound: Time evolution of the deformation along with the pressure distribution using the $\{\boldsymbol{p}, \boldsymbol{F}, \boldsymbol{H}, J\}$ C-TOUCH scheme ($\tilde{\kappa} = 3\kappa$). Results obtained with velocity $\boldsymbol{v}_0 = [0, -100, 0]^T$ m/s using 4096 hexahedral elements. A neo-Hookean constitutive model is used with $\rho_0 = 8930$ kg/m^3, $E = 585$ MPa, $\nu = 0.499$, $\alpha_{\mathrm{CFL}} = 0.3$ and $\Delta t \approx 5 \times 10^{-8}$ s.

36

8.6. Algorithm robustness

In order to assess the robustness of the algorithm, two challenging examples are presented in this section. A block, of 1×1 m^2 unit squared cross section with a height of $H = 0.5$ m, with nine equally spaced holes of diameter 0.2 m is considered (see Fig. 29a). The block is punched with a (compressive) linear velocity profile of $\boldsymbol{v}_0 = -V[0, 0, (Z/H)]$ m/s in quarter of the domain ($X \geq 0, Y \geq 0$) (see Fig. 29b). A neo-Hookean constitutive model is used where the material properties are density $\rho = 1100$ kg/m^3, Young's Modulus $E = 17$ MPa and Poisson's ratio $\nu = 0.499$.

Fig. 30 shows the time evolution of the deformation pattern with its pressure plot. The proposed method can clearly capture the extreme deformation of holes near the bottom plane ($Z = 0$), as shown in Fig. 31. No spurious pressure instabilities are observed despite simulating a complex geometry which is made of a nearly incompressible material. A mesh refinement study has also been carried out in Fig. 32. In this figure, right half of the domain has been partially clipped to show the interior pressure distribution inside the domain whilst the wireframe mesh displays the deformed configuration. Remarkably, it is clear that despite increasing the number of elements from 32400 to 86400, both the deformation and pressure resolution obtained are practically identical. More importantly, Fig. 33 highlights the importance of the dimensionless parameter $\beta := \frac{\tilde{\kappa}}{\kappa}$ used in the preconditioned Riemann solver. When using the value of $\tilde{\kappa} = \kappa$ (which recovers the elastic wave speeds $\{c_p, c_s\}$ presented in (29)), spurious pressure mode is accummulated over time which would eventually lead to breakdown of the numerical scheme. This shortcoming can be eliminated when resorting to preconditioning with the value of $\tilde{\kappa} = 3\kappa$ in order to obtain a correct scaling for numerical stabilisation.

In the very last example, robustness of the proposed C-TOUCH scheme on a rather complex geometry is shown. The geometry [4] displayed in Fig. 34a is very similar to a cardiovascular stent widely used in biomedical applications. This stent-like structure has an initial outer diameter of $D_O = 10$ mm, a thickness of $T = 0.1$ mm and a total length of $L = 20$ mm. For clarity, the dimensions of one of the repeated patterns on a planar surface are shown in Fig. 34b. In this problem, we show crushing behaviour of the stent-like structure by applying a constant traction of $\boldsymbol{t}_b = [0, 0, -100]^T$ kPa at the top and bottom of the structure along the X-Z plane. Due to the presence of three symmetry planes, one eighth of

(a) Initial configuration
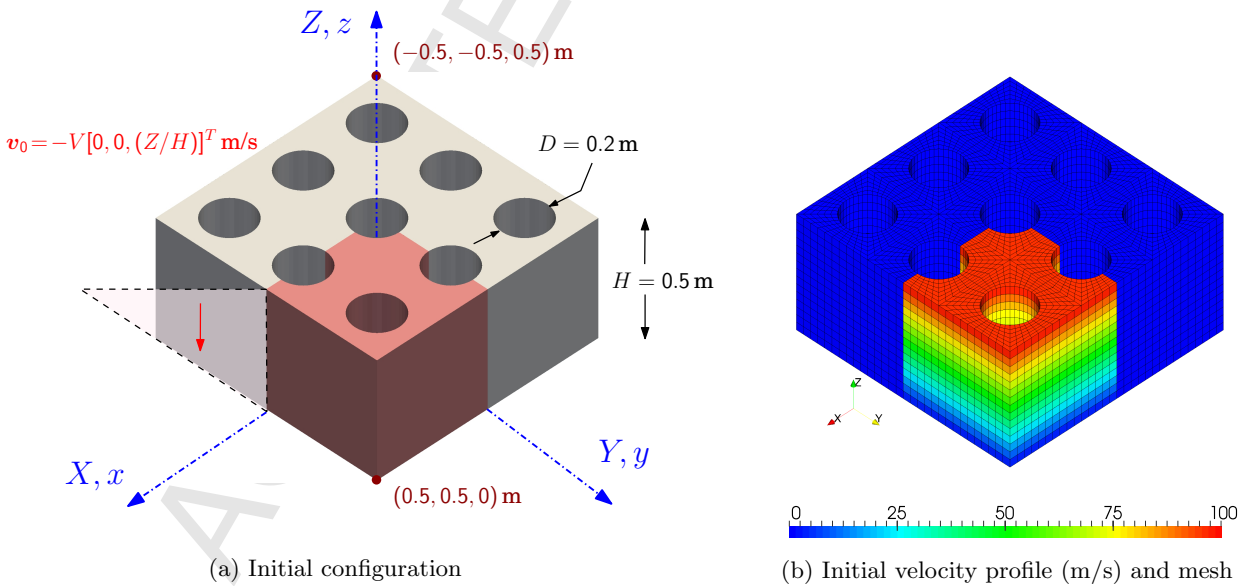
(b) Initial velocity profile (m/s) and mesh

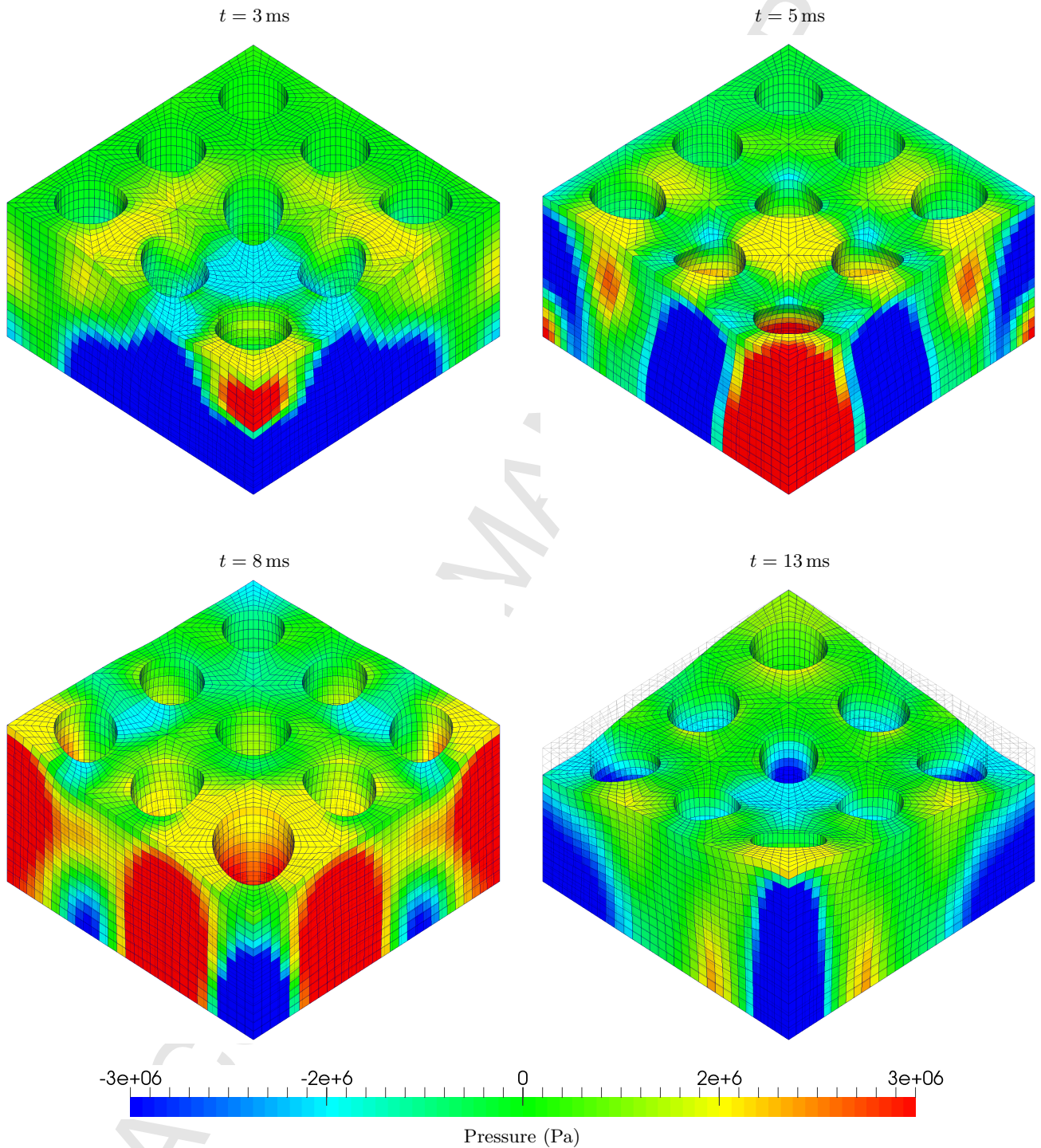Figure 29: Punch test: Problem setup.

---

[4] The CAD is freely available at www.grabcad.com

Figure 30: Punch cube: Sequence of deformed shapes plotted with pressure distribution using the $\{p, F, H, J\}$ C-TOUCH scheme with $\tilde{\kappa} = 3\kappa$. Results obtained with a discretisation of 32400 hexahedral elements using velocity $v_0 = -V [0, 0, (Z/H)]^T$ where $V = 100$ m/s and $H = 0.5$ m. A neo-Hookean constitutive model is used with $\rho = 1100$ kg/m^3, $E = 17$ MPa, $\nu = 0.499$ and $\alpha_{\text{CFL}} = 0.3$.
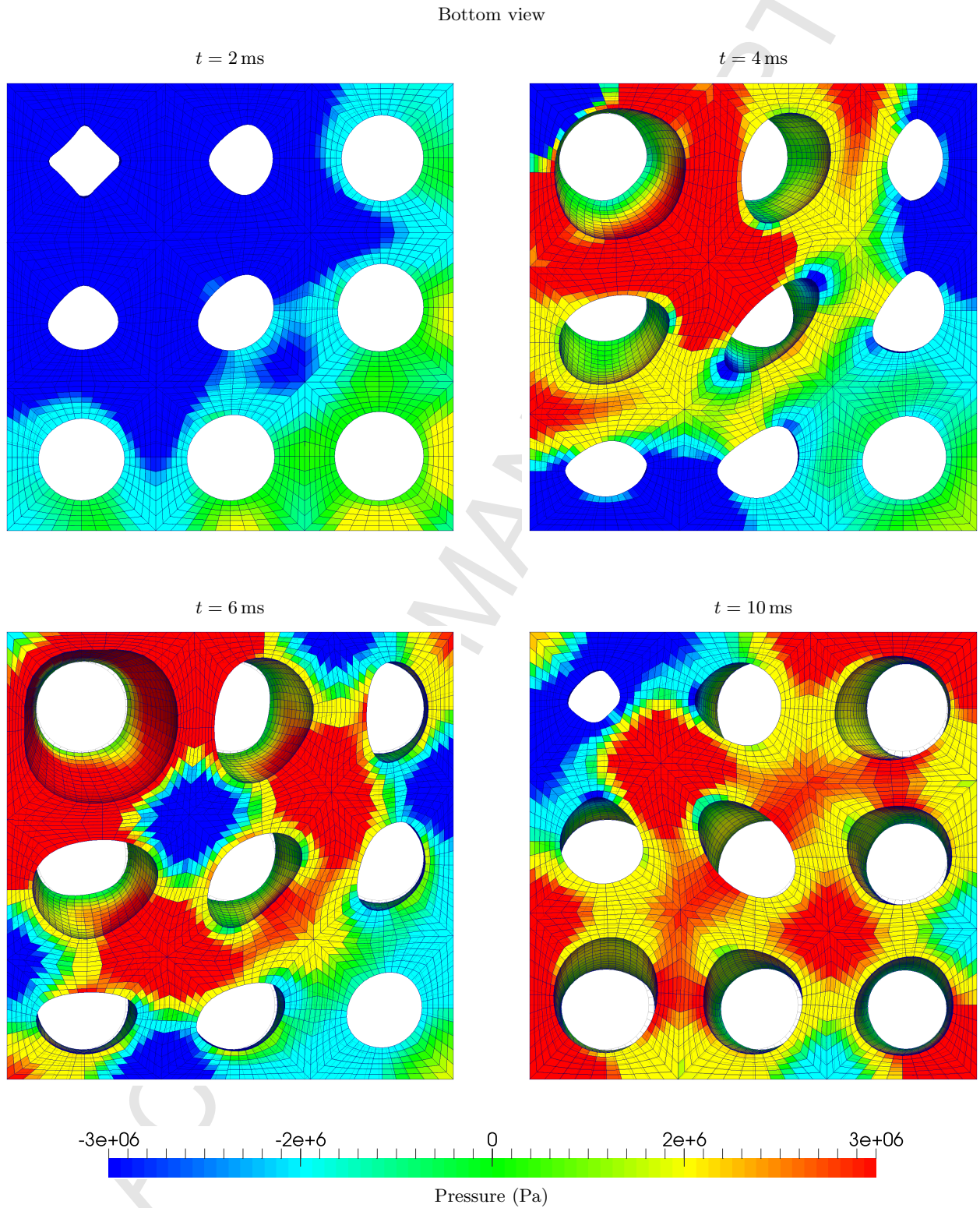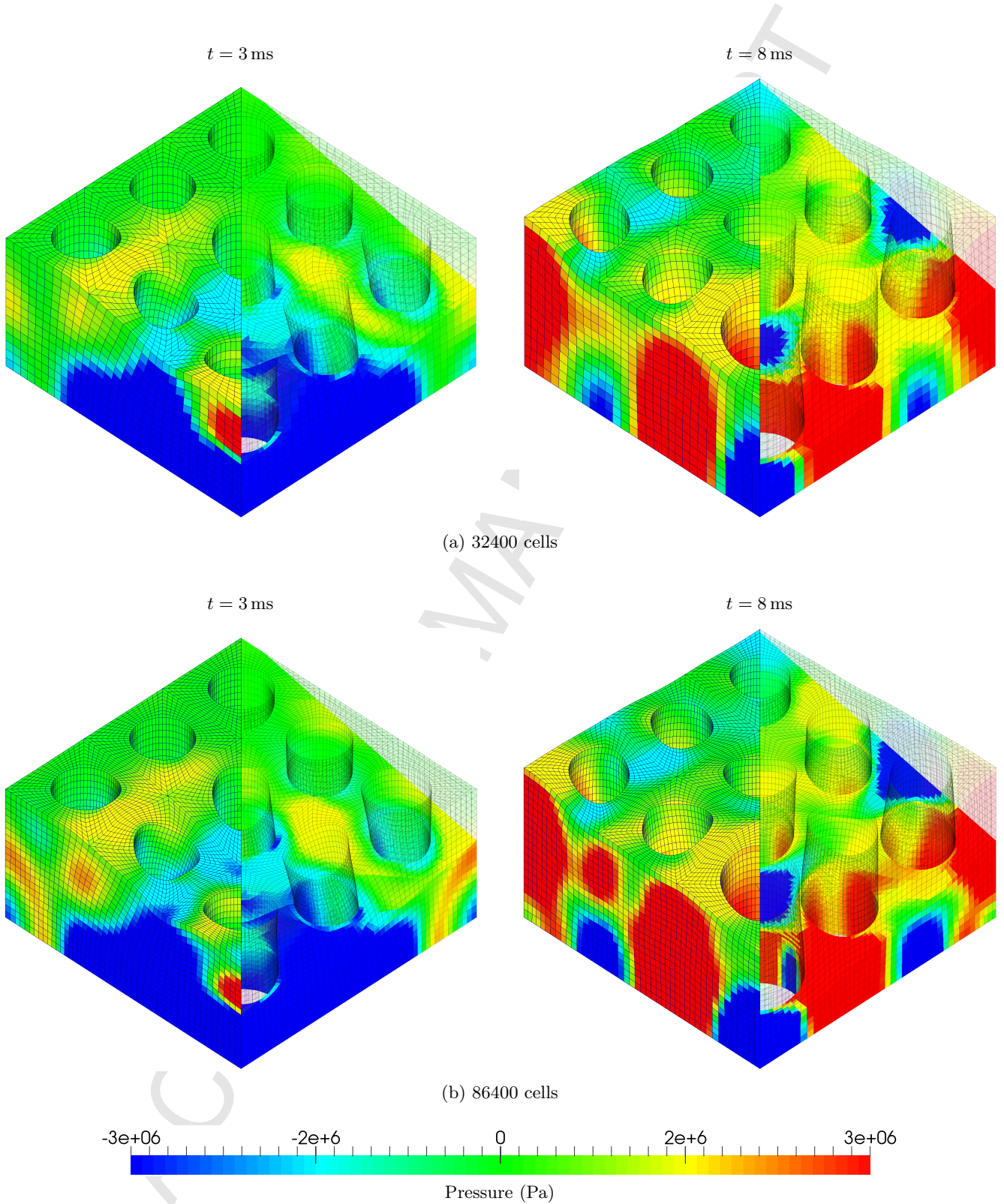
Bottom view

$t = 2\,\text{ms}$

$t = 4\,\text{ms}$

$t = 6\,\text{ms}$

$t = 10\,\text{ms}$

-3e+06   -2e+6   0   2e+6   3e+06

Pressure (Pa)

Figure 31: Punch cube: Sequence of deformed shapes plotted with pressure distribution emphasising bottom view using the $\{\boldsymbol{p}, \boldsymbol{F}, \boldsymbol{H}, J\}$ C-TOUCH scheme with $\tilde{\kappa} = 3\kappa$. Results obtained with a discretisation of 32400 hexahedral elements using velocity $\boldsymbol{v}_0 = -V\,[0, 0, (Z/H)]^T$ where $V = 100\,\text{m/s}$ and $H = 0.5$ m. A neo-Hookean constitutive model is used with $\rho = 1100$ kg/m^3, $E = 17$ MPa, $\nu = 0.499$ and $\alpha_{\text{CFL}} = 0.3$.

39

$t = 3\,\mathrm{ms}$

$t = 8\,\mathrm{ms}$

(a) 32400 cells

$t = 3\,\mathrm{ms}$

$t = 8\,\mathrm{ms}$

(b) 86400 cells

-3e+06	-2e+6	0	2e+6	3e+06

Pressure (Pa)

Figure 32: Punch cube: Mesh refinement of deformed shapes along with pressure distribution at times $t = 3$ ms and $t = 8$ ms using mesh sizes of (a) 32400; and (b) 86400 hexahedral elements. Results obtained using the $\{\boldsymbol{p}, \boldsymbol{F}, \boldsymbol{H}, J\}$ C-TOUCH scheme using $\tilde{\kappa} = 3\kappa$ with velocity $\boldsymbol{v}_0 = -V\,[0, 0, (Z/H)]^T$ where $V = 100$ m/s and $H = 0.5$ m. A neo-Hookean constitutive model is utilised with $\rho = 1100$ kg/m^3, $E = 17$ MPa, $\nu = 0.499$ and $\alpha_{\mathrm{CFL}} = 0.3$.

40

Bottom view
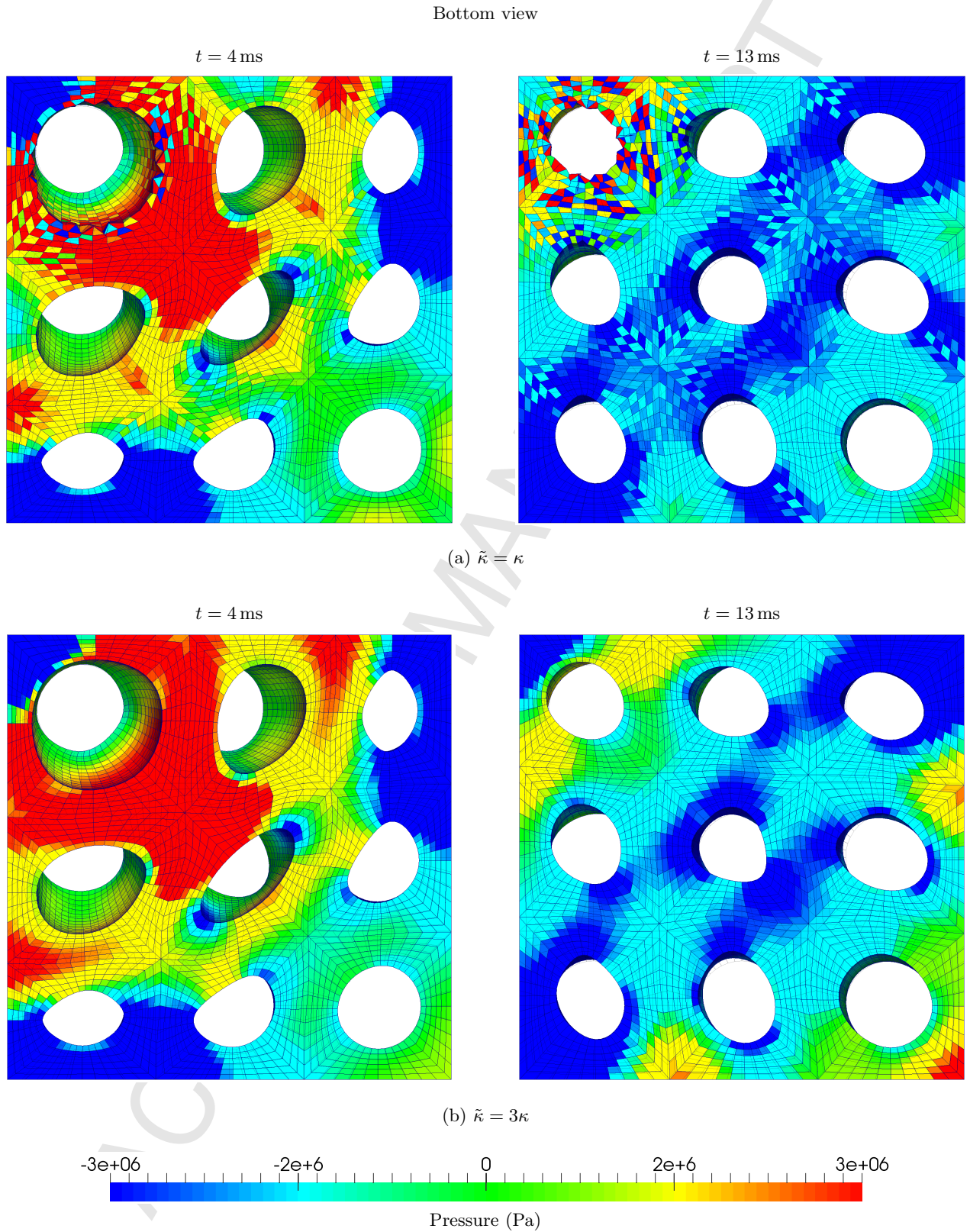
Figure 33: Punch cube: Comparison of deformed shapes plotted with pressure distribution using the $\{p, F, H, J\}$ C-TOUCH scheme with (a) $\tilde{\kappa} = \kappa$; and (b) $\tilde{\kappa} = 3\kappa$. Results obtained with a discretisation of 32400 hexahedral elements using velocity $v_0 = -V[0, 0, (Z/H)]^T$ where $V = 100$ m/s and $H = 0.5$ m. A neo-Hookean constitutive model is used with $\rho = 1100$ kg/m^3, $E = 17$ MPa, $\nu = 0.499$ and $\alpha_{\mathrm{CFL}} = 0.3$.

(a) Initial configuration

(b) Planar $1/32^{\text{th}}$ geometry
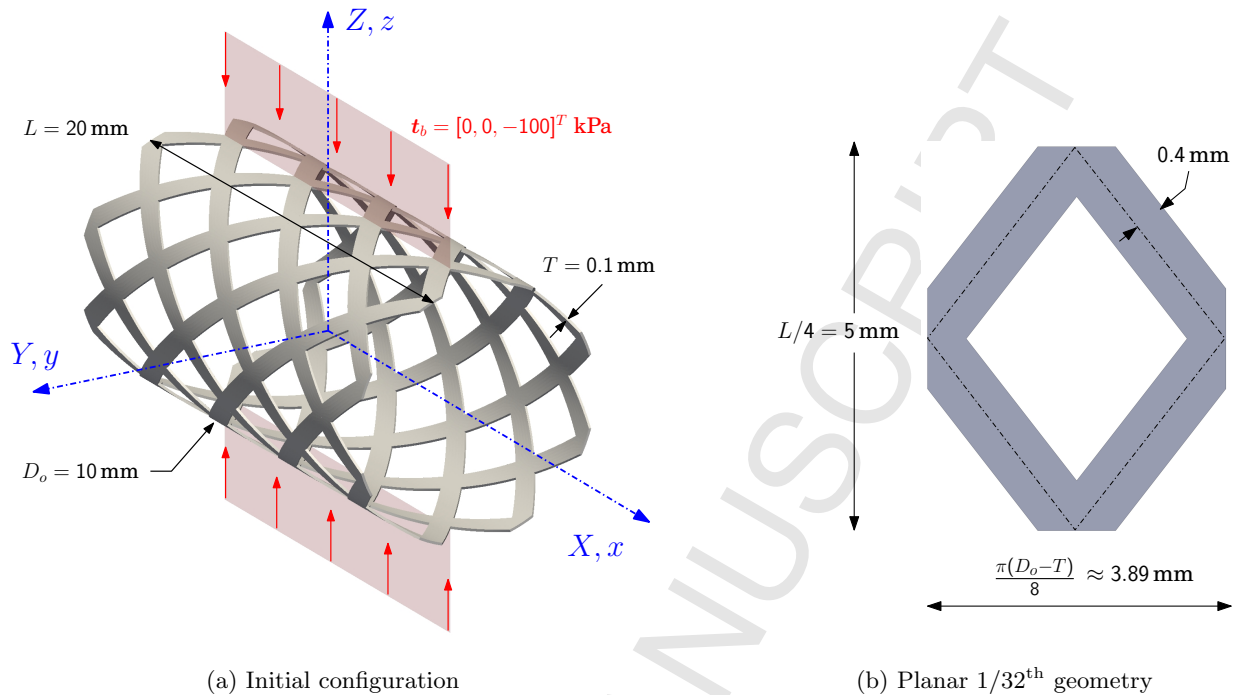
Figure 34: Stent-like structure: Problem setup.

the problem is simulated with appropriate boundary conditions. The structure is modelled with a neo-Hookean material defined with density $\rho_0 = 1100$ kg/m^3, Young's Modulus $E = 17$ MPa and Poisson's ratio $\nu = 0.45$.

Fig. 35 shows the crushing behaviour pattern of the stent-like structure. Following the bending problem analysed earlier in Section 8.3, only two elements (cells) are employed across the thickness to deform the stent. It is remarkable seeing how the deformation behaviour of the structure can be captured on a rather complex geometry. For visualisation purposes, Fig. 36 displays the overall deformation of the stent-like structure at time $t = 500\,\mu$s, with zoomed views in critical areas of sharp spatial gradients. Very smooth pressure field is observed around sharp corners of the structure. A grid independence study has also been carried out in Fig. 37 at time $t = 400\,\mu$s. As the mesh is refined from 6912 elements (2 cells across the thickness) to 43648 elements (4 cells across the thickness), practically identical deformation is obtained. However, as expected, the pressure resolution is enhanced when more elements are employed. To further examine the robustness of the algorithm, we use a larger value of Poisson's ratio $\nu = 0.499$ which leads to the incompressible limit of $\frac{\kappa}{\mu} \approx 500$. As can be observed in the first row of Fig. 38, the pressure field is plotted constant per cell without resorting to any sort of visual nodal interpolation. Alternatively, a nodal averaging process could also be used to display the results, refer to the second row of Fig. 38. The proposed framework, once again, seems very efficient when handling nearly incompressible materials on complicated geometries. This will provide a platform for the modelling of biomedical applications in the near future.

9. Conclusions

In this paper, we present a new computational framework for the numerical analysis of large strain fast solid dynamics, with special attention paid to the case of near incompressibility. A complete set of first order conservation laws [56–59] is presented, where the linear momentum $\boldsymbol{p}$ conservation equation is solved in conjunction with three geometric conservation equations for the minors of the deformation tensor (e.g. one for the deformation gradient $\boldsymbol{F}$, one for the co-factor of the deformation gradient $\boldsymbol{H}$ and one for the Jacobian of the deformation gradient J). For closure of the system, a polyconvex model is employed

42
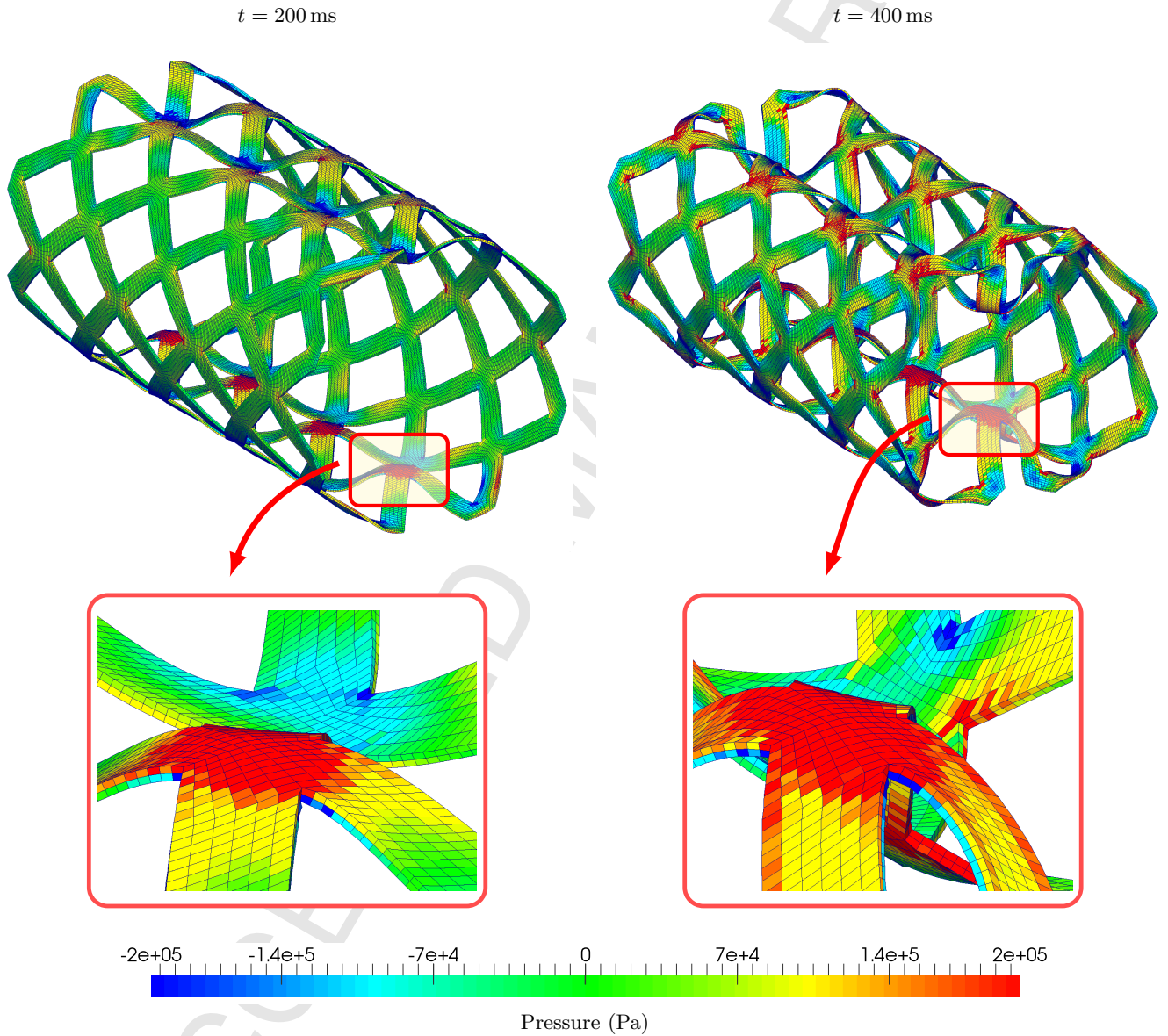
Figure 35: Stent-like structure: Sequence of deformed shapes plotted with pressure distribution using the $\{\boldsymbol{p}, \boldsymbol{F}, \boldsymbol{H}, J\}$ C-TOUCH scheme. Results obtained with a discretisation of 6912 hexahedral elements using traction loading $\boldsymbol{t}_b = [0, 0, -100]^T$ kPa. A neo-Hookean material is used with $\rho = 1100$ kg/m^3, $E = 17$ MPa, $\nu = 0.45$, $\alpha_{\mathrm{CFL}} = 0.3$ and $\Delta t \approx 5 \times 10^{-8}$ s.
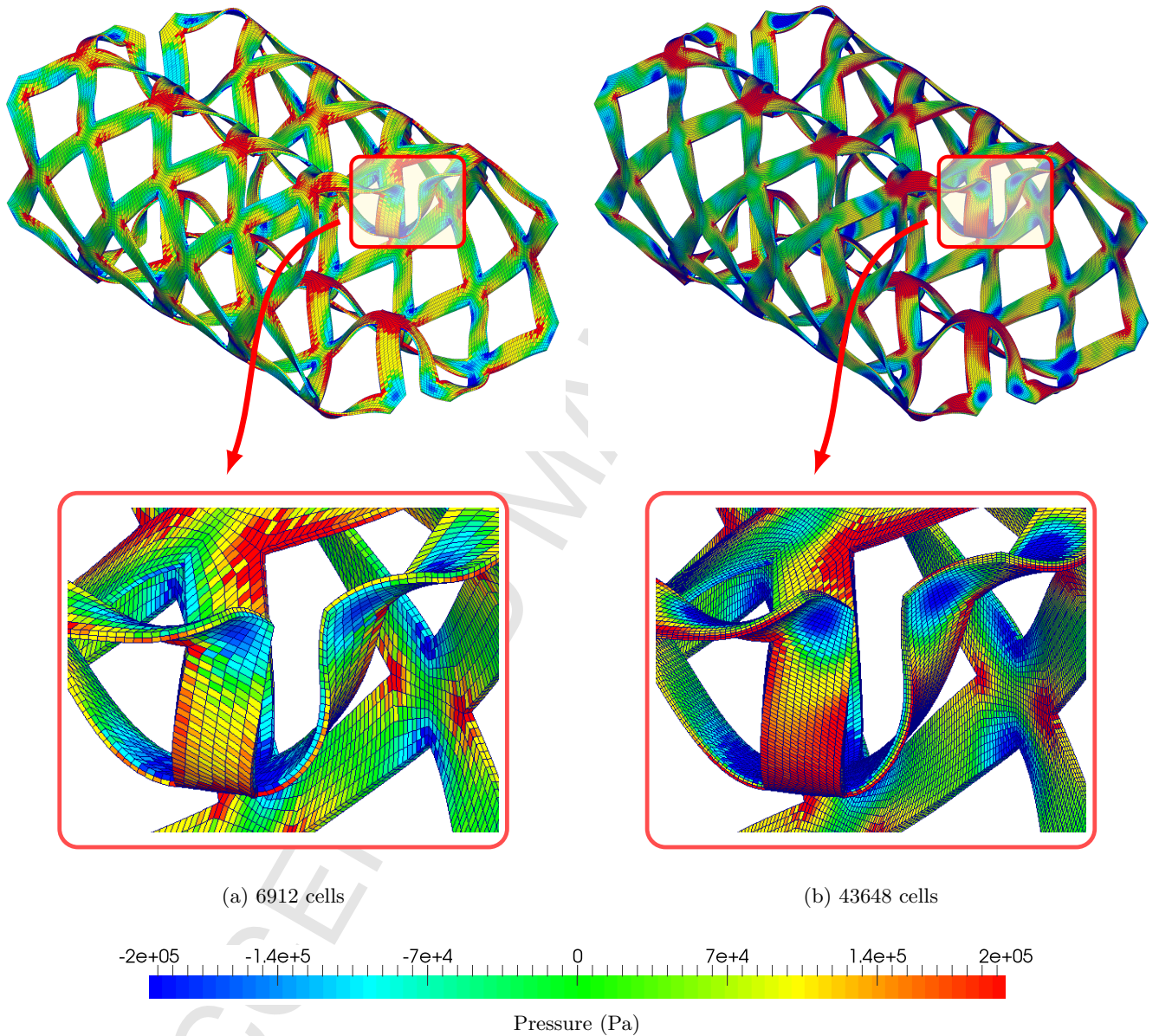
43
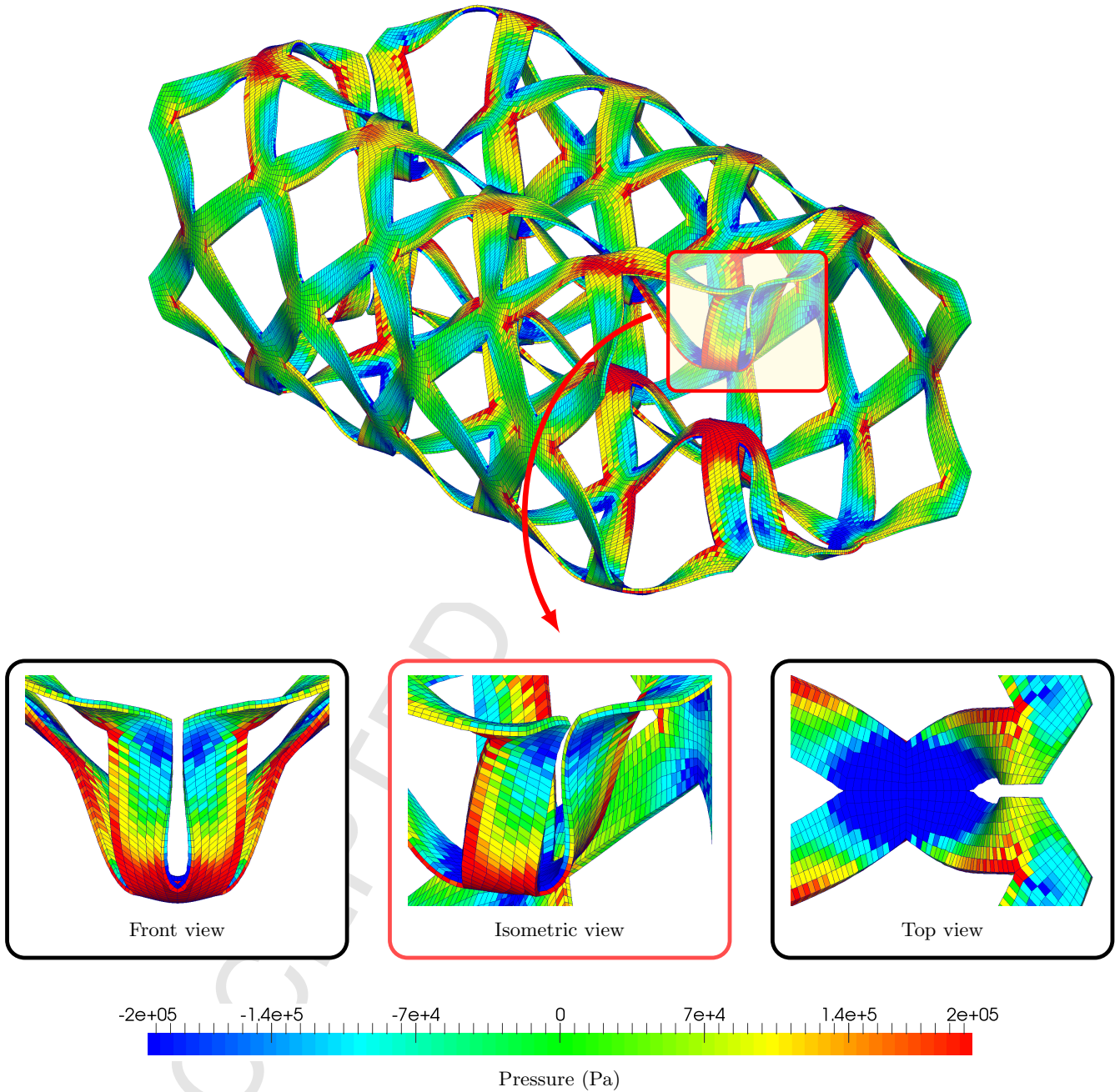
Figure 36: Stent-like structure: Snapshot of deformed shape highlighting the pressure distribution in key region using $\{\boldsymbol{p}, \boldsymbol{F}, \boldsymbol{H}, J\}$ C-TOUCH scheme at time $t = 500\,\mu\text{s}$. Results obtained with a discretisation of 6912 hexahedral elements using traction loading $\boldsymbol{t}_b = [0, 0, -100]^T$ kPa. A neo-Hookean material is used with $\rho = 1100$ kg/m^3, $E = 17$ MPa, $\nu = 0.45$ and $\alpha_{\text{CFL}} = 0.3$.

44

(a) 6912 cells   (b) 43648 cells

Pressure (Pa)

Figure 37: Stent-like structure: Mesh refinement of deformed shapes plotted with pressure distribution at time $t = 400\,\mu$s using the $\{\boldsymbol{p}, \boldsymbol{F}, \boldsymbol{H}, J\}$ C-TOUCH scheme. Results obtained with a discretisation of 6912 and 43648 hexahedral elements using traction loading $\boldsymbol{t}_b = [0, 0, -100]^T$ kPa. A neo-Hookean material is used with $\rho = 1100$ kg/m^3, $E = 17$ MPa, $\nu = 0.45$ and $\alpha_{\mathrm{CFL}} = 0.3$.
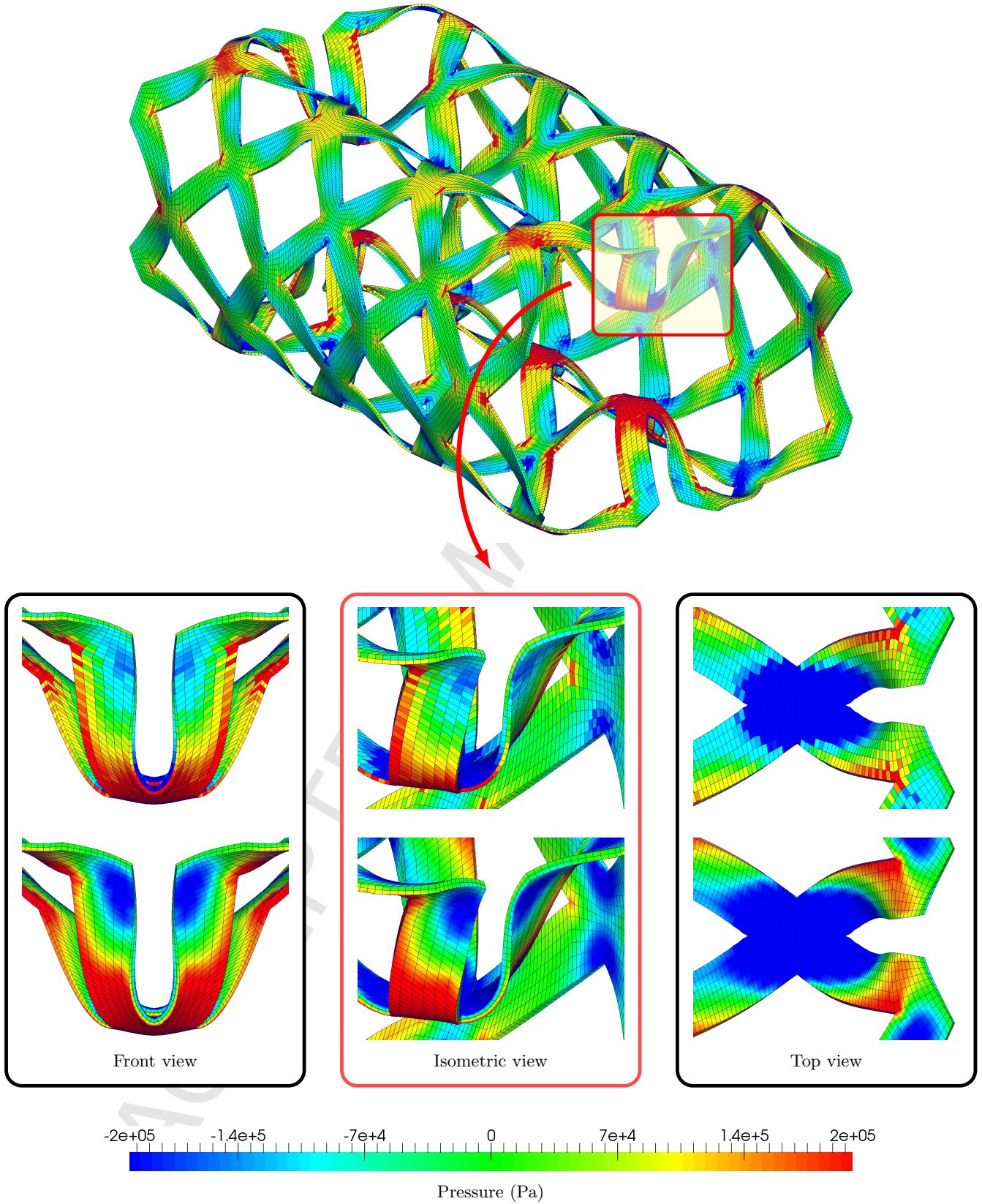
45

Figure 38: Stent-like structure: Snapshot of deformed shape highlighting the pressure distribution in key region using $\{p, F, H, J\}$ C-TOUCH scheme ($\tilde{\kappa} = 3\kappa$) at time $t = 500\,\mu$s. The first row shows the cell center pressure whereas the second row displays the interpolated/extrapolated pressure at the nodes. Results obtained with a discretisation of 6912 hexahedral elements using traction loading $\boldsymbol{t}_b = [0, 0, -100]^T$ kPa. A neo-Hookean material is used with $\rho = 1100$ kg/m^3, $E = 17$ MPa, $\nu = 0.499$ and $\alpha_{\mathrm{CFL}} = 0.3$.

46

guaranteeing the existence of real wave speeds, and thus material stability [2, 57]. The formulation has an eye on bridging the gap between Computational Fluid Dynamics and large strain solid dynamics, with its tailor-made implementation from scratch within the modern Computational Fluid Dynamics code "OpenFOAM".

From the spatial discretisation viewpoint, an acoustic Riemann solver combined with a preconditioning procedure [63–65] is presented. It has been shown that the preconditioned Riemann solver (with a correct scaling of the numerical stabilisation) effectively alleviates the appearance of spurious pressure modes when attempting to model nearly incompressible solids ($\kappa/\mu > 500$). For comparison purposes, an alternative Total Lagrangian version of the nodal scheme presented in [2], in conjunction with a global a posteriori angular momentum projection algorithm, has also been implemented in "OpenFOAM". Finally, an extensive set of challenging numerical examples is presented in order to assess the accuracy, reliability and robustness of the proposed methodologies. The proposed framework shows excellent behaviour in nearly incompressible bending dominated scenarios, yielding second order of convergence for velocities, deviatoric and volumetric components of the stress.

Taking advantage of the new $\{\boldsymbol{p}, \boldsymbol{F}, \boldsymbol{H}, J\}$ computational framework, the authors will now further explore (1) the adaptation of Roe-type Riemann solvers [83] to solids, (2) the ability to model large strain thermoelasticity problems, and (3) an alternative Arbitrary Lagrangian-Eulerian description in large strain solid dynamics [15–17].

10. Acknowledgements

Appendix A. Hyperbolicity

This Appendix is included to present the eigen-structure (consists of eigenvalues and eigenvectors) of a modified flux Jacobian matrix $\boldsymbol{\mathcal{A}_N}$. This is necessary when considering the acoustic Riemann solver in conjunction with a preconditioning procedure, described as follows

$$\boldsymbol{\mathcal{F}}_N^C = \frac{1}{2}\left[\boldsymbol{\mathcal{F}}_N(\boldsymbol{\mathcal{U}}^-) + \boldsymbol{\mathcal{F}}_N(\boldsymbol{\mathcal{U}}^+)\right] - \underbrace{\frac{1}{2}\boldsymbol{\mathcal{P}}^{-1}|\boldsymbol{\mathcal{P}}\boldsymbol{\mathcal{A}_N}|\left(\boldsymbol{\mathcal{U}}^+ - \boldsymbol{\mathcal{U}}^-\right)}_{\text{Preconditioned numerical stabilisation}}. \tag{A.1}$$

To achieve this, and for simplicity, a compressible Mooney Rivlin model described in Reference [57] (refer to equations (20), (22), (24) and (27) in Section 3.3 on pg. 694-695) is considered [57]

$$W(\boldsymbol{F}, \boldsymbol{H}, J) = \alpha(\boldsymbol{F} : \boldsymbol{F}) + \gamma(\boldsymbol{H} : \boldsymbol{H}) + f(J), \tag{A.2}$$

where $f(J) = -4\gamma J - 2\alpha\ln J + \frac{\lambda}{2}(J-1)^2$, $\{\alpha, \gamma, \lambda\}$ are material parameters defined such that $\alpha + \gamma = \frac{\mu}{2}$ [57] and μ represents the shear modulus.

Analogously to the procedure presented in [1] (see Appendix A from pg. 451 to pg. 453), with the aid of (34) and (A.2), the modified eigen-problem by considering each individual component of this system

47

becomes

$$c_\alpha \boldsymbol{p}_\alpha = -2\alpha \boldsymbol{F}_\alpha \boldsymbol{N} - (2\gamma \boldsymbol{F} \times \boldsymbol{H}_\alpha) \boldsymbol{N} - f'' J_\alpha \boldsymbol{H} \boldsymbol{N}; \tag{A.3a}$$

$$c_\alpha \boldsymbol{F}_\alpha = -\frac{\beta^2}{\rho_0} (\boldsymbol{p}_\alpha \otimes \boldsymbol{N}); \tag{A.3b}$$

$$c_\alpha \boldsymbol{H}_\alpha = -\frac{\beta^2}{\rho_0} [\boldsymbol{F} \times (\boldsymbol{p}_\alpha \otimes \boldsymbol{N})]; \tag{A.3c}$$

$$c_\alpha J_\alpha = -\frac{1}{\beta^2 \rho_0} \boldsymbol{p}_\alpha \cdot \boldsymbol{H} \boldsymbol{N}, \tag{A.3d}$$

with $f'' := \frac{d^2 f}{dJ^2} = \lambda + \frac{2\alpha}{J^2}$.

As a consequence of the high level of redundancy in the system of equations being considered, only six wave speeds are different from zero. These can be readily identified by substituting the last three geometric strain equations (A.3b-A.3d) into (A.3a) to give:

$$\left[2\alpha \beta^2 \boldsymbol{p}_\alpha + \frac{f''}{\beta^2} \Lambda_A^2 (\boldsymbol{n} \otimes \boldsymbol{n}) \boldsymbol{p}_\alpha + 2\gamma \beta^2 (\Lambda_T^2 \boldsymbol{I} - \boldsymbol{\Lambda}_T) \boldsymbol{p}_\alpha \right] = \rho_0 c_\alpha^2 \boldsymbol{p}_\alpha, \tag{A.4}$$

where the following notations have been used

$$\begin{aligned} \Lambda_A \boldsymbol{n} &= \boldsymbol{H} \boldsymbol{N}; \\ \Lambda_A^2 &= \boldsymbol{H} \boldsymbol{N} \cdot \boldsymbol{H} \boldsymbol{N}; \\ \boldsymbol{\Lambda}_T &= \boldsymbol{F} \boldsymbol{T}_1 \otimes \boldsymbol{F} \boldsymbol{T}_1 + \boldsymbol{F} \boldsymbol{T}_2 \otimes \boldsymbol{F} \boldsymbol{T}_2; \\ \Lambda_T^2 &= \boldsymbol{F} \boldsymbol{T}_1 \cdot \boldsymbol{F} \boldsymbol{T}_1 + \boldsymbol{F} \boldsymbol{T}_2 \cdot \boldsymbol{F} \boldsymbol{T}_2 = \mathrm{tr} \boldsymbol{\Lambda}_T. \end{aligned} \tag{A.5}$$

Note that $\boldsymbol{T}_{1,2}$ denote an arbitrary pair of orthogonal unit vectors on the reference plane with surface normal $\boldsymbol{N}$ and $\boldsymbol{n}$ is a unit vector orthogonal to the vectors $\boldsymbol{F} \boldsymbol{T}_{1,2}$ which lie on the propagation surface. The first set of eigenvalues corresponding to p-waves is obtained by taking $\boldsymbol{p}_\alpha = \boldsymbol{n}$ to give,

$$c_{1,2} = c_p; \qquad c_p = \pm \sqrt{\frac{\left(2\alpha \beta^2 + 2\gamma \beta^2 \Lambda_T^2 + \frac{f''}{\beta^2} \Lambda_A^2 \right)}{\rho_0}}. \tag{A.6}$$

The remaining four eigenvalues correspond to shear waves where the vibration takes place on the propagation plane. The corresponding velocity vectors are orthogonal to $\boldsymbol{n}$ and in the directions of the unit eigenvectors $\{\boldsymbol{t}_1, \boldsymbol{t}_2\}$ of the rank two tensor $\boldsymbol{\Lambda}_T$. The wave speeds are given by $c_{3,4} = c_{s_1}$ and $c_{5,6} = c_{s_2}$, where

$$c_{s_1} = \pm \beta \sqrt{\frac{\left(2\alpha + 2\gamma \left(\Lambda_T^2 - \lambda_1^2 \right) \right)}{\rho_0}}; \quad c_{s_2} = \pm \beta \sqrt{\frac{\left(2\alpha + 2\gamma \left(\Lambda_T^2 - \lambda_2^2 \right) \right)}{\rho_0}} \tag{A.7}$$

and $\lambda_{1,2}^2$ are the eigenvalues of $\boldsymbol{\Lambda}_T$.

In the case of neo-Hookean model (i.e. by imposing the values of $\alpha = \frac{\mu}{2}$ and $\gamma = 0$), both the pressure and shear wave speeds evaluated at the initial undeformed configuration ($\boldsymbol{F} = \boldsymbol{H} = \boldsymbol{I}$ and $J = 1$) become

$$c_{1,2} = \frac{1}{\beta} \sqrt{\frac{\lambda + \mu(\beta^4 + 1)}{\rho_0}}; \qquad c_{3,4} = c_{5,6} = \beta \sqrt{\frac{\mu}{\rho_0}}, \tag{A.8}$$

where the dimensionless parameter β is defined as $\beta := \frac{\tilde{\kappa}}{\kappa}$ and $\tilde{\kappa}$ is a user-defined material constant, usually taken in the neighbourhood of the bulk modulus κ of the material. The wave speeds $c_{1,2}$ presented in (A.8a) reduces to

$$c_{1,2} \approx \frac{1}{\beta} \sqrt{\frac{\kappa}{\rho_0}}, \tag{A.9}$$

48

when approaching the limit of incompressibility ($\kappa \gg \mu$).

Utilising equation (A.3), the corresponding right eigenvectors are obtained after some simple algebra

$$\boldsymbol{\mathcal{R}}_{1,2} = \begin{bmatrix} \boldsymbol{n} \\ -\frac{\beta^2}{\rho_0 c_{1,2}} \boldsymbol{n} \otimes \boldsymbol{N} \\ -\frac{\beta^2}{\rho_0 c_{1,2}} \boldsymbol{F} \times (\boldsymbol{n} \otimes \boldsymbol{N}) \\ -\frac{\Lambda_A}{\beta^2 \rho_0 c_{1,2}} \end{bmatrix}; \qquad \boldsymbol{\mathcal{R}}_{3,4} = \begin{bmatrix} \boldsymbol{t}_1 \\ -\frac{\beta^2}{\rho_0 c_{3,4}} \boldsymbol{t}_1 \otimes \boldsymbol{N} \\ -\frac{\beta^2}{\rho_0 c_{3,4}} \boldsymbol{F} \times (\boldsymbol{t}_1 \otimes \boldsymbol{N}) \\ 0 \end{bmatrix}; \tag{A.10}$$

$$\boldsymbol{\mathcal{R}}_{5,6} = \begin{bmatrix} \boldsymbol{t}_2 \\ -\frac{\beta^2}{\rho_0 c_{5,6}} \boldsymbol{t}_2 \otimes \boldsymbol{N} \\ -\frac{\beta^2}{\rho_0 c_{5,6}} \boldsymbol{F} \times (\boldsymbol{t}_2 \otimes \boldsymbol{N}) \\ 0 \end{bmatrix}.$$

Finally, evaluation of the set of left eigenvectors now follows in an analogous manner [1]

$$\boldsymbol{\mathcal{L}}_{1,2} = \begin{bmatrix} \boldsymbol{n} \\ -\frac{2\alpha}{c_{1,2}} [\boldsymbol{n} \otimes \boldsymbol{N}] \\ -\frac{2\gamma}{c_{1,2}} [\boldsymbol{F} \times (\boldsymbol{n} \otimes \boldsymbol{N})] \\ -\frac{f'' \Lambda_A}{c_{1,2}} \end{bmatrix}; \qquad \boldsymbol{\mathcal{L}}_{3,4} = \begin{bmatrix} \boldsymbol{t}_1 \\ -\frac{2\alpha}{c_{3,4}} [\boldsymbol{t}_1 \otimes \boldsymbol{N}] \\ -\frac{2\gamma}{c_{3,4}} [\boldsymbol{F} \times (\boldsymbol{t}_1 \otimes \boldsymbol{N})] \\ 0 \end{bmatrix}; \tag{A.11}$$

$$\boldsymbol{\mathcal{L}}_{5,6} = \begin{bmatrix} \boldsymbol{t}_2 \\ -\frac{2\alpha}{c_{5,6}} [\boldsymbol{t}_2 \otimes \boldsymbol{N}] \\ -\frac{2\gamma}{c_{5,6}} [\boldsymbol{F} \times (\boldsymbol{t}_2 \otimes \boldsymbol{N})] \\ 0 \end{bmatrix}.$$

Bibliography

[1] J. Haider, C. H. Lee, A. J. Gil, J. Bonet, A first order hyperbolic framework for large strain computational solid dynamics: An upwind cell centred Total Lagrangian scheme, International Journal for Numerical Methods in Engineering 109 (2017) 407–456.

[2] G. Kluth, B. Després, Discretization of hyperelasticity on unstructured mesh with a cell-centered Lagrangian scheme, Journal of Computational Physics 229 (2010) 9092–9118.

[3] T. J. Hughes, The finite element method: Linear static and dynamic finite element analysis, Courier Corporation, 2012.

[4] D. J. Benson, Computational methods in Lagrangian and Eulerian hydrocodes, Computer Methods in Applied Mechanics and Engineering 99 (1992) 235–394.

[5] D. J. Payen, K. J. Bathe, Improved stresses for the 4-node tetrahedral element, Computers and Structures 89 (2011) 1265–1273.

[6] D. J. Payen, K. J. Bathe, A stress improvement procedure, Computers and Structures 112-113 (2012) 311–326.

[7] H. M. Hilber, T. J. R. Hughes, R. L. Taylor, Improved numerical dissipation for time integration algorithms in structural dynamics, Earthquake Engineering and Structural Dynamics 5 (1977) 283–292.

[8] W. L. Wood, M. Bossak, O. C. Zienkiewicz, An alpha modification of Newmark's method, International Journal for Numerical Methods in Engineering 15 (1980) 1562–1566.

[9] J. Chung, G. M. Hulbert, A time integration algorithm for structural dynamics with improved numerical dissipation: The generalized-α method, Journal of Applied Mechanics 60 (1993) 371–375.

[10] D. D. Adams, W. L. Wood, Comparison of Hilber-Hughes-Taylor and Bossak 'α-methods' for the numerical integration of vibration equations, International Journal for Numerical Methods in Engineering 19 (1983) 765–771.

[11] F. M. Andrade Pires, E. A. de Souza Neto, J. L. de la Cuesta Padilla, An assessment of the average nodal volume formulation for the analysis of nearly incompressible solids under finite strains, Communications in Numerical Methods in Engineering 20 (2004) 569–583.

[12] K. J. Bathe, Finite element procedures, Prentice Hall, 1996.

[13] Y. Onishi, K. Amaya, A locking-free selective smoothed finite element method using tetrahedral and triangular elements with adaptive mesh rezoning for large deformation problems, International Journal for Numerical Methods in Engineering 99 (2014) 354–371.

[14] Y. Onishi, K. Amaya, Performance evaluation of the selective smoothed finite element methods using tetrahedral elements with deviatoric/hydrostatic split in large deformation analysis, Theoretical and Applied Mechanics Japan 63 (2015) 55–65.

[15] A. Huerta, F. Casadei, New ALE applications in non-linear fast-transient solid dynamics, Engineering Computations 11 (1994) 317–345.

[16] A. Rodríguez Ferran, F. Casadei, A. Huerta, ALE stress update for transient and quasistatic processes, International Journal for Numerical Methods in Engineering 43 (1998) 241–262.

[17] A. Rodríguez Ferran, A. Pérez Foguet, A. Huerta, Arbitrary Lagrangian Eulerian (ALE) formulation for hyperelastoplasticity, International Journal for Numerical Methods in Engineering 53 (2002) 1831–1851.

[18] T. Belytschko, W. K. Liu, B. Moran, Nonlinear finite elements for continua and structures, John Wiley and Sons, 2000.

[19] J. Bonet, A. J. Gil, R. D. Wood, Nonlinear solid mechanics for finite element analysis: Statics, Cambridge University Press, 2016.

[20] T. Belytschko, J. S. Ong, W. K. Liu, J. M. Kennedy, Hourglass control in linear and nonlinear problems, Computer Methods in Applied Mechanics and Engineering 43 (1984) 251–276.

[21] D. Flanagan, T. Belytschko, A uniform strain hexahedron and quadrilateral with orthogonal hourglass control, International Journal for Numerical Methods in Engineering 17 (1981) 679–706.

[22] J. Bonet, A. Burton, A simple average nodal pressure tetrahedral element for incompressible and nearly incompressible dynamic explicit applications, Communications in Numerical Methods in Engineering 14 (1998) 437–449.

[23] M. W. Gee, C. R. Dohrmann, S. W. Key, W. A. Wall, A uniform nodal strain tetrahedron with isochoric stabilization, International Journal for Numerical Methods in Engineering 78 (2009) 429–443.

[24] M. A. Puso, J. Solberg, A stabilized nodally integrated tetrahedral, International Journal for Numerical Methods in Engineering 67 (2006) 841–867.

[25] C. Dohrmann, M. Heinstein, J. Jung, S. Key, W. Witkowski, Node-based uniform strain elements for three-node triangular and four-node tetrahedral meshes, International Journal for Numerical Methods in Engineering 47 (2000) 1549–1568.

[26] J. Bonet, H. Marriott, O. Hassan, An averaged nodal deformation gradient linear tetrahedral element for large strain explicit dynamic applications, Communications in Numerical Methods in Engineering 17 (2001) 551–561.

[27] E. A. Souza Neto, D. Perić, M. Dutko, D. R. J. Owen, Design of simple low order finite elements for large strain analysis of nearly incompressible solids, International Journal of Solids and Structures 33 (1996) 3277–3296.

[28] Y. Fryer, C. Bailey, M. Cross, C.-H. Lai, A Control Volume procedure for solving the elastic stress-strain equations on an unstructured mesh, Applied Mathematical Modelling 15 (1991) 639–645.

[29] C. Bailey, M. Cross, A Finite Volume procedure to solve elastic solid mechanics problems in three dimensions on an unstructured mesh, International Journal for Numerical Methods in Engineering 38 (1995) 1757–1776.

[30] A. Slone, C. Bailey, M. Cross, Dynamic solid mechanics using Finite Volume Methods, Applied Mathematical Modelling 27 (2003) 69–87.

[31] G. A. Taylor, C. Bailey, M. Cross, A vertex-based Finite Volume Method applied to non-linear material problems in computational solid mechanics, International Journal for Numerical Methods in Engineering 56 (2003) 507–529.

[32] H. Jasak, H. Weller, Application of the finite volume method and unstructured meshes to linear elasticity, International Journal for Numerical Methods in Engineering 48 (2000) 267–287.

[33] I. Bijelonja, I. Demirdžić, S. Muzaferija, A finite volume method for incompressible linear elasticity, Computer Methods in Applied Mechanics and Engineering 195 (2006) 6378–6390.

[34] P. Cardiff, A. Karač, A. Ivanković, Development of a finite volume contact solver based on the penalty method, Computational Materials Science 64 (2012) 283–284.

[35] P. Cardiff, A. Karač, A. Ivanković, A large strain finite volume method for orthotropic bodies with general material orientations, Computer Methods in Applied Mechanics and Engineering 268 (2014) 318–335.

[36] P. Cardiff, Z. Tuković, P. D. Jaeger, M. Clancy, A. Ivanković, A Lagrangian cell-centred finite volume method for metal forming simulation, International Journal for Numerical Methods in Engineering (2016).

[37] J. A. Trangenstein, P. Colella, A higher-order Godunov method for modeling finite deformation in elastic-plastic solids, Communications on Pure and Applied Mathematics 44 (1991) 41–100.

[38] J. A. Trangenstein, A second-order Godunov algorithm for two-dimensional solid mechanics, Computational mechanics 13 (1994) 343–359.

[39] B. Després, C. Mazeran, Lagrangian Gas Dynamics in Two Dimensions and Lagrangian systems, Archive for Rational Mechanics and Analysis 178 (2005) 327–372.

[40] P.-H. Maire, R. Abgrall, J. Breil, J. Ovadia, A Cell-Centered Lagrangian Scheme for Two-Dimensional Compressible Flow Problems, SIAM Journal on Scientific Computing 29 (2007) 1781–1824.

[41] G. Carré, S. Del Pino, B. Després, E. Labourasse, A cell-centered Lagrangian hydrodynamics scheme on general unstructured meshes in arbitrary dimension, Journal of Computational Physics 228 (2009) 5160–5183.

[42] P.-H. Maire, A high order cell-centered Lagrangian scheme for two-dimensional cylindrical geometry, Journal of Computational Physics 228 (2009) 6882–6915.

[43] D. E. Burton, T. C. Carney, N. R. Morgan, S. K. Sambasivan, M. J. Shashkov, A cell-centered Lagrangian Godunov-like method for solid dynamics, Computers and Fluids 83 (2013) 33–47.

[44] P.-H. Maire, R. Abgrall, J. Breil, R. Loubère, B. Rebourcet, A nominally second-order cell-centered Lagrangian scheme for simulating elastic–plastic flows on two-dimensional unstructured grids, Journal of Computational Physics 235 (2013) 626–665.

[45] G. Georges, J. Breil, P.-H. Maire, A 3D finite volume scheme for solving the Updated Lagrangian form of hyperelasticity, International Journal for Numerical Methods in Fluids 84 (2017) 41–54.

[46] X. Zeng, G. Scovazzi, N. Abboud, O. Colomès, S. Rossi, A dynamic variational multiscale method for viscoelasticity using linear tetrahedral elements, International Journal on Numerical Methods in Engineering (2017).

[47] G. Scovazzi, B. Carnes, X. Zeng, S. Rossi, A simple, stable, and accurate tetrahedral finite element for transient, nearly and fully incompressible solid dynamics: A dynamic variational multiscale approach, International Journal for Numerical Methods in Engineering 106 (2015) 799–839.

[48] S. Rossi, N. Abboud, G. Scovazzi, Implicit finite incompressible elastodynamics with linear finite elements: A stabilized method in rate form, Computer Methods in Applied Mechanics and Engineering 311 (2016) 208–249.

[49] G. Scovazzi, T. Song, X. Zeng, A velocity/stress mixed stabilized nodal finite element for elastodynamics: Analysis and computations with strongly and weakly enforced boundary conditions, Computer Methods in Applied Mechanics and Engineering 325 (2017) 532–576.

[50] C. H. Lee, A. J. Gil, J. Bonet, Development of a cell centred upwind finite volume algorithm for a new conservation law formulation in structural dynamics, Computers and Structures 118 (2013) 13–38.

[51] M. Aguirre, A. J. Gil, J. Bonet, A. A. Carreño, A vertex centred finite volume Jameson–Schmidt–Turkel (JST) algorithm for a mixed conservation formulation in solid dynamics, Journal of Computational Physics 259 (2014) 672–699.

[52] M. Aguirre, A. J. Gil, J. Bonet, C. H. Lee, An upwind vertex centred Finite Volume solver for Lagrangian solid dynamics, Journal of Computational Physics 300 (2015) 387–422.

[53] I. A. Karim, C. H. Lee, A. J. Gil, J. Bonet, A two-step Taylor-Galerkin formulation for fast dynamics, Engineering Computations 31 (2014) 366–387.

[54] C. H. Lee, A. J. Gil, J. Bonet, Development of a stabilised Petrov–Galerkin formulation for conservation laws in Lagrangian fast solid dynamics, Computer Methods in Applied Mechanics and Engineering 268 (2014) 40–64.

[55] A. J. Gil, C. H. Lee, J. Bonet, M. Aguirre, A stabilised Petrov–Galerkin formulation for linear tetrahedral elements in compressible, nearly incompressible and truly incompressible fast dynamics, Computer Methods in Applied Mechanics and Engineering 276 (2014) 659–690.

52

[56] A. J. Gil, C. H. Lee, J. Bonet, R. Ortigosa, A first order hyperbolic framework for large strain computational solid dynamics. Part II: Total Lagrangian compressible, nearly incompressible and truly incompressible elasticity, Computer Methods in Applied Mechanics and Engineering 300 (2016) 146–181.

[57] J. Bonet, A. J. Gil, C. H. Lee, M. Aguirre, R. Ortigosa, A first order hyperbolic framework for large strain computational solid dynamics. Part I: Total Lagrangian isothermal elasticity, Computer Methods in Applied Mechanics and Engineering 283 (2015) 689–732.

[58] C. H. Lee, A. J. Gil, G. Greto, S. Kulasegaram, J. Bonet, A new Jameson–Schmidt–Turkel Smooth Particle Hydrodynamics algorithm for large strain explicit fast dynamics, Computer Methods in Applied Mechanics and Engineering 311 (2016) 71–111.

[59] C. H. Lee, A. J. Gil, O. I. Hassan, J. Bonet, S. Kulasegaram, A variationally consistent Streamline Upwind Petrov Galerkin Smooth Particle Hydrodynamics algorithm for large strain solid dynamics, Computer Methods in Applied Mechanics and Engineering (2017).

[60] C. M. Dafermos, Quasilinear hyperbolic systems with involutions, Springer, 1989.

[61] M. Torrilhon, Locally divergence-preserving upwind finite volume schemes for magnetohydrodynamic equations, SIAM Journal on Scientific Computing 26 (2005) 1166–1191.

[62] E. F. Toro, Riemann solvers and numerical methods for fluid dynamics: A practical introduction, Springer-Verlag, Third edition, 2009.

[63] H. Guillard, C. Viozat, On the behaviour of upwind schemes in the low Mach number limit, Computers & fluids 28 (1999) 63–86.

[64] H. Guillard, A. Murrone, On the behavior of upwind schemes in the low Mach number limit: II. Godunov type schemes, Computers & fluids 33 (2004) 655–675.

[65] H. Guillard, On the behavior of upwind schemes in the low Mach number limit. IV: P0 approximation on triangular and tetrahedral cells, Computers & Fluids 38 (2009) 1969–1972.

[66] F. Rieper, A low-Mach number fix for Roe's approximate Riemann solver, Journal of Computational Physics 230 (2011) 5263–5287.

[67] B. Després, E. Labourasse, Angular Momentum preserving cell-centered Lagrangian and Eulerian schemes on arbitrary grids, Journal of Computational Physics 290 (2015) 28–54.

[68] J. Bonet, A. J. Gil, R. Ortigosa, On a tensor cross product based formulation of large strain solid mechanics, International Journal of Solids and Structures 84 (2016) 49–63.

[69] J. E. Marsden, T. J. R. Hughes, Mathematical foundations of elasticity, Dover Publications, 1994.

[70] J. Bonet, A. J. Gil, R. Ortigosa, A computational framework for polyconvex large strain elasticity, Computer Methods in Applied Mechanics and Engineering 283 (2015) 1061–1094.

[71] R. J. LeVeque, Finite volume methods for hyperbolic problems, volume 31, Cambridge University Press, 2002.

[72] F. Vilar, P.-H. Maire, R. Abgrall, A Discontinuous Galerkin discretization for solving the two-dimensional gas dynamics equations written under Total Lagrangian formulation on general unstructured grids, Journal of Computational Physics 276 (2014) 188–234.

[73] J. Blazek, Computational Fluid Dynamics: Principles and applications, Elsevier, 2005.

53

[74] R. J. LeVeque, Numerical methods for conservation laws, volume 132, Springer, 1992.

[75] A. J. Chorin, A numerical method for solving incompressible viscous flow problems, Journal of Computational Physics 2 (1967) 12 – 26.

[76] Z. Zhang, A. Gil, O. Hassan, K. Morgan, The simulation of 3d unsteady incompressible flows with moving boundaries on unstructured meshes, Computers & Fluids 37 (2008) 620 – 631.

[77] B. Engquist, S. Osher, One-sided difference approximations for nonlinear conservation laws, Mathematics of Computation 36 (1981) 321–351.

[78] R. Courant, K. Friedrichs, H. Lewy, On the partial difference equations of mathematical physics, Mathematische Annalem 100 (1928) 32–74.

[79] S. K. Lahiri, J. Bonet, J. Peraire, L. Casals, A Variationally Consistent Fractional Time-Step Integration Method for Incompressible and Nearly Incompressible Lagrangian Dynamics, International Journal for Numerical Methods in Engineering 63 (2005) 1371–1395.

[80] J. Simo, N. Tarnow, The discrete energy-momentum method. Conserving algorithms for nonlinear elastodynamics, Zeitschrift für angewandte Mathematik und Physik ZAMP 43 (1992) 757–792.

[81] J. Donea, A. Huerta, Finite element methods for flow problems, John Wiley & Sons, 2003.

[82] S. K. Lahiri, J. Bonet, J. Peraire, A Variationally Consistent Mesh Adaptation Method for Triangular Elements in Explicit Lagrangian Dynamics, International Journal for Numerical Methods in Engineering 82 (2010) 1073–1113.

[83] P. L. Roe, Approximate Riemann solvers, parameters vectors, and difference schemes, Journal of Computational Physics 43 (1981) 357–372.

54